HAL
open science

Multiphysics modelling of the steelmaking converter

Nikienta Yannick Doh

To cite this version:

Nikienta Yannick Doh. Multiphysics modelling of the steelmaking converter. Food and Nutrition. Université de Lorraine, 2012. English. NNT : 2012LORR0136 . tel-01749372

HAL Id: tel-01749372

https://hal.univ-lorraine.fr/tel-01749372v1

Submitted on 29 Mar 2018

HAL is a multi-disciplinary open access archive for the deposit and dissemination of scientific research documents, whether they are published or not. The documents may come from teaching and research institutions in France or abroad, or from public or private research centers.

L'archive ouverte pluridisciplinaire **HAL**, est destinée au dépôt et à la diffusion de documents scientifiques de niveau recherche, publiés ou non, émanant des établissements d'enseignement et de recherche français ou étrangers, des laboratoires publics ou privés.

UNIVERSITÉ DE LORRAINE

AVERTISSEMENT

Ce document est le fruit d'un long travail approuvé par le jury de soutenance et mis à disposition de l'ensemble de la communauté universitaire élargie.

Il est soumis à la propriété intellectuelle de l'auteur. Ceci implique une obligation de citation et de référencement lors de l'utilisation de ce document.

D'autre part, toute contrefaçon, plagiat, reproduction illicite encourt une poursuite pénale.

Contact : ddoc-theses-contact@univ-lorraine.fr

LIENS

Code de la Propriété Intellectuelle. articles L 122. 4
Code de la Propriété Intellectuelle. articles L 335.2- L 335.10
http://www.cfcopies.com/V2/leg/leg_droi.php
http://www.culture.gouv.fr/culture/infos-pratiques/droits/protection.htm

Modélisation multiphysique du convertisseur d'aciérie

THESE

Présentée et soutenue publiquement le 26 janvier 2012

Pour l'obtention du grade de

Docteur de l'Université de Lorraine

(Science des Matériaux)

Ecole Doctorale: Energie Mécanique et Matériaux

par

Yannick Nikienta DOH

Composition du jury

Mr. E. CLIMENT	Professeur, IMFT, FRANCE	Rapporteur
Mr. M. JOLLY	Senior lecturer, University of Birmigham, UK	Rapporteur
Mr. P. CHAPELLE	Co-directeur de thèse, Chargé de recherches, IJL, FRANCE	Examinateur
Mme S. DENIS	Professeur, IJL, FRANCE	Examinateur
Mr. E. FIANI	Ingénieur, ADEME, Angers, FRANCE	Examinateur
Mr. P. GARDIN	Ingénieur R&D, ArcelorMittal Maizières, FRANCE	Examinateur
Mr. A. JARDY	Directeur de thèse, Chargé de recherches, IJL, FRANCE	Examinateur
Mr. K. PERICLEOUS	Professor, University of Greenwich, UK	Examinateur
Mr. G. DJAMBAZOV	Senior research fellow, University of Greenwich, UK	Invité
Mr. G. GHAZAL	Ingénieur R&D, ArcelorMittal Maizières, FRANCE	Invité

To my mom,

Acknowledgements

This thesis ends after these three years of research conducted in Nancy at Institut Jean Lamour and in London at the University of Greenwich.
Thanks God, the merciful and the passionate, for providing me the opportunity to step in the excellent world of science. To be able to step strong and smooth in this way, I have also been supported and supervised by many people to whom I would like to express my gratitude to them in my humble acknowledgments.

Foremost, I would like to express my sincere gratitude to my advisors at Institut Jean Lamour Dr Alain Jardy and Dr Pierre Chapelle and at the University of Greenwich, Pr Koulis Pericleous and Dr Georgi Djambazov for the continuous support of my PhD study and research, for their patience, motivation, enthusiasm, and immense knowledge. Their guidance helped me in all the time of research and writing of this thesis. I could not have imagined having a better advisors and mentors for my PhD study.

Besides my advisors, I would like to thank Dr Pascal Gardin and Dr Ghassan Ghazal at ArcelorMittal Maizières for their encouragement, insightful comments, and technical support.

My sincere thanks also go to ADEME (French Environment and Energy Management Agency) and Conseil régionale de Lorraine for the financial help they sponsored me, helping me conducting this PhD to its end.

I thank my fellow labmates at IJL: Andrea, Ashish, Benoit, Gaël, Ismael, J.F., Julien, Khalid, Marie, Mathieu, Mathilde, Miha, Natacha, Olivier, Paolo, Rebecca, Sebastian, Valerio, Vincent and Yilin and at the University of Greenwich: Bruno, Carmen, Mahazar, Sharmin, Xiaoyang and Zach for all the mutual aid and the fun we had in the last three years.

Last but not least, I would like to thank my father, my mother, my sister Evelyne and her daughter Nola and my brothers Lionel and Cédrick for their support, encouragement and understanding during these crucial years.

Contents

ACKNOWLEDGEMENTS II

CONTENTS IV

LIST OF FIGURES VIII

LIST OF TABLES XII

NOMENCLATURE XIV

INTRODUCTION 2

DESCRIPTION OF THE PROCESS 2

INDUSTRIAL AND ENVIRONMENTAL ISSUES 4

AIMS AND SCHEDULE OF THE PHD 5

CHAPTER I LITERATURE REVIEW 7

I.1 FREE GAS JETS 7

I.1.1 Subsonic gas jets 7

I.1.1.1 Description 7

I.1.1.2 Velocity profiles and spread of the jet in the ZEF 8

I.1.2 Supersonic gas jets 9

I.1.2.1 Nozzle equations 9

I.1.2.2 Structure of a supersonic gas jet 10

I.2 IMPINGEMENT OF A GAS JET ONTO A LIQUID SURFACE 13

I.2.1 Cold and hot model experiments 14

I.2.2 Analytical models of the cavity depth 17

I.2.3 Modelling studies 19

I.3 GENERATION OF LIQUID DROPLETS 24

I.3.1 Experimental studies 24

I.3.2 Mechanisms of droplet generation 26

I.4 POST-COMBUSTION 27

I.5 CONCLUSIONS 32

CHAPTER II IMPINGEMENT OF A JET ONTO A LIQUID SURFACE: NUMERICAL MODEL 35

II.1 MATHEMATICAL MODEL 35

II.1.1 Fluid flow equations 35

II.1.2 Turbulence modelling 35

II.1.2.1 The standard k-ε model 35

II.1.2.2 The filtered k-ε model 36

II.1.3 Differencing schemes ... *36*
II.1.3.1 The Hybrid scheme [70] ... 37
II.1.3.2 The Smart scheme [71] ... 37
II.1.4 Free surface deformation model ... *37*
II.1.4.1 Donor-Acceptor ... 38
II.1.4.2 Counter Diffusion Method ... 38
II.1.5 Compressibility modelling ... *39*
II.1.5.1 Energy conservation equation ... 39
II.1.5.2 Pressure correction equation ... 39
II.1.5.3 Modification to the turbulence model for compressible flow ... 40
II.1.5.4 Zonal-GALA ... 42
II.1.6 Boundary conditions of the model ... *43*
II.2 SIMULATION OF A FREE JET ... 44
II.2.1 Geometry and boundary conditions ... *45*
II.2.2 Results ... *46*
II.3 SIMULATION OF QIAN ET AL. 2-PHASE EXPERIMENT ... 49
II.3.1 Influence of grid size ... *50*
II.3.2 Comparison of two VOF models ... *51*
II.3.3 Influence of the boundary conditions at the lance outlet ... *52*
II.3.3.1 Non-uniform profiles of u, k and ε at a straight lance outlet ... 53
II.3.3.2 Influence of the distributions of u, k and ε at the lance outlet on the cavity prediction ... 54
II.3.4 Comparison of two different k-ε turbulence models ... *56*
II.3.5 Comparison of two different differencing schemes ... *56*
II.3.6 Optimal input and model validation ... *57*
II.4 SIMULATION OF THE IJL JET-CAVITY EXPERIMENT ... 59
II.4.1 Experiments made at IJL ... *59*
II.4.2 Results ... *60*
II.4.2.1 Example of experimental results ... 60
II.4.2.2 Simulation results ... 60
II.5 SIMULATION OF QIAN ET AL. 3-PHASE EXPERIMENT ... 62
II.5.1 Three-phase handling ... *62*
II.5.2 Experiment and boundary conditions ... *63*
II.5.3 Kerosene as the second liquid ... *64*
II.5.4 Corn oil as the second liquid ... *65*
II.6 SIMULATION OF A SUPERSONIC OXYGEN JET IMPACTING A LIQUID STEEL BATH ... 66
II.7 CONCLUSIONS ... 72

CHAPTER III POST-COMBUSTION NUMERICAL MODEL ... 75

III.1 MATHEMATICAL MODEL ... 75
III.1.1 Main assumptions ... *75*
III.1.2 Governing equations ... *76*

III.1.2.1 Transport equations 76
III.1.2.2 Derived parameters 78
III.1.2.3 Penetration of the oxygen in the bath 78
III.1.3 Boundary conditions 79
III.2 NUMERICAL RESULTS 80
III.2.1 Nippon Steel Corp. Case 80
III.2.1.1 Experiment and boundary conditions 80
III.2.1.2 Results 81
III.2.2 6t pilot case 84
III.2.2.1 Experiment and boundary conditions 84
III.2.2.2 Results 86
III.2.3 Industrial converter 97
III.2.3.1 Boundary conditions 97
III.2.3.2 Results 98
III.3 CONCLUSIONS 100
CONCLUSIONS AND PROSPECTS 103
CONCLUSIONS 103
PROSPECTS 105
REFERENCES 107
APPENDIX A: INDUSTRIAL CONVERTER: JET-CAVITY SIMULATION 117
RÉSUMÉ ÉTENDU EN FRANÇAIS 121

List of figures

Figure 1: From iron ore to semi-finished steel products [1]. 2
Figure 2: Different techniques of O_2 supply [3]. 3
Figure 3: Evolutions of the species content into the bath as a function of the blowing technique [4]. 3
Figure 4: Top blown basic oxygen converter. 3
Figure 5: Examples of BOF size (dimensions in m) [6]. 3
Figure 6: Example of the evolution of the species content with the blowing time [2]. 3
Figure 7: PHYSICA: levels of code abstraction [8]. 6
Figure 8: Subsonic jet structure [14]. 8
Figure 9: Supersonic flow patterns downstream a nozzle [18]. 10
Figure 10: Structure of a supersonic gas jet [5]. 11
Figure 11: Schematic diagram of the jet decaying model [19]. 11
Figure 12: Comparison of the predictions obtained using the equations presented in Table 2. 12
Figure 14: Surface deformation modes [30]. 14
Figure 15: The two modes of drop generation [51]. 25
Figure 16: Wavelength of Kelvin-Helmholtz [58]. 26
Figure 17: Post-combustion model [60]. 28
Figure 18: ArcelorMittal post-combustion model [64]. 30
Figure 19: Interface shape as represented in the Donor-Acceptor scheme. 38
Figure 20: Comparison of the centreline velocity computed in [74] against the experimental data from Sumi et al. [79]. 42
Figure 21: Principle of the Zonal-GALA approach. 43
Figure 22: Computational domain. 43
Figure 23: Geometry of the computational domain (dimensions in mm). 46
Figure 24: Mesh of the computational domain. 46
Figure 25: Centreline velocity: comparison between various simulation results and Hussein et al. experimental data fit [80]. 47
Figure 26: Radial profile of the axial velocity at 70 D_n: comparison between various simulation results and Hussein et al. experimental data fit [80]. 48
Figure 27: Experimental apparatus of Qian et al. [35]. 49
Figure 28: Geometry and initial conditions in Qian experiment (dimensions in mm). 50
Figure 29: Time-averaged interface for different meshes. 51

Figure 30: Time-averaged interfaces predicted using the Donor-Acceptor scheme and the Counter Diffusion Method. 52
Figure 31: Instantaneous surface profile: a) CDM b) DA. 52
Figure 32: Geometry of the straight lance. 53
Figure 33: Axial velocity at the lance inlet and outlet. 53
Figure 34: Turbulent kinetic energy at the lance inlet and outlet. 54
Figure 35: Dissipation rate of the turbulent kinetic energy at the lance inlet and outlet. 54
Figure 36: Centreline velocity in the gaseous phase. 55
Figure 37: Time-averaged interface for different outlet profiles of u, k and ε. 55
Figure 38: Time-averaged interface predicted using the standard and the filtered k-ε model. 56
Figure 39: Time-averaged interface for two differencing schemes. 57
Figure 40: Time-averaged interface of the cavity for the 10 cases. 58
Figure 41: Experiment developed at IJL. 60
Figure 42: Cavity depth as a function of the flowrate for different lance heights. 60
Figure 43: Mesh (66x63 cells) of the IJL model, red line is the initial liquid level. 61
Figure 44: Time-averaged distribution of the velocity magnitude in the gas phase. 61
Figure 45: Time-averaged interface of the cavity in the IJL model. 62
Figure 46: Mesh of the computational domain and initial regions occupied by the three phases. 64
Figure 47: Time-averaged interfaces for air-kerosene-water (U_0=6.38 m/s). 64
Figure 48: Time-averaged interfaces for air-kerosene-water (U_0=7.61 m/s). The “white regions” (non-hatched parts) represent regions where the three different phases are present. 65
Figure 49: Time-averaged interfaces for air-corn oil-water (U_0=4.42 m/s). 65
Figure 50: Time-averaged interfaces for air-corn oil-water (U_0=7.12 m/s). The “white regions” (non-hatched parts) represent regions where the three different phases are present. 66
Figure 51: Schematic representation of the pilot-scale converter (dimensions in mm). 67
Figure 52: Mesh (51x107 cells) of the pilot-scale converter. 67
Figure 53: Streamlines and velocity distributions in the pilot-scale converter (U_0=378 m/s) at five different time instants. 68
Figure 54: Time-averaged density distribution in the pilot-scale converter (U_0=378 m/s). The black curve represents the isoline of the Mach number relative to a value of 0.3. 69
Figure 55: Pilot-scale converter simulation (U_0=378 m/s): interface profile at different time instants. 69

Figure 56: Pilot-scale converter simulation (U_0=378 m/s): interface profile for different C_μ values.....70
Figure 57: Time-averaged density distribution in the pilot-scale converter for different velocities. The black curve represents the isoline of the Mach number relative to a value of 0.3.....71
Figure 58: Pilot-scale converter simulation: interface profile for different velocities.....71
Figure 59: Cavity depth as a function of the inlet velocity. 72
Figure 60: Boundary conditions of the post-combustion model.....79
Figure 61: Schematic representation of the NSC reacting tube apparatus [89].....81
Figure 62: Mesh of the NSC case (20x104 cells).....81
Figure 63: Velocity and temperature distributions in the reacting tube.....82
Figure 64: Distributions of the mole fractions of the species. 82
Figure 65: Species mole fraction at 0.314 m from the O_2 lance tip. 83
Figure 66: Species mole fraction at 0.544 m from the O_2 lance tip. 83
Figure 67: Species centreline mole fraction.....84
Figure 68: Geometry and boundary conditions of the 6t pilot.....85
Figure 69: Mesh (44x137) of the 6t pilot simulation. 87
Figure 70: Streamlines, velocity and temperature distribution in the 6t pilot simulation (Ref. case). 88
Figure 71: Species mass fraction distributions in the 6t pilot simulation (Ref. case): (a) CO, (b) O_2, (c) CO_2. 89
Figure 72: Temperature distribution for different wall temperatures: (a) 500K, (b) 1000K, (c) 2000K.....90
Figure 73: Temperature distribution for different absorption and scattering coefficients: (a)0.1 (b)0.3 (c)0.5.....90
Figure 74: Temperature distribution for different Eddy Break-Up coefficients: (a) 1, (b) 3, (c) 5.....91
Figure 75: CO_2 mass fraction distribution for different Eddy Break-Up coefficient: (a) 1, (b) 3, (c) 5.....91
Figure 76: Deformed mesh (51x107 cells) for the 6t pilot (U_0=385 m/s and h_n=1 m). 93
Figure 77: Streamlines, velocity and temperature distributions in the 6t pilot (U_0=385 m/s; h_n=1 m). 93
Figure 78: Species mass fraction distributions in the 6t pilot (U_0=385 m/s; h_n=1 m). 94
Figure 79: Streamlines and velocity distributions for different inlet velocity in the 6t pilot (h_n=1 m): a)U_0=385 m/s, b)U_0=500 m/s, c)U_0=615 m/s. 95

Figure 80: Temperature distributions for different inlet velocity in the 6t pilot (h_n=1 m): a)U_0=385 m/s, b)U_0=500 m/s, c)U_0=615 m/s. 95
Figure 81: Species mass fraction distributions for different inlet velocity in the 6t pilot (h_n = 1 m): a) U_0=385 m/s, b) U_0=500 m/s, c) U_0=615 m/s. 96
Figure 82: FOS converter. 97
Figure 83: Mesh (95x232 cells) of the industrial converter. 98
Figure 84: Streamlines velocity and temperature distributions in the FOS converter. 99
Figure 85: Species mass fraction inside the FOS converter: a) CO b) O_2 c) CO_2. 100
Figure 86: Mesh (85x192 cells) of a full scale industrial converter. 117
Figure 87: Distribution of the velocity magnitude and streamlines in the gas phase at different time instants. 118
Figure 88: Time-averaged density distribution. 118
Figure 89: Profile of the gas-metal interface. 119
Figure 90: Time-averaged density distribution for three different Mach numbers at the inlet. The black curve represents the isoline of the Mach number relative to a value of 0.3. 119
Figure 91: Profile of the gas-metal interface for different Mach number. 120
Figure 92: Depth of the cavity as a function of the inlet velocity. 120

List of tables

Table 1: Materials balance (kg/t.liq.st) of the steelmaking converter [7]. 4
Table 2: A selection of the equations for the supersonic core length published in the literature (E: experiment; S: simulation).....12
Table 3: Experimental studies in the literature regarding gas jet impinging onto a deformable surface ([1]Inert gas – slag experiments; [2] Negative values referred to experiments with immersed lance).....15
Table 4: Formulas for the cavity depth.....18
Table 5: Computational studies in the literature dealing with the impingement of a gas jet onto a free surface reviewed in this chapter. 20
Table 6: Selection of experimental studies in the literature on liquid droplets resulting from gas jet impingement on a liquid bath. 24
Table 7: Values of constants to calculate C_T. 41
Table 8: Adjusted values of C_μ for different ambient temperatures with T_{jet}=190K and U_0=451 m/s [74]. 41
Table 9: Boundary conditions of the hydrodynamic model. 44
Table 10: Values of the constants in the different turbulence models used in the present study. 45
Table 11: Gas blowing conditions at the nozzle outlet. 46
Table 12: Jet characteristic parameters (Chapter I Eq. 8, Eq. 9 and Eq. 10) for the different turbulence models considered. Comparison with Hussein et al. experimental data [80]. 48
Table 13: Summary of the 10 cases simulated (Δ=0.075 D_n for the filtered k-ε turbulence model and C=2 for the CDM).....58
Table 14: Properties of the liquids and gas blowing conditions at the nozzle outlet (3-phase model). 63
Table 15: Physical properties of the oxygen and liquid steel used in the simulations. 66
Table 16: Adjusted values of C_μ for different inlet velocities with T_{jet}=203 K and T_{amb}=300 K. 70
Table 17: Source and diffusion terms of the system of equations. 76
Table 18: Boundary conditions of the post-combustion model. 80
Table 19: Cases of the 6t simulations with lance height at 2.2 m. 88
Table 20: Summary of the test cases on the 6t pilot (U_0=197 m/s, h_n=2.2 m). 92

Nomenclature

Roman

A	Area	m^2
a	Speed of sound	$m.s^{-1}$
a	Absorption in the radiation model	-
Cp	Specific heat	$J.kg^{-1}.K^{-1}$
D	Diameter	m
f	Mixture fraction	-
F_m	Mass flowrate	$kg.s^{-1}$
F_G	Volumetric gas flow rate at normal condition	$m^3.s^{-1}$
g	Acceleration due to gravity	$m.s^{-2}$
h	Height	m
h	Enthalpy	$J.kg^{-1}$
I	Turbulent intensity	-
J	Curvature	m^{-1}
k	Turbulent kinetic energy	$m^2.s^{-2}$
Lp	Potential core length	m
M	Jet momentum	$kg.m.s^{-2}$
Ma	Mach number	-
m_i	Mass fraction of the species "i" in a cell	-
N_B	Blowing number	-
P	Pressure	Pa
Q	Volumetric flowrate	$m^3.s^{-1}$
r	Radius	m
r	Gas constant (r = 8.314 $J.K^{-1}.mol^{-1}$)	$J.K^{-1}.mol^{-1}$
R	Radiosity	$kg.s^{-3}$
R_B	Generation rate of metal droplets	$kg.s^{-1}$
s	Scattering coefficient	-
st	Stoichiometric reaction of the reaction	-
T	Temperature	K, °C
U	Velocity	$m.s^{-1}$
W	Molecular weight	$kg.mol^{-1}$
We	Weber number	-
x_2	Supersonic core length	m

Greek

α	Liquid volume fraction	-
δ	Half-width of the jet	m
ε	Rate of dissipation of k	$m^2.s^{-3}$
γ	Specific heat ratio	-
γ	Liquid specific weight (ρg)	$kg.m^{-2}.s^{-2}$
λ	Thermal conductivity	$kg.m.s^{-3}.K^{-1}$
μ	Dynamic viscosity	$kg.m^{-1}.s^{-1}$
ν	Kinematic viscosity	$m^2.s^{-1}$
θ	Jet expansion angle	degree
ρ	Density	$kg.m^{-3}$
σ	Surface tension	$kg.s^{-2}$

Subscript

0	Inlet
amb	Ambient
c	Cavity
C	Continuous phase
d	Dispersed phase
eff	Effective
ε	Dissipation rate of k
fu	Fuel
G	Gas
K	Turbulent kinetic energy
ℓ	Liquid
M	Centreline
n	Nozzle
μ	Dynamic viscosity
ox	Oxidant
pr	Product
st	Stoichiometric
t	Throat

Abbreviation

BOF	Basic Oxygen Furnace
CDM	Counter Diffusion Method
CFD	Computational Fluid Dynamic
DA	Donor-Acceptor
RANS	Reynolds Averaged Navier-Stokes
VOF	Volume Of Fluid

Introduction

Description of the process

Steel is an alloy of iron containing up to 2% of carbon (usually up to 1%). For ultra low carbon grade, steel can contain only 40 ppm of carbon. Two mains ways are used to produce molten steel: the first one involves the blast furnace followed by the basic oxygen furnace (BOF) and the second one uses the electric arc furnace (EAF). The first route, which is our main interest in this PhD, can be split into three major steps as displayed in **Figure 1**: the productions of molten pig iron, molten steel and semi-finished steel products.

The production of molten pig iron: It takes place in the blast furnace, where preheated coke, pelleted and sintered iron ore and crushed limestone are supplied from the furnace top and air is blown from the bottom of the furnace. Molten pig iron is produced through the reduction of iron oxides by carbon monoxide. It is collected at 1400°C from the bottom of the furnace.

The production of molten steel: In the BOF, oxygen is blown onto liquid pig iron to decrease its content of carbon. The process lasts around 20 min and produces molten steel which is then purified in the steel refining facility. The operations in the steel refining facility aim to adjust the species composition inside the molten steel.

The production of semi-finished steel products: The refined molten steel is solidified through the continuous casting process into semi-finished steel products (blooms, billets and slabs).

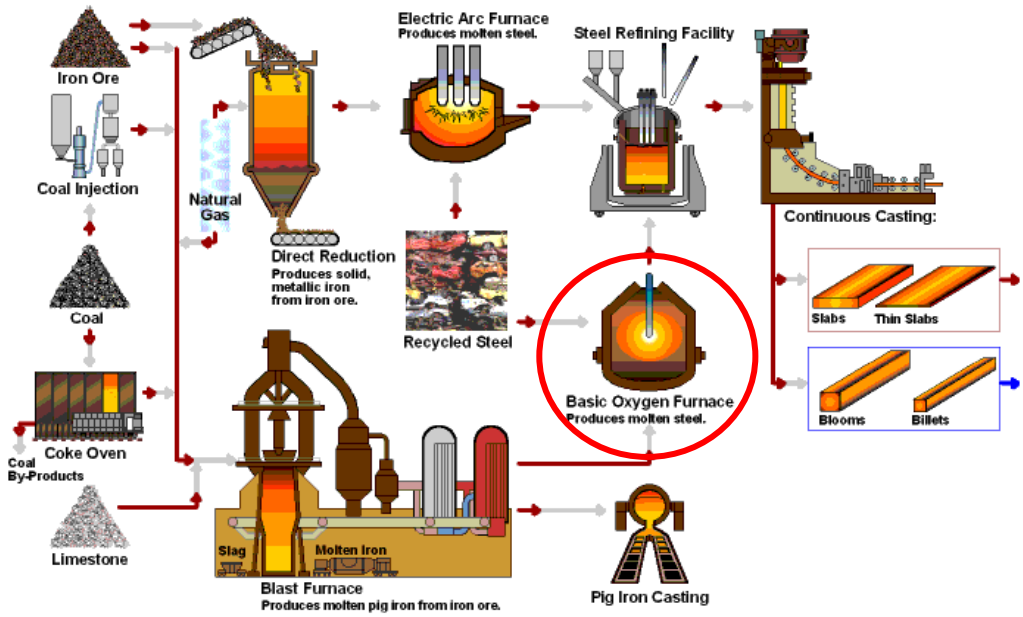

Figure 1: From iron ore to semi-finished steel products [1].

The emphasised area in **Figure 1** is our area of interest during this PhD: the basic oxygen furnace (also called the oxygen converter). As aforementioned, the BOF is the reactor where

pig iron (less than 7% of carbon) is converted into steel (less than 2% of carbon). Note that pig iron contains also typically, apart from iron and carbon, 0.4% silicon, 0.2% manganese, 0.076% phosphorus and 0.006% sulphur [**2**]. Different oxygen blowing techniques (**Figure 2**) can be used to decarburise the pig iron: top blowing, bottom blowing and combined (top and bottom) blowing. The main difference between top and bottom blowing is the evolution of the phosphorus content. As it can be seen in **Figure 3,** during top blowing the decrease of the phosphorus content of the bath is important during the first half of the process, while during bottom blowing the lowering of the phosphorus content is more efficient at the end of the process. Aside from this main difference, the contents of silicon and carbon decrease slightly faster during bottom blowing than during top blowing.

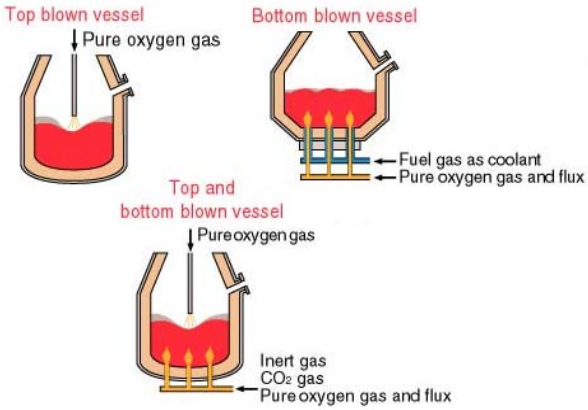

Figure 2: Different techniques of O_2 supply [3].

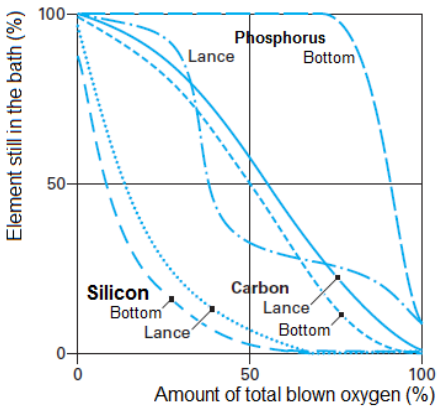

Figure 3: Evolutions of the species content into the bath as a function of the blowing technique [4].

We will focus only on the top blowing converter in this study as sketched in **Figure 4.** In a top blown converter, the oxygen is blown at a supersonic speed (Mach number between 2 and 2.4 [**5**]) through a vertically oriented lance onto the molten pig iron bath, causing the formation of a cavity at the bath surface and the expulsion of liquid droplets above the bath (black points in **Figure 4**), which contribute to increase the metal reaction surface area.

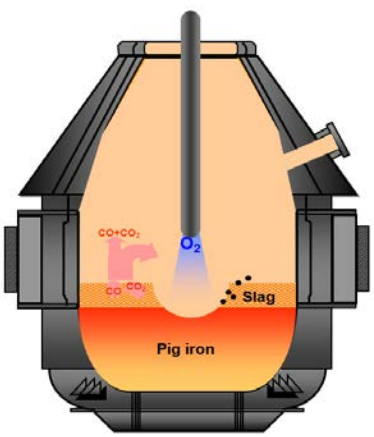

Figure 4: Top blown basic oxygen converter.

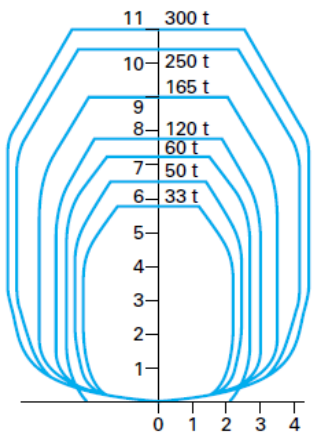

Figure 5: Examples of BOF size (dimensions in m) [6].

The dimensions of the furnace can go over 8 m in diameter and 11 m in height for a charge of iron of 300 tons, as displayed in **Figure 5**.

The oxidation of the carbon dissolved in the bath leads to the production of carbon monoxide (**Eq. 1**). Note that the oxygen may also react with iron and the others elements present in the bath (phosphorous, silicone, manganese, etc.) (**Eq. 3** to **Eq. 7**). These oxides combined with the lime added at the beginning of the process help to create the slag which covers the liquid steel surface. The carbon monoxide exits the bath as bubbles due to buoyancy, and once in the gaseous phase may be oxidised by the remaining oxygen according to **Eq. 2** : the post-combustion. The post-combustion reaction is highly exothermic and is the main contributor to the heating of the bath [**7**]. The typical evolutions of the bath temperature and of the concentration of the various species present in the bath during the blowing process are illustrated in **Figure 6**. One should note the important increase of the bath temperature with the blowing time from 1370°C at the beginning up to 1600°C at the end of the process.

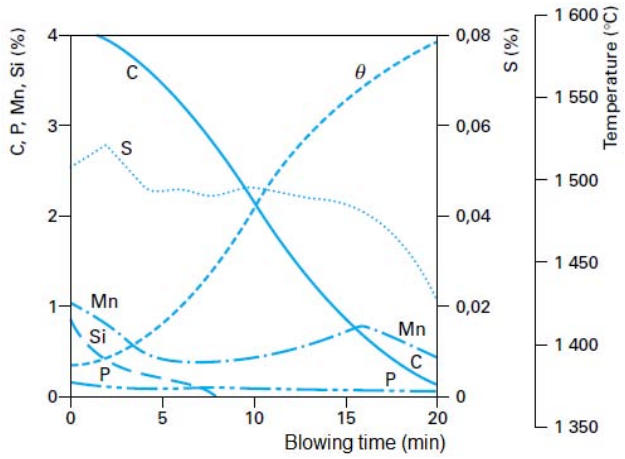

Figure 6: Example of the evolution of the species content with the blowing time [2].

The equations of the decarburisation and the post-combustion are as follows:

$$C + 1/2\ O_{2\,(g)} \rightarrow CO_{\,(g)} \qquad \textbf{Eq. 1}$$

$$CO_{\,(g)} + 1/2\ O_{2\,(g)} \rightarrow CO_{2\,(g)} \qquad \textbf{Eq. 2}$$

The main reactions involved in the slag creation are:

$$Mn + 1/2\ O_{2\,(g)} \rightarrow MnO \qquad \textbf{Eq. 3}$$

$$Si + O_{2\,(g)} + 2\ CaO \rightarrow (CaO)_2SiO_2 \qquad \textbf{Eq. 4}$$

$$2P + 5/2\ O_{2\,(g)} + 3\ CaO \rightarrow (CaO)_3P_2O_5 \qquad \textbf{Eq. 5}$$

$$Fe + 1/2\ O_{2\,(g)} \rightarrow FeO \qquad \textbf{Eq. 6}$$

$$2\ FeO + 1/2\ O_{2\,(g)} \rightarrow Fe_2O_3 \qquad \textbf{Eq. 7}$$

Table 1 presents an example of the inputs and outputs of the converter (in kilogram per ton of liquid steel). To recycle the scrap, it is put as input inside the converter. Different cases differing by the relative amounts of the pig iron and scrap in the input are shown here.

		Maximum iron ore input	Maximum scrap input
Input	Pig iron	929	850
	Scrap	121	212
	Ore	30	3
	Lime (CaO)	24	22
	Dolomite	7	5
	O_2 (m^3/t.liq.st)	44	45
Output	Liquid steel	1000	1000
	Slag	51	46
	Gas (m^3/t.liq.st)	82	75
	Dust	12	12
	Splashing	4	4

Table 1: Materials balance (kg/t.liq.st) of the steelmaking converter [7].

Industrial and environmental issues

The oxidation reactions occurring inside the BOF, in particular the post-combustion, produce a lot of heat (102 MJ/t.liq.st for a 300-ton converter [**7**]). Part of this heat is lost through the reactor walls, the enthalpy of the exhaust gases, etc. For instance, for a 300-ton converter, the heat losses are around 73 MJ/t.liq.st [**7**]. These losses increase when decreasing the converter size (reaching 100 MJ/t.liq.st [**7**] for a 100-ton converter). An optimisation of the energy efficiency of the process would be necessary to decrease the heat losses. Moreover, it could also allow to increase the scrap amount added at the beginning of the process. Indeed, the scrap is cold and some of the heat of the bath is consumed to melt the scrap. The optimisation of the energy efficiency can be done in particular by increasing the post-combustion rate and promoting the transfer of the heat released by this reaction to the metal bath.

The cavity created at the bath surface by the jet impingement is the area where the surface reactions between the metal and oxygen take place. The size and shape of this cavity are strongly related to the blowing conditions at the lance and more specifically to the design of

the lance nozzle (e.g. single or multiple holes). Up to now, relatively little is known on which nozzle design is preferable. In particular, it is believed that improvement of the lance design and a better understanding of the jet-bath interactions would be of strong interest to help shortening the blowing time and increasing the productivity of the process. The impact of the supersonic jet onto the metal bath is also responsible for the generation of a significant amount of liquid metal and slag droplets. Part of these droplets falls back to the bath but some leave the converter as dust, which may cause some environmental issues.

Aims and schedule of the PhD

The aim of this study is to model some aspects of the steelmaking converter in order to help to solve the issues stated above. This study consists of the development of two models which are at present independent: the first one deals with the jet penetration in the bath and the second one with the post-combustion in the gaseous phase.

The jet penetration model aims to better understand the key parameters driving the cavity creation at the bath surface. It will integrate in particular the following features:

- Oxygen jet: the model will consider compressibility effects when simulating the oxygen jet since the jet is supersonic (Mach number around 2) in the industrial case.
- Free surface of the bath: the cavity created by the impingement of the supersonic jet onto the liquid free surface will be determined.

The post-combustion model targets the description of the gaseous phase in the vessel. It will incorporate in particular the following aspects:

- Chemical reactions: the reactions considered here will be the decarburisation reaction (**Eq. 1**) as boundary condition and the post-combustion reaction (**Eq. 2**) to be solved by our model. Other chemical reactions such as the slag-bath reactions will not be considered as a first approach in this study.
- Heat transfer: the convection due to the flow driven by the supersonic jet and the radiative transfer are the main heat transfer mechanisms to be accounted for in the model.

This study was done at Institut Jean Lamour (IJL) in Nancy (FRANCE) in collaboration with the University of Greenwich in London (UK) where I studied for one year. The jet penetration model was mainly developed at IJL whereas the post-combustion one was built at the University of Greenwich.

The study will be done using PHYSICA, a multi-physics (including Computational Fluid Dynamics (CFD)) software developed at the University of Greenwich [**8**]. PHYSICA uses a finite volume approach on structured and unstructured 3D meshes. It is possible to address different physics in the code, e.g. fluid and solid mechanics, heat transfer, electromagnetism, chemical reactions. The main advantage of this code compared to CFD commercial softwares is that it is "open" and enables the user to access the source code of all modules in order to implement specific models (**Figure 7**).

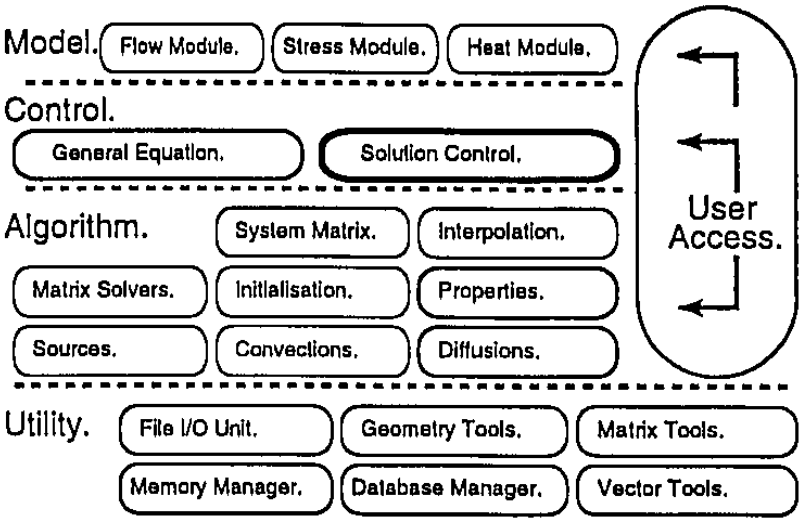

Figure 7: PHYSICA: levels of code abstraction [8].

This thesis includes five chapters. The first one describes the process, the issues involved and the aim of this PhD. The second chapter is a literature review of the physics inside the converter. The behaviour of subsonic and supersonic jets is described and the models and experiments developed to study the impingement of a gas jet onto a liquid surface are reviewed. Then, a selection of the studies dealing with the phenomena associated to the post-combustion inside the gaseous phase and the droplets generation at the edge of the surface cavity is presented. The third and the forth chapters are about the two models developed during this study. The first model is about the impingement of a supersonic jet onto a liquid surface. After a description of the mathematical equations involved, the model is used to simulate two- (air-water and oxygen-steel) and three-phase (air-kerosene/corn oil-water) model experiments. The second model tackles the post-combustion inside the gaseous part together with hydrodynamic and heat transfer (radiative transfer and convection) aspects. This model is applied to study three different scale systems (a laboratory experiment, pilot and industrial converters). In the last chapter, after some concluding remarks, we will finish by the future works which could be done to improve the two developed models.

Chapter I Literature review

The literature review presented in this chapter is divided into four sections. The first three sections focus on various hydrodynamic phenomena associated with the impingement of a gas jet onto a liquid surface, namely the development of the gas jet, the formation of a cavity at the liquid surface and the generation of droplets from this cavity due to the interactions with the jet. The last section deals with phenomena associated to the post-combustion reaction of the carbon monoxide in the top space of a converter, above the metal bath.

I.1 Free gas jets

A supersonic gas jet is a jet with a Mach number greater than one. It can be obtained only with a Laval (convergent-divergent) nozzle. In the BOF, the gas jet that impinges the molten steel surface has generally a Mach number greater than 2. Before describing the behaviour of a supersonic gas jet, we will consider in the first part of this section the behaviour of a subsonic gas jet, since much of the literature studies on jets impinging a liquid surface were performed using such kind of jet.

I.1.1 Subsonic gas jets

I.1.1.1 Description

In a subsonic turbulent[1] free jet, three main regions are generally identified [**10**], as seen in **Figure 8:**

- Potential core region: This region extends from the nozzle exit up to a distance of 3 to 7 times the nozzle outlet diameter [**11**]. No surrounding fluid is entrained so that 95%-99% of the initial velocity is conserved
- Transition region: The centreline velocity begins to decay. The shear stress at the jet boundary creates turbulence (through the generation of Kelvin-Helmholtz vortices) which results in ambient gas entrainment.
- Zone of Established Flow (ZEF): This region appears at a downstream distance of the nozzle typically 15 to 20 times the nozzle outlet diameter [**12,13**]. The axial velocity in this region follows a self-similar Gaussian radial distribution and the centreline velocity decreases hyperbolically with the distance from the nozzle. The characteristic

[1] The Reynolds number ($Re= U_0D_n/\nu$, where U_0, D_n and ν are the gas outlet velocity, the nozzle diameter and the gas kinematic viscosity respectively) is considered to be greater than 2300 [**9**].

relationships of the jet velocity in the ZEF will be presented in detail later in the next paragraph.

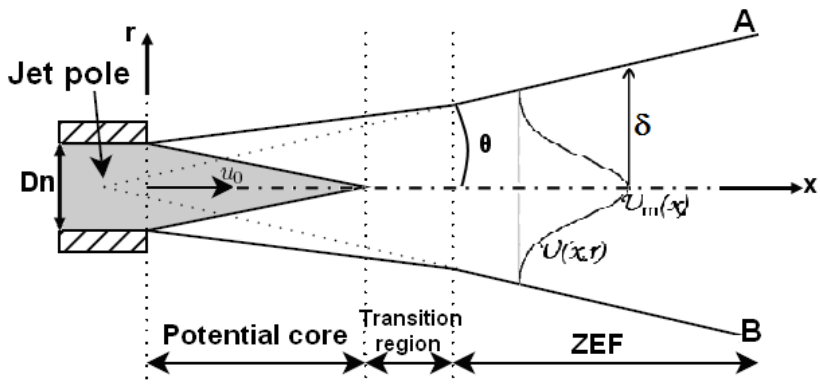

Figure 8: Subsonic jet structure [14].

I.1.1.2 Velocity profiles and spread of the jet in the ZEF

Using the fact that the total momentum remains constant in any cross-section of the jet, Abramovich [**10**] found the centreline velocity of the jet U_m to be inversely proportional to the distance from the nozzle in the ZEF region. Rajaratnam [**9**] reached a similar result (viz. $U_m \sim 1/x$) from a similarity analysis of the equations of motion and the kinetic energy transport equation. **Figure 8** shows the main parameters used to describe the ZEF region of a jet. [OA) and [OB) represent the lines where the axial velocity is negligible (less than 1-5%) compared to the centreline velocity. A virtual origin of the jet is defined and denoted "O". Note that the spreading angle of the jet θ is known to be between 11° and 12° [**14,15**].

In the ZEF region, the axial variations of the centreline velocity $U_m(x)$ and the jet half-width δ and the radial variation of the axial velocity U(x,r) are commonly described in the literature by **Eq. 8** to **Eq. 10**. These equations involve as parameters the velocity at the nozzle exit U_0, two length scales (the nozzle diameter D_n and the x-coordinate of the virtual origin x_0) and two dimensionless coefficients (*a* and *b*, where *a* represents the spreading rate of the jet).

$$\frac{U_m(x)}{U_0} = b\frac{D_n}{x - x_0} \qquad \textbf{Eq. 8}$$

$$\frac{U(x,r)}{U_m(x)} = \exp\left(-\frac{\ln 2}{a^2}\left(\frac{r}{x - x_0}\right)^2\right) \qquad \textbf{Eq. 9}$$

$$\frac{\delta}{D_n} = a\frac{x - x_0}{D_n} \qquad \textbf{Eq. 10}$$

In the above equations, we can notice the importance of the coefficients *a* and *b* whose knowledge enables to fully describe the variation of the axial velocity and the jet half-width in the ZEF. Bailly and Comte-Bellot [**12**] found these coefficients to be linked through a

"compatibility" relationship as described in **Eq. 11** and to be included within the ranges: 5.13<b<7.9 and 0.07<a<0.11.

$$a^2 b^2 = \frac{3}{4}\left(\sqrt{2}-1\right) \approx 0.311 \qquad \textbf{Eq. 11}$$

This relationship has been established by using the momentum conservation on the centreline.

I.1.2 Supersonic gas jets

I.1.2.1 Nozzle equations

The main equations describing the axial variation of the jet parameters in a Laval nozzle are summarized below [**16**]. Considering that the flow is one-dimensional and isentropic, the conservation equations can be used to derive the following relations for the density (ρ), the pressure (p) and the temperature (T) in any section of the nozzle as a function of the properties of the gas in the supply reservoir (ρ_0, p_0 and T_0):

$$\frac{\rho_0}{\rho} = \left(1 + \frac{\gamma - 1}{2} Ma^2\right)^{\frac{1}{\gamma-1}} \qquad \textbf{Eq. 12}$$

$$\frac{p_0}{p} = \left(1 + \frac{\gamma - 1}{2} Ma^2\right)^{\frac{\gamma}{\gamma-1}} \qquad \textbf{Eq. 13}$$

$$\frac{T_0}{T} = 1 + \frac{\gamma - 1}{2} Ma^2 \qquad \textbf{Eq. 14}$$

where γ is the ratio of the gas specific heats at constant pressure and at constant volume (1.4 for diatomic gases).

In the case where the nozzle is chocked (Ma = 1 at the nozzle throat), the gas properties at the nozzle throat (ρ^*, p^* and T^*) are given by (for $\gamma = 1.4$): $\frac{\rho^*}{\rho_0} = 0.634$; $\frac{P^*}{P_0} = 0.528$; $\frac{T^*}{T_0} = 0.833$

Finally, two other useful relations concern respectively the cross-sectional area at any point along the nozzle and the Mach number at the nozzle outlet. Under the assumption that the nozzle is chocked, these relations read:

$$\frac{A}{A^*} = \frac{1}{Ma}\left[\frac{2}{\gamma+1}\left(1 + \frac{\gamma-1}{2} Ma^2\right)\right]^{(\gamma+1)/} \qquad \textbf{Eq. 15}$$

$$Ma_{outlet} = \left[\frac{2}{\gamma-1}\left\{\left(\frac{P_0}{P_{outlet}}\right)^{\frac{\gamma-1}{\gamma}} - 1\right\}\right]^{1/2} \qquad \textbf{Eq. 16}$$

I.1.2.2 Structure of a supersonic gas jet

Depending on the value of the ratio of the gas pressure at the nozzle outlet to the pressure of the ambient gas, three different types (**Figure 9**) of supersonic flow can occur immediately downstream a nozzle [**17**]**:**

- Over-expanded jet ($P_{outlet} < P_{amb}$): The adaptation of the jet to the ambient pressure occurs through a complex pattern of periodic expansion and compressive waves starting by oblique shocks formed at the nozzle edge. Periodic cells ("diamond" structure) are created. The cell length increases when decreasing the ambient pressure.
- Fully expanded jet ($P_{outlet} = P_{amb}$): The nozzle is adapted in this case and there are no waves.
- Under-expanded jet ($P_{outlet} > P_{amb}$): The jet exhibits a similar behaviour as in the over-expanded case. However, in the present case, the under-expansion of the jet causes first expansion waves to appear at the nozzle edge.

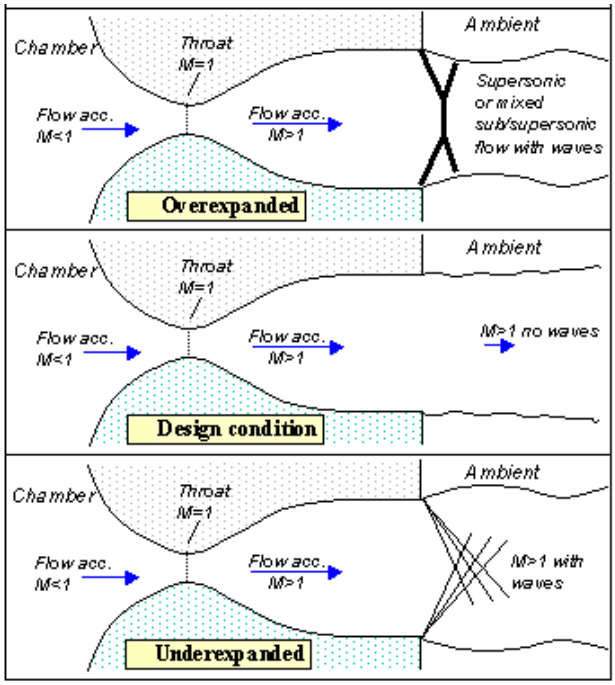

Figure 9: Supersonic flow patterns downstream a nozzle [18**].**

In the case of a fully expanded jet, the structure of the jet emerging from the nozzle includes a supersonic core immediately downstream the nozzle outlet followed by a subsonic region (**Figure 10**). The supersonic core is defined as the region where the Mach number remains essentially greater than one (**Figure 11**). Note that one may distinguish in the supersonic core a potential core region. In the subsonic region, the jet exhibits the same behaviour as described in **Section I.1.1.1**.

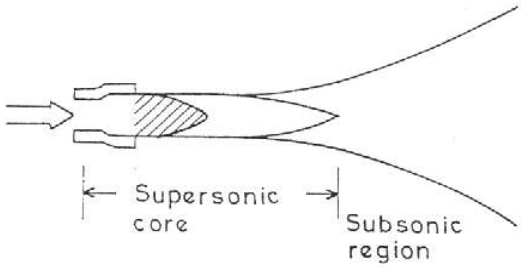

Figure 10: Structure of a supersonic gas jet [5].

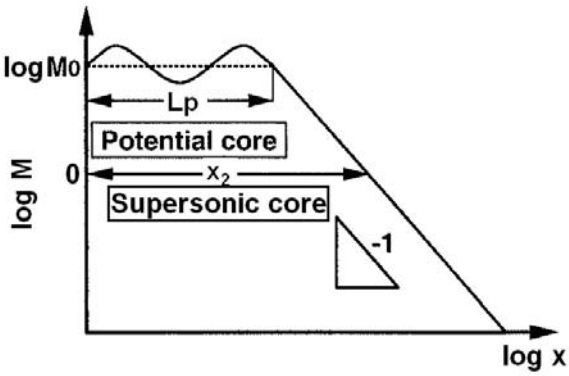

Figure 11: Schematic diagram of the jet decaying model [19].

<u>The potential core (Lp):</u> To calculate the length of the potential core, Okhotskii [**20**] proposed a formula as a function of the density ratio between the jet and the ambient gas.

$$Lp = 6.8 \frac{\rho_0}{\rho_{amb}} \qquad \textbf{Eq. 17}$$

Allemand et al. [**21**] have proposed a more complex correlation, which takes into account not only the difference between the jet and the ambient gas densities, but also the temperature and the Mach number of the jet in the outlet section and the ambient temperature.

$$\frac{Lp}{D_n} = \left(\frac{\rho_0}{\rho_{amb}}\right)^{1/2} \left[4.2 + 1.1\left(Ma_{outlet}^2 + 1 - \frac{T_{outlet}}{T_{amb}}\right)\right] \qquad \textbf{Eq. 18}$$

<u>The supersonic core (x_2)</u>

There have been many authors who investigated the supersonic core of a supersonic gas jet (e.g. Koria [**5**], Odenthal et al. [**22**]). In particular, several equations have been proposed to estimate the length of the supersonic core (see **Table 2**) as a function of the outlet Mach number (M_{outlet}), the inlet and ambient pressures (P_0 and P_{amb}) and the nozzle and throat diameters (D_n and D_t). In **Figure 12,** the estimates obtained using these equations are compared. We assumed that the nozzle is adapted (i.e. P_{outlet}=P_{amb}) and the Mach number at the nozzle outlet is calculated from **Eq. 15**. All the equations considered here give very similar results except the equation of Odenthal et al. [**22**] which leads to estimates of the

supersonic core length significantly lower than those obtained from the other equations. This difference between Odenthal equation and the equations of the other authors may be related to the high temperature of the ambient gas considered in Odenthal study. Indeed, at high ambient temperatures, the low density of the ambient gas results in a reduced mass addition to the jet from the ambient gas. The decrease of the jet velocity is then reduced.

Reference	Year	Supersonic core	Operating parameters		
			P_0(MPa)	T_{amb}(K)	
Koria [5]	1993	$\frac{x_2}{D_n} = 6.2\, Ma_{outlet}^{1.572\pm0.281}$	0.7 – 1.5	-	S
Naito et al. [19]	2000	$\frac{x_2}{D_t} = Ma_{outlet}\left(5.88 + 1.54\, Ma_{outlet}^2\right)$	0.39 – 1	300	E
Tago et al. [23]	2002	$\frac{x_2}{D_t} = 2.24\frac{P_0}{P_{atm}} + 6.16$	0.5 - 1	300	E
Odenthal et al. [22]	2007	$\frac{x_2}{D_t} = 14.446 \ln P_0 - 177.24$	0.3 – 1	1943	S

Table 2: A selection of the equations for the supersonic core length published in the literature (E: experiment; S: simulation).

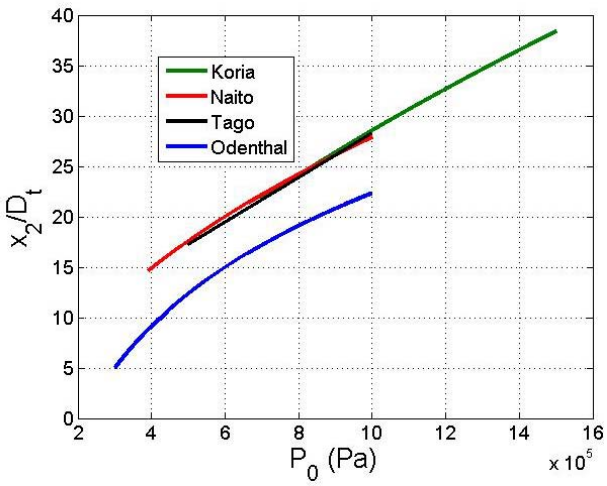

Figure 12: Comparison of the predictions obtained using the equations presented in Table 2.

Centreline Mach number and expansion angle of the jet

Naito et al. [**19**] carried out an experiment with a Laval nozzle blowing out a supersonic air jet. They measured the decaying of the centreline Mach number with a Pitot tube and found it to be related to the supersonic core length (**Eq. 19**).

$$Ma = \frac{x_2}{x} \quad (x > Lp) \qquad \textbf{Eq. 19}$$

Okhotskii [**20**] has proposed the following equation to describe the variation of the angle of the jet expansion as a function of the outlet Mach number:

$$\tan\theta = 0.19\ Ma_{outlet}^{-0.985} \qquad \textbf{Eq. 20}$$

I.2 Impingement of a gas jet onto a liquid surface

Eletribi et al. [**24**] described the forces exerted on a liquid surface when a gas jet impacts it. The deformable surface is subjected to four different forces: the impingement force of the jet, the shear force associated to the flow of gas along the surface, the surface tension force and the pressure force due to the induced recirculatory flow in the bath. As soon as the impingement force of the jet is higher than the surface tension force, a cavity is formed. The surface tension force increases with the surface area. When the upward and downward forces counterbalance each other, a "stable" cavity is obtained. Note that the higher the gas velocity, the higher the jet pressure force, the higher the recirculatory flow induced force and the shear force.

Among the forces listed below, it is important to know which ones are predominant. The capillary length is defined as the length scale at which gravity and surface tension forces are of the same order of magnitude.

$$l_c = \sqrt{\frac{\sigma}{\rho g}} \qquad \textbf{Eq. 21}$$

where σ, ρ and g are the surface tension, the density and the acceleration due to gravity respectively. The capillary length is around 2.7 mm for the water/air system and around 4.7 mm for the liquid steel/oxygen system. In a converter, the depth of the cavity formed at the liquid steel/oxygen interface is generally much higher than this latter value, so that the cavity creation is driven mainly by the gravity forces and the surface tension forces are negligible [**25**]. In contrast, for the case of the water/air interface, both regimes (gravity controlled or surface tension controlled) may be encountered depending on the blowing conditions [**26**].

Based on the force analysis aforementioned and experimental observations, three modes of jet impingement on a liquid surface have been described by Molloy [**27**]:

- Dimpling mode: a low dynamic pressure of the jet associated to a low gas velocity and/or a high lance height induces at the liquid surface a shallow cavity as represented on the left image of **Figure 13**. An analytical expression of the liquid surface profile in this mode has been proposed by Olmstead et al. [**28**].
- Splashing mode: when increasing the gas velocity and/or reducing the lance height, a production of outwardly directed droplets takes place (middle image on **Figure 13**).

- Penetrating mode: when increasing further the gas velocity and/or reducing the lance height, a diminution in the amount of droplets generated above the bath is observed. Obviously the cavity becomes deeper due to the higher dynamic pressure of the jet (right image of **Figure 13**). In the penetrating mode, Molloy [**27**] and Kumagai et al. [**29**] described the apparition of two additional phenomena: oscillation and swirl. The cavity side walls oscillate in the radial direction, and swirl around the nozzle axis. Note that the apparition of the oscillation and swirl is not related to an increase in the gas velocity.

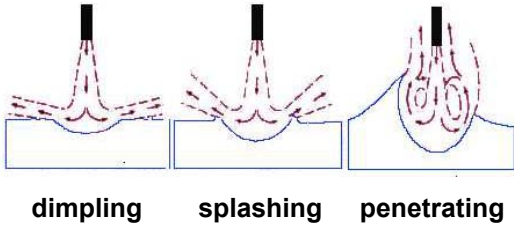

Figure 13: Surface deformation modes [30**].**

I.2.1 Cold and hot model experiments

There have been many experimental studies of gas jet impinging on a liquid bath, starting with the work of Banks and Chandrasekhara [**26**] in the early sixties until the recent work of Nordquist et al. [**31**]. Most of these works are based on cold model experiments (in which water is used to model molten steel and oxygen is replaced by air). There have been very few studies involving hot model experiments (i.e. oxygen-steel system) [**25,32,33**]. **Table 3** summarises a selection of the different experiments reported in the literature regarding the jet impingement onto a liquid pool. The operating parameters most often investigated are the nozzle diameter, the lance height and the gas flow rate. All these experiments aim essentially at visualizing and characterising the shape and dimensions of the cavity created by the jet at the liquid surface.

Reference	Year	Air-water	Oxygen-metal	Single nozzle	Multi-nozzles	Nozzle diameter	Nozzle angle	Bath height	Lance height	Flow rate	Vessel diameter	Operating parameters		
												Nozzle diameter (mm)	Lance height (mm)	Gas flow rate (10^{-3} $m^3.s^{-1}$)
Banks et al. [26]	1963	X		X		X			X	X		6.14-11.2	30-300	0.24-32.8
Cheslak et al. [34]	1969	X		X		X			X			1.4-8.7	50-180	-
Sharma et al. [25]	1977		X	X		X		X	X	X		17.1-20.6	80	2.83-5.18
Koria et al. [32]	1987		X	X	X		X	X	X	X	X	1.2	300-600	-
Qian et al. [35]	1996	X		X		X		X	X	X	X	5.8-23	15-210	0.13-3.33
Shimada et al. [33]	2000		X[1]	X		X			X	X		3-6	5-25	0.05-0.23
Kumagai et al. [29]	2001	X		X		X			X	X	X	1-4	-20 – 20[2]	0.003-0.08
Olivares et al. [36]	2002	X		X				X	X	X		1	20-100	0.25-0.3
Meidani et al. [37]	2004	X			X				X			0.5-1.5	76-250	24.5
Nordquist et al. [31]	2006	X		X		X			X	X		0.8-3	50-200	0.83-1.17

Table 3: Experimental studies in the literature regarding gas jet impinging onto a deformable surface ([1]Inert gas – slag experiments; [2] Negative values referred to experiments with immersed lance).

Banks and Chandrasekhara [**26**] carried out air-water model experiments to study planar and round jets considering laminar and turbulent flows. They concluded that the turbulent jet does not exert the same stagnation pressure as the laminar jet does. Whereas the viscous phenomena have a great influence on the induced flows in the liquid, they are unimportant regarding the cavity. They also concluded that the surface tension and specific weight of the liquid are important parameters when considering the cavity formation

Cheslak et al. [**34**] measured the depth of the cavity formed on wet fast setting cement as a result of gas jet impact. They compared their experimental results with predictions from a theory similar to that from Banks and Chandrasekhara [**26**] and found there was reasonable agreement.

Sharma et al. [**25**] performed hot experiments and determined that chemical reactions, high temperature and the presence of a slag layer above the bath do not affect the shape and the depth of the cavity. The depth is predominantly governed by the pressure. These authors also highlighted the fact that straight-bore and convergent-divergent nozzles lead to the same jet momentum (and therefore the same cavity depth) under the same blowing conditions.

Koria and Lange [**32**] carried out oxygen-steel experiments using single and multi-nozzle jets. They investigated the influence of the blowing parameters on the penetrability, which was defined as the ratio of the depth to the diameter of the cavity. The cavity width and depth were mainly influenced by oxygen pressure, lance distance and the number of nozzles.

Qian et al. [**35**] studied the influence on the surface cavity of a lighter liquid layer covering the liquid bath. They first tested a single-layered bath (only water in the bath), then a multi-layered bath (corn oil or kerosene above water). They proposed an improved correlation for the prediction of the depression depth, covering a wider range of operating parameters (in particular low lance height to nozzle diameter ratio) than previous correlations.

Shimada et al. [**33**] carried out experiments with a molten slag at 1673 K using an X-ray computed tomography technique to visualise the slag shape in the gas impact region. They tested several blowing conditions, using various inert gases (Ar, He, N_2) and different values of lance diameter and gas flow rate. They concluded that the depression is of columnar shape and that the penetration depth increases with the gas momentum.

Kumagai and Iguchi [**29**] carried out two different types of experiments: the first one with the lance above the bath surface and the second one with the lance immersed in the bath. They classified the deformations of the liquid surface into seven categories as a function of gas flowrate and lance height and investigated more particularly the dynamic of the cavity (swirl motion).

Olivares et al. [**36**] used a one eighth air-water model of a LD converter with top-, bottom- and combined-blowing to characterise the mixing time in the bath and the jet penetration. They conducted both an experimental and a numerical study and established a correlation for the jet penetration as a function of a modified Froude number.

Meidani et al. [**37**] tested a new lance design (shrouded supersonic jets) in a water model. After a dimensional analysis, they studied the jet penetration in the bath and compared their results with the predictions of a mathematical model. The new lance was found to have better performances: it increases the penetration depth.

Nordquist et al. [**31**] reviewed many studies of gas jet impacting on a liquid surface. They also investigated the penetration of an impinging air jet onto a water pool, with particular focus on the effect of small nozzle diameters. It was shown that their measurements of the penetration depth cannot be represented satisfactorily by existing literature correlations in the case of nozzle diameters smaller than 2 mm. A new correlation for this latter range of nozzle diameter was then derived.

I.2.2 Analytical models of the cavity depth

Table 4 summarises the main equations established in the literature to calculate the depth of the cavity (h_c) formed by a gas jet impinging onto a liquid pool. These equations are semi-empirical correlations, i.e. they are based (for some of them) on some basic theoretical arguments but involve empirical coefficients. It should be emphasised that all these equations relate to a single layer liquid bath (except the improved correlation of Qian et al. [**35**]) and are established for an air-water model (except the oxygen-metal model of Koria and Lange [**32**]) with subsonic gas jet velocities.

The operating parameters appearing most frequently in the formulae listed in **Table 4** include the lance height, the jet velocity at the nozzle exit, the diameter of the nozzle and the liquid and gas densities. The different approaches used to derive these correlations may be classified into three categories (as initially proposed by Banks and Chandrasekhara [**26**]):

- The basic approach is a dimensional analysis which consists of reducing the number of the factors which can influence the cavity depth.
- A first theoretical approach is the displaced liquid analysis based on the assumption that the force associated to the gas jet impact is equal to the weight of the liquid displaced from the cavity.
- A second theoretical approach is the stagnation pressure analysis. The cavity depth is estimated by equalizing the pressure force of the gas at the stagnation point and the hydrostatic pressure associated to the height of the liquid depression. This approach was further developed by Qian et al. [**35**] who have proposed an improved estimation of the gas velocity near the stagnation point for the calculation of the stagnation pressure.

Reference	Year	Cavity depth equation	Q ($10^{-3}m^3.s^{-1}$)
Banks et al. [26]	1963	$\frac{h_c}{h_n}\left(1+\frac{h_c}{h_n}\right)^2 = \frac{125}{\pi}\frac{M}{\rho_\ell g h_n^3}$	0.24-32.8
Huin [38]	1986	$h_c = 5300\left(\frac{Q}{D_n}\right)^{2/3}\exp\left[-0.78\frac{h_n}{5300\left(\frac{Q}{D_n}\right)^{2/3}}\right]$	-
Koria et al. [32]	1987	$\frac{h_c}{h_n} = 4.469\left[\frac{0.7904.10^5}{\rho_\ell g}\frac{D_n^2}{h_n^3}P_{amb}\left(1.27\frac{P_0}{P_{amb}}-1\right)\cos\alpha\right]^{0.66}$	-
Qian et al. [35]	1996	$\frac{M}{\gamma_{\ell mix}^{**} h_c D_n^2} = F^*$	0.13-3.33
Kumagai et al. [29]	2001	$h_c = 4.1D_n\left[\left(\frac{4}{\pi}\right)^2\frac{\rho_G U_G^{2***}}{\rho_\ell g D_n}\right]^{1/3}$	0.003-0.08
Olivares et al. [36]	2002	$h_c = 1.508\frac{D_n^2}{h_n}\left[\frac{\rho_G U_m^2}{(\rho_\ell-\rho_G)gD_n}\right]^{0.714}$	0.25-0.3
Nordquist et al. [31]	2006	$h_c = \frac{\rho_G U_0^2}{2g}\frac{5.159.10^{-9}}{0.01059h_n - D_n/2}$	0.83-1.17

Table 4: Formulas for the cavity depth.

$$^{*}F = \begin{cases} 1.04 & if \quad 0 < \frac{h_n+h_c}{D_n} < 3.5 \\ 0.84 + 0.0072\left(\frac{h_n+h_c}{D_n}\right)^2 + 0.024\left(\frac{h_n+h_c}{D_n}\right)^2 & if \quad 3.5 < \frac{h_n+h_c}{D_n} < 10 \\ \frac{\pi}{K_2^2}\left(\frac{h_n+h_c}{D_n}\right)^2 & if \quad \frac{h_n+h_c}{D_n} > 10 \end{cases}$$

$$^{**}\gamma_{\ell mix} = \frac{h_{c1}}{h_c}\gamma_{\ell 1} + \max\left[\gamma_{\ell 1}\left(1-\frac{h_{c1}}{h_c}\right), \gamma_{\ell 2}\left(1-\frac{h_{c2}}{h_c}\right)\right]$$

$$***U_G = \begin{cases} U_m & if \quad \frac{h_n}{D_n} < 1.26 \\ \dfrac{U_m}{0.00523\left(\frac{h_n}{D_n} - 1.26\right)^2 + 1} & if \quad 1.26 \le \frac{h_n}{D_n} < 17.2 \\ \dfrac{U_m}{0.167\left(\frac{h_n}{D_n}\right) - 0.543} & if \quad \frac{h_n}{D_n} \ge 17.2 \end{cases}$$

Where h_n and D_n are the height and the diameter of the nozzle respectively. ρ_ℓ and ρ_G are the liquid and gas densities respectively. Q is the flowrate and M the jet momentum, α the inclination angle of the lance and γ_ℓ the liquid specific weight.

I.2.3 Modelling studies

The modelling approaches employed for simulating gas jet impingement on a liquid surface have gained in complexity over years with the development of the modelling and numerical simulation techniques. The first simulations, beginning in the seventies by the work of Szekely and Asai [**39**], were done with in-house codes for a 2D geometry with a fixed shape of the surface cavity, while the most recent ones (in the last decade) use a commercial CFD code with free surface tracking algorithms (e.g. Odenthal et al. [**22**]).

Table 5 summarises the different computational studies reviewed in this section. It also presents the main features of each model (e.g. the geometry, the turbulence model used, the range of velocities).

Reference	Year	Geometry	Phases	Turbulence model	Multiphase model	CFD software	Experimental data used to evaluate the accuracy of the model	Range of the Mach number
Szekely and Asai [39]	1974	2D	Air-water, Oxygen-metal	k		In-house code	Wakelin [**40**]	-
Zhang et al. [41]	1985	2D	Air-water	k-ε (S)		In-house code	Zhang et al. [**41**]	Ma ~ 0.16
Olivares et al. [36]	2002	2D	Air-water	RNG k-ε	VOF	-	Olivares et al. [**36**]	Ma ~ 1
Nguyen and Evans [42]	2006	2D	Air-water	k-ε (S)	VOF	FLUENT [**43**]	Zhang et al. [**41**] Banks et al. [**26**]	0.16 <Ma< 0.3
Ersson et al. [44-46]	2006 - 2008	2D	Air-water, Oxygen-slag-metal	k-ε (S, R, SM)	VOF	FLUENT [**43**] Thermo-Calc [**47**]	Banks et al. [**26**]	0.15<Ma<0.4
Balabel [30]	2007	2D	Air – silicon oil	k-ε (S)	Level Set	FLUENT [**43**]	Wygnanski and Fiedler [**27**] Cheslak et al. [**34**] Eletribi et al. [**24**]	0.02<Ma<0.05
Barron et al. [48]	2008	2D	Oxygen-metal	k-ε (S)	VOF	-	-	1.0<Ma<1.5
Hwang [14]	2008	2D	Air-water, Oxygen-metal		VOF	In-house code	Hwang [**14**]	0.39<Ma<0.4
Odenthal et al. [22]	2007	3D	Oxygen-slag-metal	k-ε (S)	VOF	FLUENT [**43**]	-	1.9<Ma<2.4

Table 5: Computational studies in the literature dealing with the impingement of a gas jet onto a free surface reviewed in this chapter.

(S: standard variant; R: realizable variant and SM: standard variant with modified coefficients)

The first wave of computational studies [**39,41**] takes only the bath into account. The jet is not included in the computational domain. Moreover, the cavity shape is presumed and not allowed to evolve in the simulation. We can underline the fact that the equations of the continuity equation, and the transport equations of momentum and turbulent kinetic energy were written in terms of the vorticity and the stream function in those models.

Firstly, in the seventies, Szekely and Asai [**39**] developed a 2D mathematical representation of the bath of a top-blowing converter with a more particular focus on the liquid movement in the bath induced by the impinging gas jet. They analysed the vorticity, velocity and turbulent energy fields computed in different liquid baths (water, molten steel and mercury). The computed velocity profiles were shown to be in agreement with the experimental data reported by Wakelin [**40**] for a CO_2-water system.

Later, Zhang et al. [**41**] simulated a 1/9 model of a 30-ton converter using a similar approach to that of Szekely and Asai, but considering a k-ε turbulence model. Their mathematical model accounts for the simultaneous action on the bath of a symmetrically placed impinging gas jet and a submerged gas stream. A similitude study was conducted to identify the most important parameters. They found the computed results to be in satisfactory agreement with experimental data obtained by laser Doppler anemometry.

The second wave of computational studies is based on the classical RANS approach and considers a deformable bath free surface. Olivares et al. [**36**] simulated a 1/8 air-water model of a LD converter. The simulation was done for the case of a 2D geometry using the RNG k-ε turbulence model and the VOF model to deal with the two phases. The gas jet has been treated as incompressible despite the sonic velocity values considered in the simulations. The thermodynamic was out of interest in this study so that an isothermal calculation was performed. Olivares et al. [**36**] concluded on the importance of the modified Froude number for the characterisation of the jet penetration depth in the bath and reported a cyclic rippling deformation of the bath surface.

Nguyen and Evans [**42**] computed an impinging gas jet onto a liquid pool by using a standard k-ε turbulence approach and the VOF model in a 2D axisymmetric geometry formulation. The interface was reconstructed with the geo-reconstruct (piecewise-linear) scheme implemented in the software FLUENT [**43**]. The calculated streamlines and the centreline velocity of the gas jet were found to be in good agreement with the experimental results of Zhang et al. [**41**]. The predicted cavity depth agreed well with the estimate obtained using the formula of Banks and Chandrasekhara [**26**]. Moreover, the jet centreline velocity U_m could be well fitted with the following equation:

$$\frac{U_m}{U_0} = \frac{K_1}{z / D_n + K_0}$$ where K_1 = 8.4 and K_0 = 7.7.

Ersson and co-workers [**44-46**] have developed an original model which accounts for the coupling of fluid mechanics and thermodynamics phenomena in a top blown converter. The first step made by Ersson et al. [**44**] was to investigate the performance of different turbulence models available in the software FLUENT [**43**]. The authors noticed that albeit the standard k-ε gives better results for the penetration depth of the jet in the bath, it failed to estimate the right location of the main recirculation loop of the induced flow in the bath. On the contrary, the realizable k-ε was able to better predict the position of the main recirculation loop in the bath and to satisfactorily approximate the penetration depth. In a second step [**45**], the fluid mechanics model was coupled to the thermodynamic equilibrium calculation software THERMOCALC [**47**] in order to predict the reaction rate in the vessel. The CFD computations were based on a VOF model and the realizable k-ε turbulence model. The simulations were made for the case of an oxygen-liquid steel system. The concentrations of five different species were calculated, namely the concentrations of C and O dissolved in the liquid and those of O_2, CO and CO_2 in the gas phase. The authors have compared their computational results with the experimental carbon concentration in the droplets measured by Nordquist et al. [**31**]. Finally, the last step [**46**] is an improvement of the previous approach to take into consideration reactions in the gas-slag-steel system. As expected, the authors concluded that the convection is the dominant mass transport mechanism in the surface area. For the conditions considered in the paper, it was found that almost no slag was created.

Balabel [**30**] modelled an incompressible gas jet impinging onto the deformable surface of a silicon oil bath. In contrast to the approach most commonly used by others authors, the Level Set Method was used as multiphase approach. The numerical results for the jet part were compared to the experimental data of Wygnanski and Fiedler [**27**]. The model gives cavity depth predictions in-between the estimate provided respectively by Cheslak et al. [**34**] formula and that of Eletribi et al. [**24**]. The model over-estimates the cavity width.

Barron et al. [**48**] investigated numerically a new blowing lance design which comprises four peripheral conventional nozzles and one vertical centred nozzle. The 2D mathematical model, developed for the case of an oxygen-steel system, uses the VOF and k-ε turbulence models without consideration of chemical reactions and heat transfer. Note also that the assumption of incompressible flow was used in their approach despite the supersonic velocity of the gas jet. The simulations have been conducted for the case of a 150-ton BOF for different values of the Mach number and the lance height. The authors concluded that the new lance design increases the bath agitation and the droplet generation.

The modelling approach used by Hwang [**14**] is restricted to the case of an incompressible gas and does not include any turbulence model. One specific feature of the model developed by Hwang is the use of the full stress boundary conditions at the liquid-gas interface for a more accurate description of the momentum transfer between the gas and the liquid. Numerical simulations are performed for the case of air impinging onto a water bath and the case of oxygen impinging onto a steel bath in a full scale converter. The author noticed that in the case of the air-water system, the cavity width predicted by the mathematical model is two to three times greater than in the experiments and that the cavity depth is well estimated only at low gas flow rate. He concluded that the model has to take into account the gas compressibility and temperature variations to better capture the surface cavity shape and dimensions. Another key of discrepancy of the model could be related to the lack of turbulence modelling in his model.

Recently, a major step forward for the modelling of an oxygen converter has been made by Odenthal et al. [**22**] who developed a 3D model of the BOF and AOD converters considering a 3-phase system (oxygen-slag-metal). Using a separate model, they simulated the compressible flow of a gas jet exhausting from a convergent-divergent (Laval) nozzle to analyse the waves in an imperfectly expanded supersonic jet. A formula was derived from the simulation results to determine the length of the supersonic core as a function of the nozzle outlet diameter and the oxygen supply pressure (see **Table 2**). The BOF model was applied to the simulation of a 335-ton combined-blowing converter. The model takes into account energy transport, turbulent flow phenomena, interfacial deformations and gas bubble behaviour. The three interfaces (oxygen-slag, slag-steel and steel-oxygen) are tracked with the VOF method. In contrast to the nozzle model, the gas is considered as incompressible in the converter model, however values of the characteristic parameters of the jet have been adjusted in order to produce a similar momentum along the jet axis as that obtained from the compressible nozzle model. Additionally, chemical reactions and slag foaming were not accounted for.

In conclusion, it should be stressed that the hydrodynamics simulations of the steelmaking converter described so far in the literature to our knowledge did not take into consideration the compressible character of the gas jet at high velocities (M > 0.3). In addition, the simulations were isothermal except in the works of Ersson and co-workers [**44-46**] and Odenthal et al. [**22**]. Most of the researchers consider a 2D geometry except Odenthal et al. [**22**] who presented a 3D model. The most used multiphase approach was the VOF model except in the work of Balabel [**30**] who used the Level Set Method. Among the different simulations cited in this report, we can highlight the work of Odenthal et al. [**22**] who

developed a 3-phase model in a 3D geometry, the one of Ersson and co-workers [**44-46**] who took into consideration the thermodynamics aspects and the thesis of Hwang [**14**] who, in contrast to the other researchers, took into account the full stress boundary conditions at the gas-liquid interface.

I.3 Generation of liquid droplets

I.3.1 Experimental studies

Reference	Year	Phases	T (°C)	Q_{top} (Nm^3/min)	Lance angle (deg)	Lance height (m)
Koria and Lange [**49**]	1984	Oxygen-metal	1450	0.03-0.15	0-20	-
Standish and He [**50**]	1989	Nitrogen-water	20	0.032-0.066	0	0.02-0.2
He and Standish [**51**]	1990	Air-water Air-glycerine-mercury	20	0.03-0.09	0	0.02-0.2
He and Standish [**52**]	1990	Air-glycerine-mercury	20	0.057-0.086	0	0.01-0.05
Higuchi and Tago [**53**]	2001	Air-water Oxygen-pig iron	20 -	0.84 0.6	10-15 12-24	0.2 0.4
Luomala et al. [**54**]	2002	Air-liquid soap-water	20	0.025-0.05	15	0.16-0.22
Subagyo et al. [**55**]	2003	Nitrogen-slag-metal	1600-1750	0.0618-0.084	-	0.04-0.06
Higuchi and Tago [**56**]	2003	Air-water	20	0.84	20	0.2
Koohi et al. [**57**]	2008	Air-water	20	0.065-0.095	36.8-101.5	-0.05 to 0.2

Table 6: Selection of experimental studies in the literature on liquid droplets resulting from gas jet impingement on a liquid bath.

Table 6 summarises a selection of the experiments made to investigate the liquid droplets generated by the impingement of a gas jet on a liquid surface. The authors have employed most often cold experiments with different gas flow rates, nozzle angles and lance heights. There are only few works on the production of droplets from the surface of high temperature liquid metal bath. Most studies are concerned with the determination of the droplet generation rate. Among the studies detailed in **Table 6**, only three groups of authors have characterized the droplet size distribution [**50,55,49**], the knowledge of this latter parameter being with that of the droplet generation rate of great importance for the determination of the overall interfacial area associated to the liquid droplets.

He and Standish [**51**] identified two modes of droplet generation (**Figure 14**): dropping which refers to the generation of individual droplets and swarming corresponding to the production of large tears of liquid. The transition between dropping and swarming was found to occur for a Weber number (ratio of the inertial forces to the surface tension forces) of around 40.

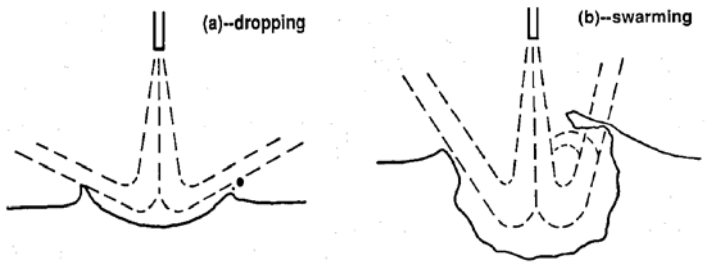

Figure 14: The two modes of drop generation [51**].**

Any factor which is able to increase the shear force at the cavity surface and/or the velocity of the liquid surface can increase the rate of droplet generation. Higuchi and Tago [**53**] found the generation rate to decrease when increasing the inclination or the twisted angle of the nozzle. Luomala et al. [**54**] reached the same conclusion and also found the generation of droplets to be decreased by the presence of a foamy slag (liquid soap in their experiment). Like Standish and He [**50**], Koohi et al. [**57**] have pointed out that when the lance is too close to the bath, the ejected droplets are entrained back in the bath by the jet. Subagyo et al. [**55**] have introduced from their hot experiment a new dimensionless number, the blowing number N_B, which is the ratio of inertia forces due to blowing to the square root of the product of surface tension and buoyancy forces.

$$N_B = \frac{\eta^2}{2} \frac{\rho_G U_m^2}{\sqrt{\sigma g \rho_\ell}} \qquad \textbf{Eq. 22}$$

where η is a constant ($\eta = 1/\sqrt{5}$), U_m the jet centreline velocity and σ the surface tension. Subagyo et al. [**55**] have shown that the onset of splashing corresponds to a critical value of the parameter N_B equal to 1. They have established an empirical relation between the droplet generation rate and the blowing number which fits well with their experimental data (hot system) and the data obtained by Standish and co-workers [**50,52**] (cold system).

$$\frac{R_B}{F_G} = \frac{(N_B)^{3.2}}{\left[2.6\times10^6 + 2.0\times10^{-4}(N_B)^{12}\right]^{0.2}} \qquad \textbf{Eq. 23}$$

where R_B is the generation rate of metal droplets (kg/s) and F_G the volumetric gas flow rate at normal condition (P=1 atm and T=273 K).

Concerning the droplet size, Standish and He [**50**] reported that the increase of the jet momentum at the bath surface increases the proportion of large droplets. It was found that

the drop size distribution can be satisfactorily represented by a normal distribution. In contrast, Koria and Lange [**49**], who carried out hot experiments during which a crucible filled with molten pig iron was used and the droplets falling outside the crucible were collected and analysed, found the drop size distribution to follow the Rosin-Rammler-Sperling distribution:

$$R = 100 \exp\left[-\left(\frac{d}{d'}\right)^n\right] \qquad \textbf{Eq. 24}$$

where R is the cumulative weight in percent of droplets with diameter greater than d, d' is the abscissa (droplet diameter) where the ordinate R is 36.8% and n the distribution exponent. In the experiments of Koria and Lange [**49**], n was found to be equal to 1.26. Subagyo et al. [**55**] used a regression analysis to correlate N_B and d': $d' = 12.0\,(N_B)^{0.82}$

Regarding the mean residence time of the droplets in the "slag phase" (i.e. glycerine in the authors experiments), He and Standish [**52**] found it to increase with top gas flow rate and height from which the droplets are ejected. Also, the increase in droplet size decreases the mean residence time. A mean residence time value of one minute has been found from their experiments.

I.3.2 Mechanisms of droplet generation

Two main mechanisms of droplet generation have been identified [**57**]:

- The displacement of the liquid gas associated to the formation of the cavity. Indeed, the penetration of the gas jet into the liquid creates the displacement of the bulk of the liquid. Large liquid drops are then ejected in the gaseous part.
- The Kelvin-Helmholtz (KH) instability.

The KH instability occurs when two stratified fluids are in relative motion. This instability results from the competitive effects [**58**] of the inertia forces and the pressure forces to which can be added (depending on the case) the gravitational effect and the interfacial force. In **Figure 15**, we denote U_C the velocity of the continuous phase (gas or slag in our case) and U_d the velocity of the dispersed phase (molten steel in our case).

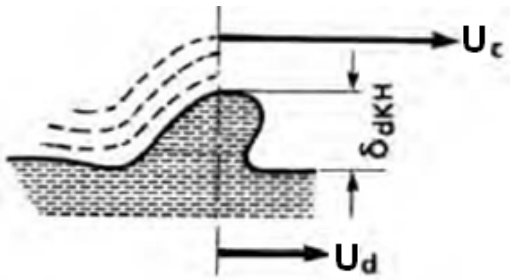

Figure 15: Wavelength of Kelvin-Helmholtz [58**].**

The velocities of the dispersed and continuous phases should be enough different to destabilise the surface of the dispersed phase. The instability occurs when the absolute difference between the two velocities is higher than a critical value as written in **Eq. 25**.

$$U_{Cd} = |U_C - U_d| > U_{CR} = [(\rho_d - \rho_c) g \sigma_d]^{1/4} \left(\frac{2(\rho_d + \rho_c)}{\rho_d \rho_c} \right)^{1/2} \quad \textbf{Eq. 25}$$

When the interface is unstable, the most unstable wavelength, known as the KH wavelength, is given by the equation:

$$\delta_{d,KH} \approx 3\pi \left(1 + \frac{\rho_C}{\rho_d} \right) \frac{\sigma_d}{\rho_c U_{Cd}^2} \quad \textbf{Eq. 26}$$

For instance, U_{CR}=6.67 m/s and $\delta_{d,KH}$ = 12.8 mm for air-water system.

To analyse the KH instability, it is of common practice to introduce the Weber number of the dispersed phase which is defined as the ratio of the shear force to the surface tension force (**Eq. 27**). In others words, this number is the ratio of the forces acting to destroy the droplet to the forces acting to retain the droplet form.

$$We_d = \frac{\rho_C D_d U_{Cd}^2}{\sigma_d} \quad \textbf{Eq. 27}$$

The KH instability occurs when $We_d \geq We_{dCR}$. In most of the experimental studies, the reported value of the critical Weber number (We_{dCR}) is between 5 and 20. A value of 12 is generally accepted [**58**].

I.4 Post-combustion

The oxygen from the lance reacts with the species contained in the metal bath. The reaction with the carbon leads to carbon monoxide CO which escapes from the metal bath. Once in the gaseous phase, CO reacts with the oxygen: this is the <u>post-combustion</u> reaction.

$$CO + 1/2O_2 \rightarrow CO_2 \quad \textbf{Eq. 28}$$

The combustion of CO by the oxygen is highly exothermic (it releases more than twice energy than the oxidation of carbon in the bath [**59**]). Investigations are performed to promote the transfer to the bath of the heat produced by this reaction in order for example to allow for the melting of a larger amount of scrap addition in the metal bath. The more CO is combusted by oxygen, the higher the heat available for the bath. The post-combustion ratio (PCR) is defined as the ratio between the concentration of carbon dioxide and the total concentration of CO_2 and CO.

$$PCR = \frac{\%CO_2}{\%CO + \%CO_2} \times 100 \quad \textbf{Eq. 29}$$

One of the earliest models of the post-combustion in a converter is the model of Hirai et al. [**60**]. The phenomena taken into account are displayed in **Figure 16**. The post-combustion occurs at the boundaries of the jet between oxygen and CO entrained inside the jet. Moreover, the CO_2 in the jet periphery can be in contact with either the metal or the slag. When in contact with the metal, it may be reduced to CO. In contrast when in contact with slag, it will not be reduced.

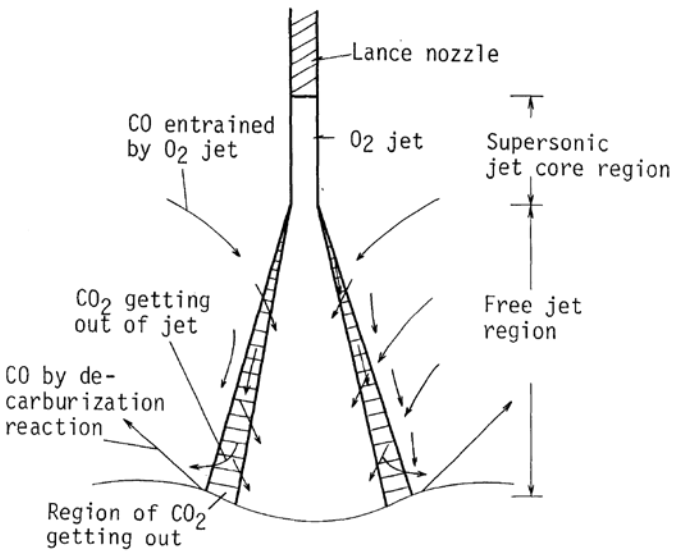

Figure 16: Post-combustion model [60**].**

Hirai et al. [**60**] have developed more particularly a set of equations to predict the post-combustion ratio. They also conducted experiments in a 250-t converter and in a 10-t ladle, and investigated the effect of changing various parameters, such as the lance design (testing the use of different number of nozzles), the oxygen flowrate and the lance height. Hirai et al. [**60**] found the post-combustion ratio to be a function of the oxygen flowrate, nozzle throat diameter and the lance height (**Eq. 30** and **Eq. 31**).

$$PCR = \frac{\sum_{ij} PCR_i \times \beta_{ij} \times Q_{O_2 i}}{\sum_i Q_{O_2 i}} \qquad \textbf{Eq. 30}$$

where β_{ij} is the interference factor between the jets (β_{ii}=1, β_{ij}=0) and Q_{O2i} is the oxygen flowrate in Nm^3/h from the nozzle i.

$$PCR_i \approx 0.1\left(\frac{h_n}{D_t}\right)^{0.8} - \left(\frac{h_n}{D_t}\right)^{-0.7} + 0.01 \qquad \textbf{Eq. 31}$$

where h_n and D_t are the lance height and the nozzle throat diameter respectively.

The above equations for the PCR were found to fit well the experimental data. It should be highlighted that this model neglects the effects of the slag foaming and the CO_2 reduction by the dust.

Another study on the post-combustion which should be highlighted is the experimental work conducted at ArcelorMittal Maizières and reported by Huin et al. [**61**]. This experiment was carried on a 6-t pilot with hot metal containing around 4% carbon and others species (Mn, P, S and Si). The oxygen in this experiment was blown at 1 to 2.4 Nm^3/min.t from a single hole lance vertically located at 1 to 2.2 m above the bath surface. The measurements were conducted with a gas sampling lance inside the gaseous phase and with a gas analysis of the off-gases. Unlike the previous experiment by Hirai et al. [**60**], this study investigated the effect of the addition of scrap (40-100 kg/t). It was observed that the PCR increases when increasing the scrap addition. Another parameter not studied in the previous experiment is the influence of the bottom stirring. The variation of the bottom stirring flowrate between 0.12 and 0.42 Nm^3/min.t informs us that the PCR is promoted by a low bottom stirring flowrate.

From the different measurements describe above, performed in 250- [**60**], 10- [**60**] and 6-t [**61**] converters, it emerges that the PCR can be increased by:

- A decrease of the <u>total oxygen flow rate</u>. The PCR is increased by soft blowing, because the latter promotes the entrainment of CO into the oxygen jet.
- An increase of the <u>lance height</u>. Indeed, increasing the lance height increases the volume of CO which can be entrained and combusted.
- A decrease of the <u>slag foaming height</u>.
- A decrease of the <u>bath temperature</u>. A low bath temperature is suitable to the production of slag.
- A decrease of the <u>carbon content</u>. In this case, more oxygen is available for the post-combustion so it increases the PCR.
- An increase of the <u>scrap ratio</u> into the converter which decreases the temperature of the bath.
- A decrease of the <u>bottom flowrate</u>. Indeed, when increasing the bottom flowrate, we increase the CO_2 reduction by the bath.

It is important to have a realistic model to know the importance of each parameter on the variation of the PCR to optimize the process. One should also note that the PCR is high in the early stage of blowing (due to the operating parameters and the resulting effects e.g. slag

foaming, bath temperature, etc.), decreases with an increase in blowing time and increases again at the final stage [**61**].

From Huin et al. [**62**] to Nakazono et al. [**63**], several models of the gaseous phase in a converter have been developed to better predict post-combustion phenomena. A selection of these mathematical models is described below.

At ArcelorMittal, a post-combustion model has first been developed by Huin et al. [**62**] and has been later used by Huber et al. [**64**] in a global dynamic model of the converter. Besides the oxidation of CO, this model takes into account the recirculation of exhaust gases in the post-combustion flame. As we can see on **Figure 17**, the rate of oxygen not reacting with the bath at the impact has been taken into consideration to know the amount of oxygen available for the post-combustion. Moreover, the entrainment of the carbon monoxide into the oxygen jet has been tackled. The reaction between the carbon dioxide and the carbon (reoxidation) in the bath has also been modelled. It should be stressed that this model is built around the hypothesis that the jet has a constant opening while getting away from the lance tip. Other weaknesses of the model are the constant pressure all inside the vessel, the crude estimation of the radiative heat flux and the velocity estimation outside the jet. Taking as inlet parameters the velocity of oxygen, the temperature of oxygen and ambient gas, the lance height and the diameters of the nozzle and converter, this model enables to predict the temperature and the composition inside the gas jet by solving the momentum, mass and energy conservation equations.

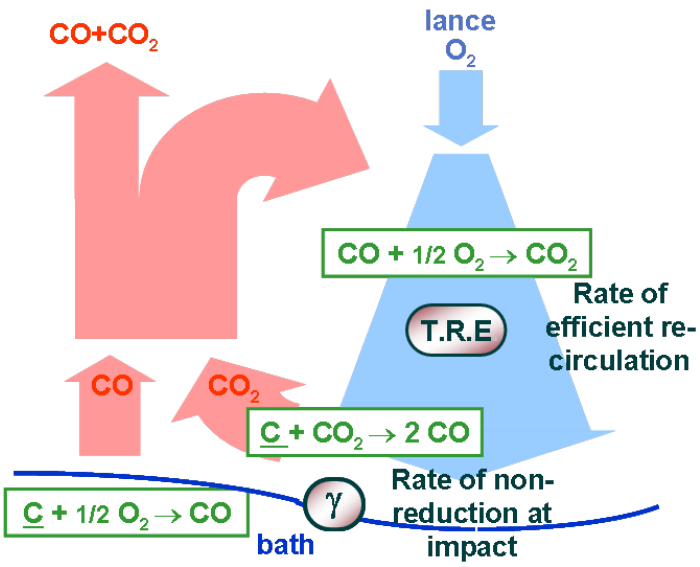

Figure 17: ArcelorMittal post-combustion model [64].

The ArcelorMittal model shows very good agreement with the gas analysis made in a 6-t pilot at Maizières [**61**].

Zhang and Oeters [**65,66**] developed an in-house code model more sophisticated than the one of Huin et al. [**62**], taking into account the following phenomena:

- Reactions of decarburisation (through O_2 and CO_2) and post-combustion. The dissociation of CO_2 has also been taken into consideration. Whereas it remains unimportant for temperatures lower than 1900°C, at 2800°C 50% of the CO_2 is dissociated.
- Heat transfer:
    - Macro kinetics (population of droplets in the gas). Heat is brought from the gas to the melt through droplets falling back to the bath
    - Micro kinetics (single droplet) with radiation and convection
    - Neglecting of heat losses via the walls
- Lagrangian droplet behaviour

The model was tested on a 170-t bottom-blown oxygen converter with a top-lance above the melt. According to the model, the heat transfer via metal droplets is limited by the reduction of CO_2 at the droplet surface (endothermic reaction). In contrast, heat transfer through the slag droplets is more efficient since these droplets are not directly affected by the reduction of CO_2. Moreover, the radiative heat was found to represent 20% to 60% of the total heat transfer in the gaseous phase.

Later, Gou et al. [**67**] developed a 2D CFD type model of the turbulent gaseous phase of a converter with radiative (Demarco-Lockwood radiation flux model) and convective heat transfer. Unlike the model by Zhang and Oeters [**65,66**], this model does not study the case of a bottom-blown converter. The chemical reactions have been described through the finite chemical reaction rate model with the reaction rate determined with the Arrhenius expression. The oxygen gets into the bath at the jet impingement area and the CO rate from the bath is set to follow an exponential profile over the radius of the vessel. With the help of this model, the authors have investigated the parameters which enable to increase the PCR and they have demonstrated the importance of radiative heat transfer. On the other hand, they found, by comparing the predictions of their model to Dofasco's industrial results, that the heat recovered by the bath is overestimated by 20%. This discrepancy was attributed to the fact that the model does not take into account the losses through the vessel and lance walls. Finally, Gou et al. have shown that the location of the post-combustion can be controlled, up to a certain point, by adjusting the lance practice.

Nakazono et al. [**63**] have modelled a supersonic O_2-jet impinging a hot (1840 K) liquid iron surface and studied the species distributions. Besides solving the conservation equations of mass, momentum, energy, this model considers the cavity geometry, which is determined from a balance between pressure, shear stress, surface tension and liquid buoyancy forces. Regarding the reactions, the forward and the backward reactions occurring between C, CO, CO_2, O_2 and O are all taken into account. The probability for the surface reaction which is defined as the probability of a specie to react at a certain temperature at the cavity surface, has been found using the Park ablation model or has been taken equal to 1. In this model, the oxygen is blown at Mach 1.0 from a nozzle located 3 cm above the bath surface. They found that non-equilibrium effects (different translational-vibrational and vibrational temperatures) are important only for CO_2. The probability of surface reaction changes slightly the mass fraction of oxygen at the cavity surface. Outside the cavity, the surface reactions are active and the dominant species is CO when the Park ablation model is used. One should also note that in their results, Nakazono et al. didn't find the cavity dimensions to be changed depending on the probability model used.

I.5 Conclusions

This literature review chapter was devoted to four main important aspects of an oxygen converter: the behaviour of the gas jet, the impingement of the gas jet onto the liquid surface, the generation of liquid droplets from the bath and the post-combustion reaction in the gaseous phase.

After describing the behaviour of subsonic and supersonic gas jets, a review of the previous studies investigating the cavity created at a liquid surface due to an impinging gas jet has been presented. Most of these studies are based on air-water experiments and disregard some important features of the BOF (such as the supersonic regime of the flow and the presence of a slag layer above the bath). On the modelling side, the most commonly approach to describe the surface deformation is the VOF method. The gas jet is treated as incompressible and the consideration of the compressible character of the gas jet at high velocities (Ma > 0.3) is still to be completed. Among the different models reviewed, we can highlight the work of Odenthal et al. [**22**] who developed a 3-phase model in a 3D geometry, the one of Ersson and co-workers [**44-46**] who took into consideration the thermodynamics aspects and the thesis of Hwang [**14**] who, in contrast to the other researchers, took into account the full stress boundary conditions at the gas-liquid interface. Various experimental investigations about the production of liquid droplets during the jet impingement have been reported. It was shown that the Weber number and the Blowing number are two important

parameters for analysing this phenomenon. Regarding the post-combustion in the gaseous phase, a number of experimental studies have shown that the PCR can be increased by an increase of the lance height and the scrap ratio or by a decrease of the total oxygen and the bottom flowrates, the slag height, the bath temperature and the carbon content. A few models have also been reported, going from the simplified jet model of Huin et al. [**62**] to the more complex model of Nakazono et al. [**63**], which is the only one to take into account the cavity geometry. The model of Zhang and Oeters [**65,66**] should be highlighted also since it takes into account the droplets of metal and slag in the gaseous phase. Finally, it should be mentioned that, to our knowledge, there are no papers dealing with the full coupling between the impinging jet problem and post-combustion phenomena in an oxygen converter.

Chapter II Impingement of a jet onto a liquid surface: numerical model

II.1 Mathematical model

The mathematical model presented in this chapter aims to represent the impingement of a gas jet onto a liquid surface. It describes the dynamics of the gas phase and the liquid phase, and the deformation of the gas-liquid interface. The model can deal with both incompressible and compressible gas flows. A 2D axisymmetric geometry is considered and the model is based on a transient formulation.

II.1.1 Fluid flow equations

A single set of Navier-Stokes equations with varying fluid properties depending on the phases present locally is solved.

$$\frac{\partial \rho u_i}{\partial t} + \frac{\partial}{\partial x_j}\left(\rho u_j u_i\right) = -r\frac{\partial P}{\partial x_i} + \frac{\partial}{\partial x_i}\left[(\mu + \mu_t)\left(\frac{\partial u_i}{\partial x_j} + \frac{\partial u_j}{\partial x_i}\right)\right] + \rho g_i \qquad \textbf{Eq. 32}$$

where $r = \left\{1 + \alpha\left(\frac{\rho_l}{\rho_g} - 1\right)\right\}^{-1}$ with α the volume fraction of liquid. ρ, μ and μ_t are the density, the dynamic and turbulent viscosities respectively. P is the pressure. u_i and g_i denote the components in the i_{th} direction of the fluid velocity vector and the gravity.

The continuity equation is given by:

$$\frac{\partial \rho}{\partial t} + \frac{\partial \rho u_i}{\partial x_i} = 0 \qquad \textbf{Eq. 33}$$

II.1.2 Turbulence modelling

II.1.2.1 The standard k-ε model

The standard k-ε model is a classical RANS (Reynolds Averaged Navier Stokes) -based turbulence model, which involves the solution of two additional transport equations for the turbulent kinetic energy k and its rate of dissipation ε.

$$\frac{\partial \rho k}{\partial t} + \frac{\partial}{\partial x_i}\left(\rho u_i k\right) = \frac{\partial}{\partial x_i}\left[\left(\mu + \frac{\mu_t}{\sigma_k}\right)\frac{\partial k}{\partial x_i}\right] + \mu_t G - \rho\varepsilon \qquad \textbf{Eq. 34}$$

$$\frac{\partial \rho \varepsilon}{\partial t} + \frac{\partial}{\partial x_i}(\rho u_i \varepsilon) = \frac{\partial}{\partial x_i}\left[\left(\mu + \frac{\mu_t}{\sigma_\varepsilon}\right)\frac{\partial \varepsilon}{\partial x_i}\right] + C_{1\varepsilon}\,\mu_t G \frac{\varepsilon}{k} - C_{2\varepsilon}\,\rho \frac{\varepsilon^2}{k} \qquad \textbf{Eq. 35}$$

In **Eq. 34** and **Eq. 35**, G is the production of turbulent kinetic energy due to the mean velocity gradients. In this implementation, the Kolmogorov-Prandtl expression for the turbulent viscosity is used:

$$\mu_t = \rho C_\mu \frac{k^2}{\varepsilon} \qquad \textbf{Eq. 36}$$

σ_k, σ_ε, $C_{1\varepsilon}$, $C_{2\varepsilon}$ and C_μ are all taken to be constant and are given respectively the values of 1.0, 1.3, 1.44, 1.92 and 0.09. Note that, as explained later in this chapter, a different value of C_μ is used in the case of compressible flows.

II.1.2.2 The filtered k-ε model

This modified k-ε approach has been developed by Johansen et al. [**68**] in 2004 with the aim to partially compensate for the deficiencies of the standard k-ε model when treating time dependent flows. It utilises the same transport equations for k and ε than those given above. However, a new expression of the turbulent viscosity is introduced, based on the turbulent viscosity defined in the standard k-ε model $\mu_{t,std}$ which is corrected by a factor, as given in **Eq. 37**. The purpose of the correction factor is to reduce the effective viscosity value.

$$\mu_t = \min\left[1, C_3\,\Delta \frac{\varepsilon}{k^{3/2}}\right]\mu_{t,std} \qquad \textbf{Eq. 37}$$

C_3 is a constant whose value lies in the range [0.61; 2.3] (in PHYSICA, C_3=1 [**69**]). Δ is the filter size. Let us note that a large filter size value has no effect on the turbulent viscosity due to the "min" operator. Physically speaking, the reduction of the effective viscosity reduces the mixing of the fluid. For instance for a jet, it reduces the entrainment of the surrounding gas inside the jet. The filter size value should be chosen larger than the grid size to ensure compatibility with the filtering concept. It has therefore to satisfy the following constraint with respect to the grid resolution:

$$\Delta \geq \max\left(\Delta r_{\min}, \Delta z_{\min}, \sqrt{(\Delta r \Delta z)_{\min}}\right) \qquad \textbf{Eq. 38}$$

Where Δr and Δz are the cell length in the radial and axial dimensions respectively.

II.1.3 Differencing schemes

In the present study, we have used two different differencing schemes for the discretisation of the convective fluxes at the cell faces.

II.1.3.1 The Hybrid scheme [70]

The Hybrid scheme uses a combination of the Central Difference and the Upwind schemes. When the local value of the Peclet number, defined as the ratio of the convection forces to the diffusion forces, is in the range -2 to 2, the Hybrid scheme reduces to the Central Difference scheme. Outside this range, the flow is dominated by the convection so the Upwind scheme is used with the diffusion terms set to zero. In this way the shortcomings of the Upwind scheme are not shared by the Hybrid scheme.

II.1.3.2 The Smart scheme [71]

Smart is a third order differencing scheme which is a stabilized version of the Quick scheme. The cell face value of a variable Φ is expressed using **Eq. 39**.

$$\Phi_f = \Phi_{i+1} + 0.5\psi(r)(\Phi_{i+1} - \Phi_{i+2}) \qquad \textbf{Eq. 39}$$

where $r = \dfrac{\Phi_{i-1} - \Phi_{i+1}}{\Phi_{i+1} - \Phi_{i+2}}$ and $\psi(r) = \max[0, \min(2r, 0.75r + 0.25, 4)]$.

Φ_{i-1}, Φ_{i+1} and Φ_{i+2} are the values of the dependent variable Φ at the centre of the downwind, upwind, and "upwind upwind" cells respectively.

II.1.4 Free surface deformation model

To define and locate the moving interface between the gas and liquid phases, we have used the VOF method [**72**]. To follow the interface, this method uses scalar functions representing the volume fraction of each fluid in each computational cell. The evolution of the local volume fraction α of a given fluid is computed through the solution of the following transport equation:

$$\frac{\partial \alpha}{\partial t} + u_i \frac{\partial \alpha}{\partial x_i} = 0 \qquad \textbf{Eq. 40}$$

Fluid properties (density, viscosity) in each cell are determined by volume averaging of the properties of each phase:

$$\begin{aligned} \rho &= \alpha \rho_\ell + (1-\alpha)\rho_g \\ \mu &= \alpha \mu_\ell + (1-\alpha)\mu_g \end{aligned} \qquad \textbf{Eq. 41}$$

Surface tension effects at the free surface are accounted for when solving the Navier-Stokes equations, by adding locally an additional source term in the momentum equation [**8**].

$$\vec{F}_\sigma = \sigma J \vec{\nabla} \alpha \qquad \textbf{Eq. 42}$$

where σ is the surface tension, n is the free surface outward normal vector $\vec{n} = \dfrac{\vec{\nabla}\alpha}{|\vec{\nabla}\alpha|}$ and J the curvature $J = -\nabla \cdot \vec{n}$.

Two different numerical methods were tested to discretise the convective term in **Eq. 40**: the well-known Donor-Acceptor (DA) scheme and the Counter Diffusion Method (CDM).

II.1.4.1 Donor-Acceptor

To advect the volume fraction over the mesh, a time explicit Donor-Acceptor scheme can be used [**72**]. In this scheme, the convective flux of α across each face of interface cells is calculated by identifying (according to the direction of the local face velocity of the fluid) one cell as a donor of an amount of liquid and the neighbouring cell as the acceptor of the same amount of liquid. Moreover, it is considered that the interface within a cell is strictly parallel to one of the cell faces (**Figure 18**).

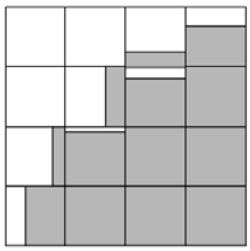

Figure 18: Interface shape as represented in the Donor-Acceptor scheme.

II.1.4.2 Counter Diffusion Method

CDM is a time implicit scheme which has been developed by Pericleous et al. [**73**] in order to avoid the use of small time steps on refined meshes inherent to explicit schemes (such as Donor-Acceptor), while preserving the interface sharpness. The implicit character of the method allows the use of larger time steps than with explicit schemes, thus reducing computational time. In this method, the convective flux of α is calculated using a "classical" first order upwind scheme, but a correction flux (counter diffusion flux) is then applied to counterbalance the numerical diffusion of the interface introduced by the upwind scheme. The idea behind counter-diffusion is to bring the numerical "bubbles" back to the gas and the numerical "droplets" back to the liquid. The counter diffusion flux is expressed by:

$$F = C\left|\vec{u}.\vec{n}\right|(1-\alpha_A)\alpha_D \qquad \textbf{Eq. 43}$$

where $\vec{u}$ and $\vec{n}$ are the fluid velocity and the normal unit vectors at the cell face centre, α_A and α_D are respectively the value of α in the acceptor and donor cells and C is a scaling factor dependent on the problem. The above equation for the flux guarantees mass conservation, as the mass taken from the 'donor' is the same as the one received by the 'acceptor'. From the results of several previous studies, the following range of values for C has been found: $1 \leq C \leq 2.5$.

II.1.5 Compressibility modelling

The original version of the PHYSICA code was developed for incompressible flow simulations. Because the present study is concerned with high speed jets in which the account of compressibility effects is important, the code was extended to handle compressible flows. Details on the modifications implemented into the code for this purpose are given in this section. Note that all the transformations to the code to account for compressibility effects and to enable the computation of compressible flows and free surface deformations within the same framework have been made by B. Lebon during a project run in parallel to the present study and are described in detail in his thesis [**74**].

II.1.5.1 Energy conservation equation

When the gas is considered as compressible, the set of equations describing the dynamics of the gas phase is supplemented by the energy conservation equation and the ideal gas law equation of state (accounting for the dependency of the density with pressure). The energy conservation equation is defined as:

$$\frac{\partial \rho h}{\partial t} + \frac{\partial}{\partial x_i}(\rho u_i h) = \frac{\partial}{\partial x_i}\left[\left(\frac{\lambda}{Cp} + \frac{\mu_t}{\sigma_T}\right)\frac{\partial h}{\partial x_i}\right] \qquad \textbf{Eq. 44}$$

Where h is the enthalpy and λ, Cp and σ_T are the thermal conductivity, the specific heat and the heat turbulent Prandtl number respectively. In the case of incompressible flows, the temperature is derived from enthalpy using **Eq. 45**, whereas in the case of compressible flows the term $\left(\frac{1}{2}U^2\right)$ is included to take into account the kinetic energy contribution leading to **Eq. 46**.

$$T = \frac{h}{Cp} \qquad \textbf{Eq. 45}$$

$$T = \frac{h - \left(\frac{1}{2}U^2\right)}{Cp} \qquad \textbf{Eq. 46}$$

II.1.5.2 Pressure correction equation

The flow equations are solved in PHYSICA using a pressure-based solver, which involves the solution of a pressure correction equation derived from the continuity equation. The general form of the pressure correction equation, including the corrections associated to the account of compressibility effects, reads:

$$a_P P'_P = \sum_i a_i P'_i + m^*_P \qquad \textbf{Eq. 47}$$

where $a_i = A_f \rho_f^* d_f + \max(k_{upw} u_{upw} A_f, 0)$, $a_P = \sum_i a_i$, A_f is the cell face area, and m_P^* the mass continuity imbalance. The subscripts *f*, P and upw denote the cell face, the cell centre and the upwind cell centre respectively and the superscripts * and ‘ denote the guess value of a variable and its correction respectively.

II.1.5.3 Modification to the turbulence model for compressible flow

When modelling a supersonic flow, the k-ε turbulence model is not accurate to reproduce the compressibility effects. Indeed, the empirical constants, especially the one used for the Kolmogorov-Prandtl expression for the turbulent viscosity (C_μ in **Eq. 36**), have been tuned for subsonic flows. Different modifications of the coefficients of the turbulent viscosity have been developed in the literature for the description of compressible flows [**75-77**]. Heinz [**75**] gives a value of C_μ as a function of the gradient Mach number as follows:

$$C_\mu = 0.07 \exp(-0.4 M_g) \qquad \textbf{Eq. 48}$$

with $M_g = \frac{|S| l}{a}$, where S is the mean shear rate, l is the turbulence length scale and a the speed of sound.

This correction was established and applied with success for a gas jet with a temperature similar to that of the surrounding gas. Yet, this model performs poorly when the temperatures of the jet and the ambient gas differ significantly. This latter situation was considered by Abdol-Hamid et al. [**76**] and Alam et al. [**77**] who took into account the variations of the turbulent viscosity at high temperatures. The work of Abdol-Hamid was concerned with a high temperature jet exiting in a low temperature ambient gas, while the work of Alam was concerned with a low temperature jet exiting in a high temperature ambient gas. Both authors have proposed a modification of the turbulent viscosity expression based on the introduction of a parameter C_T obeying the following relation:

$$C_\mu = 0.09 C_T^n \qquad \textbf{Eq. 49}$$

where C_T is:

$$C_T = 1 + \frac{C_1 T_g^m}{1 + C_2 f(M_\tau)} \qquad \textbf{Eq. 50}$$

T_g is the total temperature gradient normalised by the turbulence length scale and M_τ the turbulent Mach number:

$$T_g = \sqrt{\left(\frac{\partial T_t}{\partial x_i}\right)^2} \frac{k^{3/2}}{\varepsilon} \frac{1}{T_t} \qquad \textbf{Eq. 51}$$

$$M_\tau = \frac{\sqrt{2k}}{a} \qquad \textbf{Eq. 52}$$

$$f(M_\tau) = \left(M_\tau^2 - M_{\tau 0}^2\right) H\left(M_\tau - M_{\tau 0}\right)$$

where H(x) is the Heaviside function, $M_{\tau 0}$= 0.1 and T_t the total temperature. The values of the parameters determined in Abdol-Hamid and Alam studies are summarized in **Table 7**.

	m	C_1	C_2	n
Abdol-Hamid et al. [**76**]	3	24.33	24.33	1
Alam et al. [**77**]	0.6	1.2	1	-1

Table 7: Values of constants to calculate C_T.

Let us note that in addition to this modification Alam et al. [**77**] changed the value of the turbulent Prandtl number σ_T (from 0.9 to 0.5) as recommended by Wilcox [**78**] for free shear flows and high heat transfer problems. This value was changed to increase the heat transfer from the surroundings to the jet.

In PHYSICA, another method has been used to handle the turbulence inside a compressible jet. The value of C_μ is set to a constant value for the entire domain as a function of the ambient temperature. In his thesis, Lebon [**74**] has determined for various ambient temperatures adjusted values of C_μ listed in **Table 8** by comparing the model predictions with the experimental data reported by Sumi et al. [**79**]. An example of comparison made on the centreline velocity can be seen in **Figure 19**.

Temperature (K)	**C_μ**
285	0.07
772	0.06
1002	0.05

Table 8: Adjusted values of C_μ for different ambient temperatures with T_{jet}=190K and U_0=451 m/s [74].

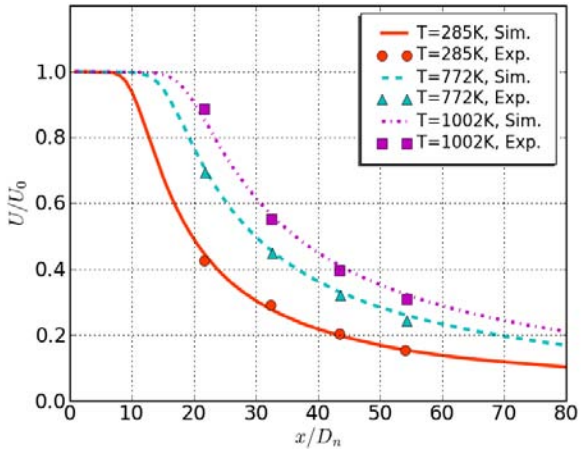

Figure 19: Comparison of the centreline velocity computed in [74] against the experimental data from Sumi et al. [79].

From the model predictions, an equation has been established to fit the adjusted values of C_μ:

$$C_\mu = A\exp\left(-B\frac{h_{amb}}{h_{jet}}\right) \qquad \textbf{Eq. 53}$$

where A =0.081, B = 0.14, h_{amb} and h_{jet} are the ambient gas and the jet enthalpy respectively.

II.1.5.4 Zonal-GALA

In the original version of PHYSICA, the solution procedure for calculating the flow field in the presence of a free surface (called the Gas And Liquid Analyser (GALA) algorithm) is based on a formulation in which the continuity equation is written in a form which conserves the volume rather than the mass. In the present study, when accounting for compressibility in the gas phase, the continuity equation in its mass conservation form (rather than in its volume conservation form) needs to be solved. To avoid any interference between the two models, a specific technique developed by B. Lebon is used [**74**]. This technique, called Zonal GALA, (**Figure 20)** consists in dividing the computational domain into two zones delimitated by the isoline of the Mach number equal to 0.3. In the region where Ma > 0.3, located near the nozzle exit, compressibility effects are fully taken into account using the mass conservation form of the continuity equation, while in the remaining part of the domain where Ma < 0.3 and which includes the gas-liquid interface, the fluids can be considered as incompressible and the continuity equation is solved in its volume conservation form. Note that the boundary between the two regions is not an input parameter, but is determined by the model as part of the solution procedure.

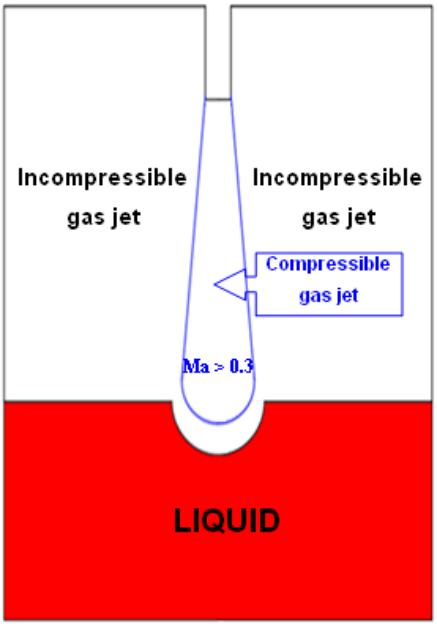

Figure 20: Principle of the Zonal-GALA approach.

II.1.6 *Boundary conditions of the model*

The computational domain is represented in **Figure 21** and the boundary conditions employed are listed in **Table 9**.

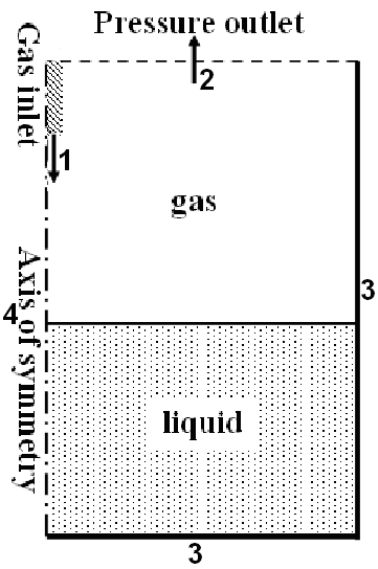

Figure 21: Computational domain.

	Type		Pressure	Velocity	k and ε	h
1	Gas inlet	Subsonic	-	U_0	k_0 and ε_0	h_0
		Supersonic	P_0			
2	Pressure outlet		0	$\frac{\partial \phi}{\partial n} = 0$		
3	Wall		-	0	Log law wall function	h_{wall}
4	Symmetry		$\frac{\partial \phi}{\partial n} = 0$			

Table 9: Boundary conditions of the hydrodynamic model.

The turbulence intensity, I, is defined as:

$$I = \frac{1}{U_0}\sqrt{\tfrac{1}{3}\left(\overline{u'^2_x} + \overline{u'^2_y} + \overline{u'^2_z}\right)} = \frac{1}{U_0}\sqrt{\frac{2k}{3}} \qquad \textbf{Eq. 54}$$

An empirical correlation to estimate I in a fully developed pipe flow (near the axis) is $I = 0.16\,\mathrm{Re}^{-1/8}$ [**78**]. Combining this correlation with **Eq. 54**, we deduce the following expression for k:

$$k_0 = \frac{3}{2}\left(0.16\,\mathrm{Re}^{-1/8}\,U_0\right)^2 \qquad \textbf{Eq. 55}$$

The turbulent dissipation rate is defined through the following empirical correlation:

$$\varepsilon_0 = C_\mu^{3/4}\,\frac{k^{3/2}}{l} \qquad \textbf{Eq. 56}$$

where the turbulent length scale is taken as $l = 0.07\,D_n$ with D_n the lance diameter and C_μ a constant (0.09 for incompressible flow).

II.2 Simulation of a free jet

The correct description of turbulence within the jet is critical for the accurate prediction of the jet spreading, and thus the size of the cavity created by the jet at the bath surface. The aim of the present section is to assess the capability of various turbulence models to describe the development of a subsonic free jet. To perform this study, we have chosen as a simulation test case the configuration and parameters used in Hussein et al. experiment [**80**]. Four variants of the k-ε turbulence model have been tested in this work: the standard and the RNG variants, as well as the modified versions of the standard k-ε model proposed respectively by Pope [**81**] and Balabel [**30**]. Note that the standard version of the k-ω turbulence model has also been tested during this study, but it was found to give poor

predictions which are not reported in the present document. All these models differ essentially in the values of the model constants used. Note, however, that in the RNG k-ε model, the transport equation of ε includes an additional source term:

$$-\frac{C_\mu \eta^3 (1-\eta/\eta_0)}{1+\beta\eta^3}\rho\frac{\varepsilon^2}{k} \qquad \textbf{Eq. 57}$$

where $\eta = \sqrt{G}\,k/\varepsilon$, $\eta_0 = 4.8$ and $\beta = 0.012$.

To better predict the spreading rate of a round jet, Balabel [**30**] proposed decreasing the $C_{1\varepsilon}$ value from 1.44 to 1.3 in the dissipation rate equation (which leads to an increased effective viscosity) while Pope [**81**] recommended increasing the $C_{1\varepsilon}$ value from 1.44 to 1.6 (which leads to a reduced effective viscosity). The standard and the RNG k-ε models were already present in the computational software PHYSICA, while the models proposed by Pope and Balabel could easily be implemented in PHYSICA by modifying the value of $C_{1\varepsilon}$. **Table 10** summarises the values of the constants for the different turbulence models considered in this study.

	C_μ	σ_k	σ_ε	$C_{1\varepsilon}$	$C_{2\varepsilon}$
Standard k-ε	0.09	1	1.314	1.44	1.92
Pope model [**81**]	0.09	1	1.314	1.6	1.92
Balabel model [**30**]	0.09	1	1.314	1.3	1.92
RNG k-ε	0.0845	0.7194	0.7194	1.42	1.68

Table 10: Values of the constants in the different turbulence models used in the present study.

The model is formulated for the steady state regime. The gas is considered to be incompressible, since the Mach number of the jet at the nozzle exit is 0.16.

II.2.1 Geometry and boundary conditions

The geometry of the computational domain taken from the work of Hussein et al. [**80**] is presented in **Figure 22**. The red lines represent the outlet boundaries, the green line is the wall of the nozzle and the blue line is the gas inlet (i.e. nozzle outlet).

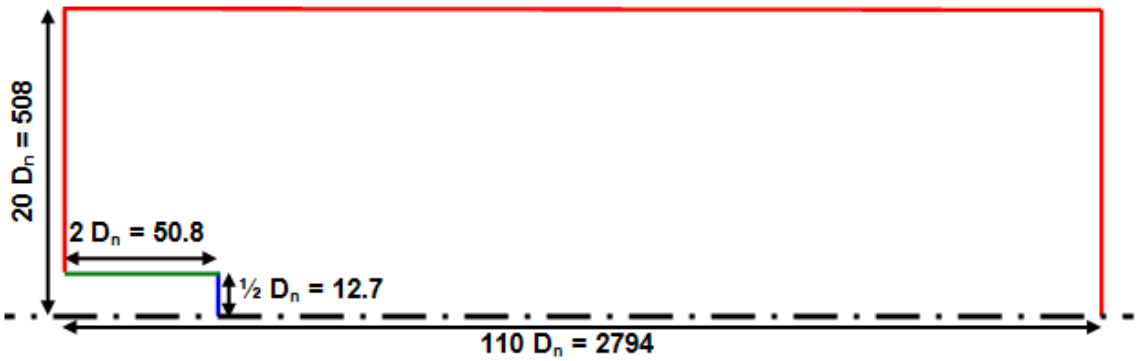

Figure 22: Geometry of the computational domain (dimensions in mm).

The mesh used in the simulations, which can be seen in **Figure 23**, contains 15370 cells. This mesh has been refined around the symmetry axis to have a better description of the centreline velocity. Note that the interior of the nozzle is not meshed.

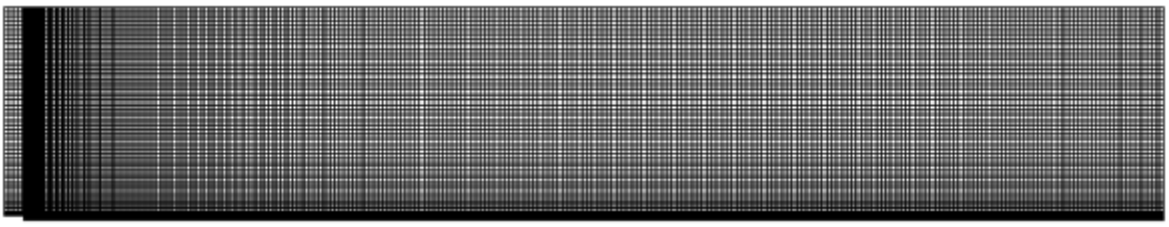

Figure 23: Mesh of the computational domain.

The simulations have been performed for a value of the jet velocity at the nozzle outlet of 56.2 m.s^{-1}, identical to that used by Hussein et al. [**80**]. The gas blowing conditions at the nozzle outlet used in our simulations are summarised in **Table 11**. k and ε are obtained from **Eq. 55** and **Eq. 56** respectively.

U_0 (m.s^{-1})	Re (10^4)	k (m^2.s^{-2})	ε (m^2.s^{-3})
56.2	9.55	0.159	5.88

Table 11: Gas blowing conditions at the nozzle outlet.

II.2.2 *Results*

In this section, the centreline velocity and the radial profile of the axial velocity calculated using four different turbulence models are compared with the experimental data of Hussein et al. [**80**]. **Figure 24** represents the variations of the jet centreline velocity over a distance of ninety times the nozzle diameter. Comparing the predictions of the standard k-ε model with those of Pope and Balabel models, one notices that an increase of the $C_{1\varepsilon}$ coefficient results in a larger value of the centreline velocity and vice-versa. This is coherent with the fact that

an increase of $C_{1\varepsilon}$ results in a greater value of ε, and thus in a reduced effective viscosity (and vice-versa). When compared to the experimental data, the Pope model overestimates the centreline velocity and the Balabel model underestimates it. The RNG k-ε model also underestimates the centreline velocity of the jet. The best performing model among the four models tested is the standard k-ε. However, even with this model, the centreline velocity is slightly under-predicted (the average error is about 6%). Data in **Figure 24** can be fitted using **Eq. 8**. The fitted values of the equation coefficients as well as the calculated length of the potential core are given in **Table 12**.

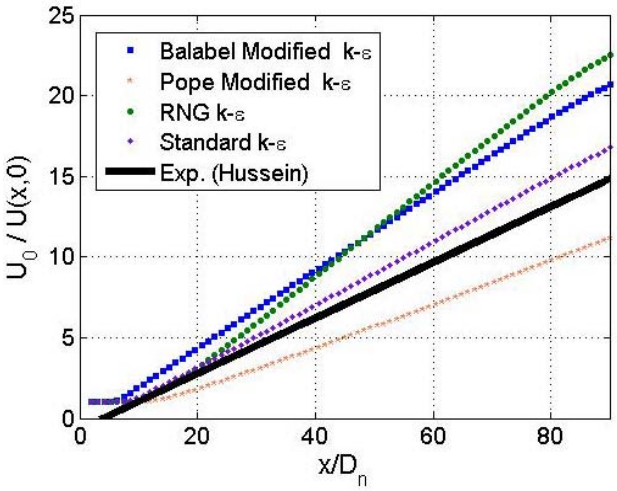

Figure 24: Centreline velocity: comparison between various simulation results and Hussein et al. experimental data fit [80].

Hussein et al. [**80**] reported experimental data for the radial profile of the axial velocity at a distance downstream the nozzle of seventy times the nozzle diameter. **Figure 25** shows the comparison between the experimental and the simulation results. All the profiles follow approximately a Gaussian distribution. The width of the jet is over-predicted by all the turbulence models except the Pope model which underestimates it. From the comparison of the results obtained with the different turbulence models, it is observed that an increase of the $C_{1\varepsilon}$ coefficient decreases the jet width and vice-versa. This is consistent with the fact that an increase of $C_{1\varepsilon}$ results, as mentioned previously, in a reduced effective viscosity (and vice-versa). A jet with a reduced effective viscosity will exhibit a low mixing rate with the ambient gas, leading to a slower spreading rate of the jet. The turbulence model closest to the experimental data is, as with the comparison in **Figure 24**, the standard k-ε. Nevertheless the half-width of the jet predicted by the standard k-ε model is overestimated by 24% (**Table 12**).

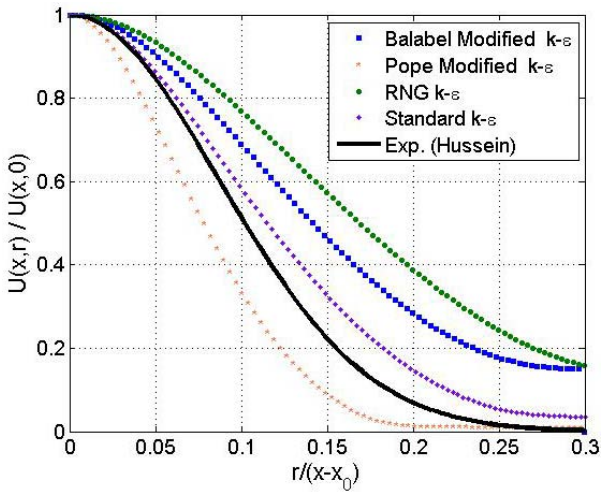

Figure 25: Radial profile of the axial velocity at 70 D_n: comparison between various simulation results and Hussein et al. experimental data fit [80].

	b	a	x_0/D_n	δ/D_n	Lp/D_n
Hussein et al. [**80**]	5.8	0.102	4	6.73	-
Balabel model [**30**]	4.22	0.141	1.47	9.69	5.3
Pope model [**81**]	7.58	0.074	6.6	4.73	11.9
RNG k-ε	3.56	0.166	8.52	10.2	9.7
Standard k-ε	5.13	0.115	3.94	7.58	7.5

Table 12: Jet characteristic parameters (Chapter I Eq. 8, Eq. 9 and Eq. 10) for the different turbulence models considered. Comparison with Hussein et al. experimental data [80].

As can be seen in **Table 12**, the turbulence model used for simulating a subsonic free jet has a significant influence on the distribution of the jet velocity and in particular on the jet spreading. None of the four models tested here is completely satisfactory. None of them is able to reproduce accurately the experimental data of Hussein et al. [**80**]. Among the four models, the standard k-ε model shows the smallest difference with Hussein et al. data. But, it predicts a jet half-width larger (by 24%) than that observed experimentally. As a consequence, it may be anticipated that the use of the standard k-ε turbulence model to simulate the impact of a gas jet onto a bath surface will produce a liquid surface cavity less deep (the jet centreline velocity being underestimated) and wider (the jet spread being overestimated) than in reality.

The over-prediction of round jets by the standard k-ε model is a well-known weakness of this model (see e.g. Wilcox [**78**]). In the present study, it was found that the simple corrections described by Pope and Balabel, which are based on the modification of the value of the

turbulence coefficient $C_{1\varepsilon}$, did not improve the model predictions. Several other corrections to the standard k-ε model have been proposed in the literature to enable more accurate predictions of round jets (see for example [**82-84**]). The performances of these other models were not evaluated in the present project and it is certainly a point that would need to be addressed in a future work.

II.3 Simulation of Qian et al. 2-phase experiment

Qian et al. [**35**] carried out experiments in a cold model to visualize the shape of the cavity when an air jet impinges the surface of a water bath. The experiments were made with a single- (water) and multi-layered (corn oil-water and kerosene-water) liquid bath. Their apparatus consisted of a square vessel containing a 29.8 cm diameter and 20.3 cm depth cylindrical glass vessel as it can be seen in **Figure 26**. The position of the interface was measured through an electro-resistive probe and the images were recorded on high-speed photographic films.

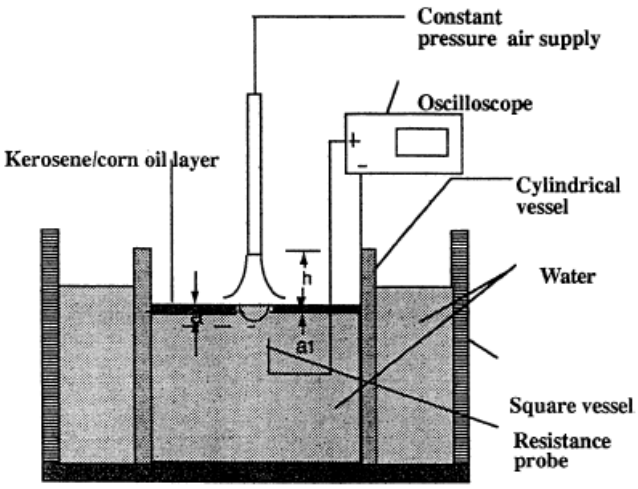

Figure 26: Experimental apparatus of Qian et al. [35**].**

The operating range of the gas flow rate was 1.43×10^{-4} to 3.57×10^{-3} m^3/s with a lance height varying from 1.5 to 21 cm. Moreover, three lances of diameters 0.25, 1.2 and 2.3 cm were used. In this section, we simulate a single-layered liquid bath experiment which was conducted with a lance diameter of 1.2 cm and a flow rate of 1.83×10^{-3} m^3/s. The simulation of experiments involving 3 phases will be presented in **Section II.4**. The geometry and conditions considered here are described in **Figure 27**.

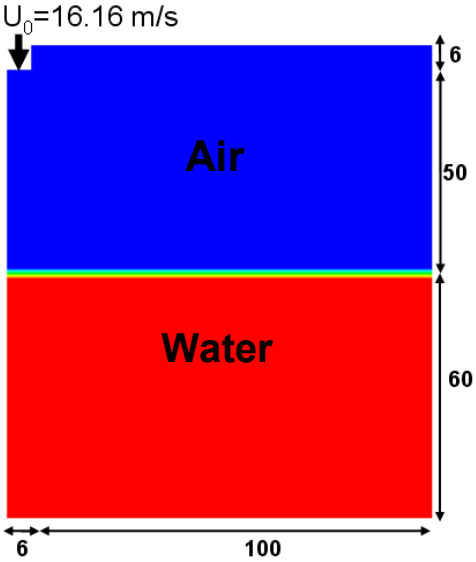

Figure 27: Geometry and initial conditions in Qian experiment (dimensions in mm).

The accuracy of the model is of dominant importance. In the following, we have tested the influence of the grid size and other models and methods to know how they affect the prediction of the cavity shape.

II.3.1 Influence of grid size

In this section, we compare the use of different meshes (refined around the interface) of various sizes. The simulation parameters are as follows:

- Four different meshes with 45x83 (2643), 53x100 (5280), 77x146 (10899) or 77x186 (14277) cells considered
- Uniform profiles of u, k and ε specified at the nozzle outlet
- Standard k-ε turbulence model
- DA for the VOF scheme
- Hybrid differencing scheme

Figure 28 represents the time-averaged computed interfaces. The refinement of the mesh slightly changes the cavity shape. When increasing the number of cells in the domain, we increase the cavity depth. The cavity depth difference is less than 1.9 mm (14%) when taking into account all the meshes and less than 1 mm (7%) when excluding the coarsest one. We can also see on the two finest meshes that the increase of the liquid initial level near the cavity is captured unlike the two coarsest ones. This is one of the reasons why the cavity is less wide for the two finest meshes. For the parametric study performed in the following

sections, a mesh consisting of 45x83 cells will be used since it leads to a computational time around ten times faster than with the finest mesh, with a difference less than 2 mm in terms of cavity depth.

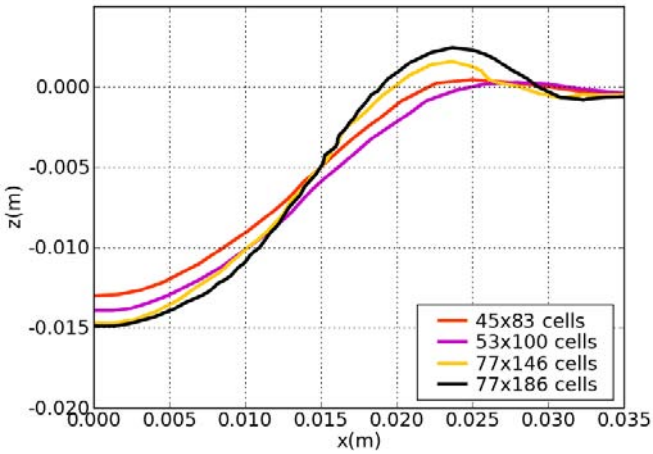

Figure 28: Time-averaged interface for different meshes.

II.3.2 Comparison of two VOF models

The simulation parameters to compare the two VOF schemes considered in this study (Donor Acceptor (DA) and the Counter Diffusion Method (CDM)) are as follows:

- Mesh of 45x83 cells
- Uniform profiles of u, k and ε specified at the nozzle outlet
- Standard k-ε turbulence model
- DA or CDM for the VOF scheme
- Hybrid differencing scheme

For both VOF schemes, **Figure 29** shows the computed time-averaged interface. Since CDM relies on an adjustable coefficient C, we tested a range of values for this coefficient. The predicted cavity dimensions were found not to be very sensitive to the coefficient value in the range 1<C<2.5. When comparing the CDM and DA solutions, it can be seen that the time-averaged results are very similar (the difference is around 0.5 mm for the cavity depth). However, the computed dynamic behaviour of the interface is markedly different (**Figure 30a** and **Figure 30b**), with the DA results producing a significant amount of interface fragmentation. The volume lost in fragmentation may explain the differences in the computed cavity dimensions. Another major difference between the two VOF schemes is the computational time. Because CDM is a time-implicit method, it is possible to use time steps about ten times greater than for the DA scheme. In these simulations, the computational time

was less than two hours for the CDM cases (Δt = 1 ms) and around twenty hours for the DA scheme (Δt = 0.1 ms).

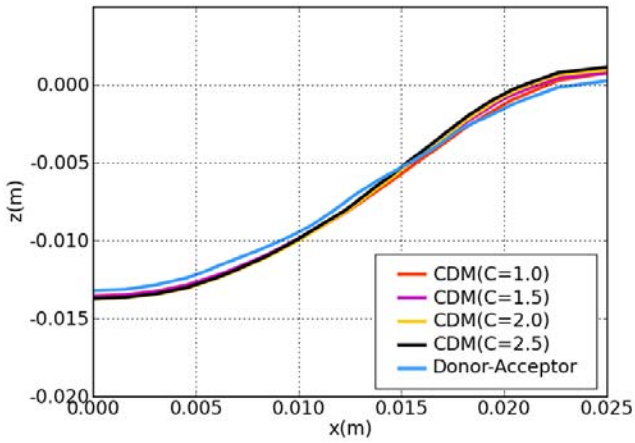

Figure 29: Time-averaged interfaces predicted using the Donor-Acceptor scheme and the Counter Diffusion Method.

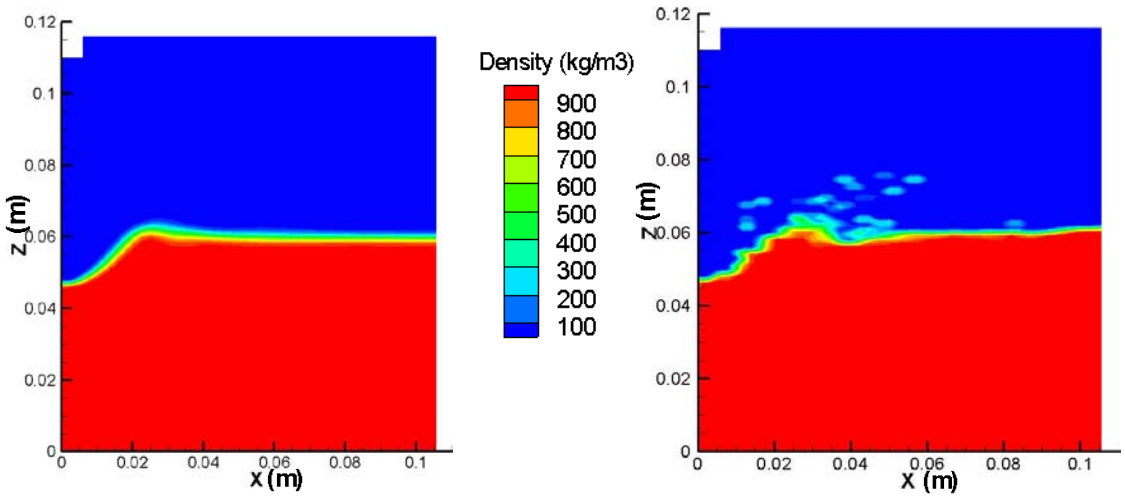

Figure 30: Instantaneous surface profile: a) CDM b) DA

II.3.3 Influence of the boundary conditions at the lance outlet

In the present section, the influence of the spatial distributions of the jet parameters (velocity, turbulent kinetic energy and its dissipation rate) at the lance outlet on the predicted cavity characteristics (i.e. depth and width) is studied. The results obtained with uniform and non-uniform distributions are compared. For the case with non-uniform profiles, it is considered that the jet exhausts from a straight lance. The lance is assumed to be long enough so that the gas flow is fully developed at the lance outlet. Using a separate model, we first simulate the gas flow in the straight lance. Then, the flow profiles computed at the lance outlet from this model are applied as inlet boundary conditions in the jet-cavity model.

II.3.3.1 Non-uniform profiles of u, k and ε at a straight lance outlet

The aim of this simulation is to determine the lance outlet profiles of the velocity, k and ε. Note that the analytical profile of the velocity of a fully developed flow in a channel is well-known in the literature [**17**] while there are no analytical profiles available for k and ε. **Figure 31** represents the 2D axisymmetric geometry of the straight lance.

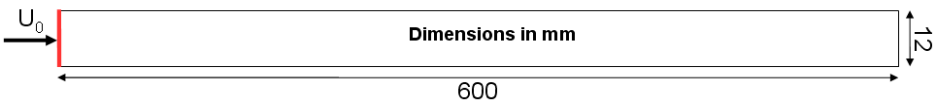

Figure 31: Geometry of the straight lance.

The simulation was made in steady state with a mesh consisting of 120x30 cells using the standard k-ε turbulence model. The flow parameters at the inlet, which are considered uniform, are:

- U_0 = 16.16 m/s (Re= $1.3.10^4$)
- k = 0.94 $m^2.s^{-2}$ (I = 4.9 %)
- ε = 178 $m^2.s^{-3}$

The axial velocity of the gas is plotted against the radial position at the lance inlet and outlet in **Figure 32**. The velocity profile computed from the analytical equation of one seventh power-law given in **Eq. 58** is also shown in this figure.

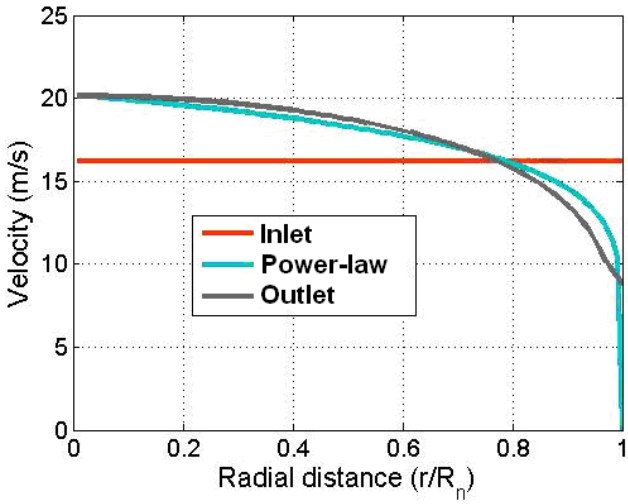

Figure 32: Axial velocity at the lance inlet and outlet.

$$\frac{u}{u_{\max}} = \left(1 - \frac{r}{R_n}\right)^{1/7} \qquad \textbf{Eq. 58}$$

where $u_{\max} = 1.25\, U_0$.

As it can be seen, the one seventh power-law equation reproduces satisfactorily the velocity profile at the lance outlet. The profile of the turbulent kinetic energy is plotted in **Figure 33** against the radial distance at the lance inlet and outlet. The outlet profile of k can be reasonably well fitted with a 3rd order polynomial as given in **Eq. 59**.

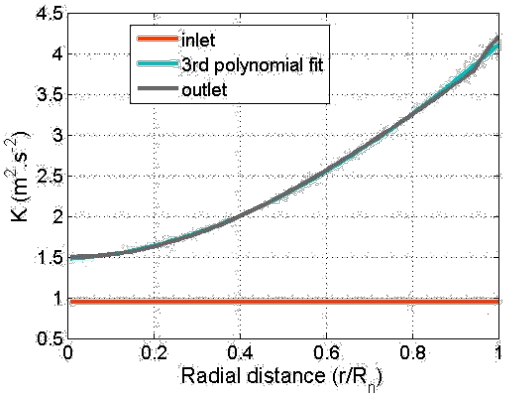

Figure 33: Turbulent kinetic energy at the lance inlet and outlet.

$$k = -2.386 \cdot 10^6 r^3 + 8.14 \cdot 10^4 r^2 + 33.97 r + 1.48 \qquad \textbf{Eq. 59}$$

As shown in **Figure 34**, the profile of ε at the lance outlet can be fitted with a 7th order polynomial as given in **Eq. 60**.

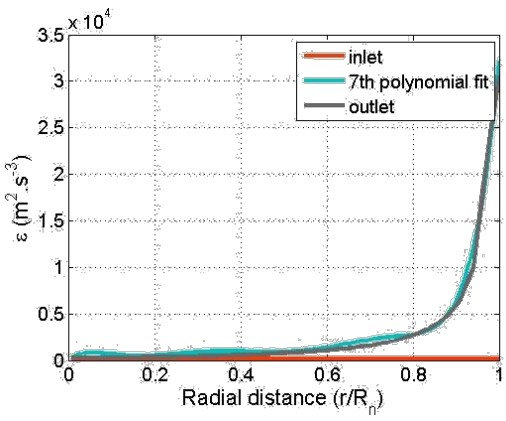

Figure 34: Dissipation rate of the turbulent kinetic energy at the lance inlet and outlet.

$$\varepsilon = 1.857 \cdot 10^{22} r^7 - 3.397 \cdot 10^{20} r^6 + 2.456 \cdot 10^{18} r^5 - 8.88 \cdot 10^{15} r^4 + 1.68 \cdot 10^{13} r^3 - 1.57 \cdot 10^{10} r^2 + 6.132 \cdot 10^6 r \qquad \textbf{Eq. 60}$$

II.3.3.2 Influence of the distributions of u, k and ε at the lance outlet on the cavity prediction

The simulation parameters to compare the influence of the distributions of the velocity, k and ε at the lance outlet are as follows:

- Mesh of 51x83 cells (More cells have been added to the jet to capture the non-uniform profiles of u, k and ε)
- Uniform or non-uniform profiles of *u*, *k* and ε specified at the nozzle outlet
- Standard k-ε turbulence model
- DA for the VOF scheme
- Hybrid differencing scheme

In this section, the above equations i.e. **Eq. 58**, **Eq. 59** and **Eq. 60** are used to specify the non-uniform profiles of U, k and ε at the lance outlet. **Figure 35** shows that the jet centreline velocity is significantly higher when considering non-uniform profiles. At the bath initial level, this velocity is equals to 13 and 17 m/s for the uniform and non-uniform profiles respectively. The cavity created by the impingement of the jet in the case of the non-uniform profiles should therefore be deeper than the cavity obtained in the case of the uniform profiles.

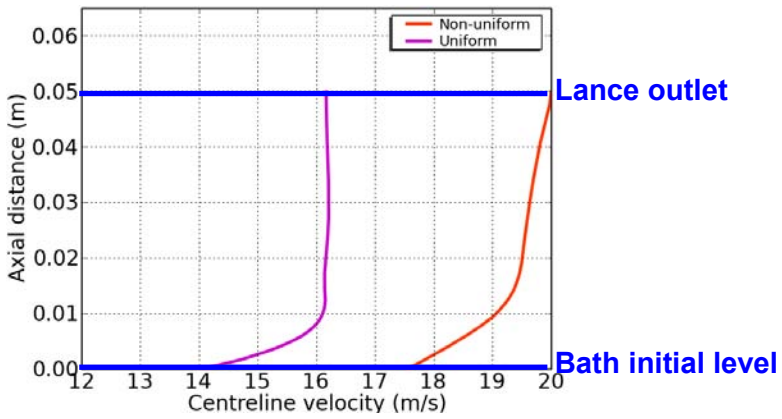

Figure 35: Centreline velocity in the gaseous phase.

This result is confirmed when comparing the time-averaged interface presented in **Figure 36** for the two cases. The cavity depth calculated with non-uniform profiles is approximately 18% higher than that with uniform profiles. The cavity width is essentially the same in both cases.

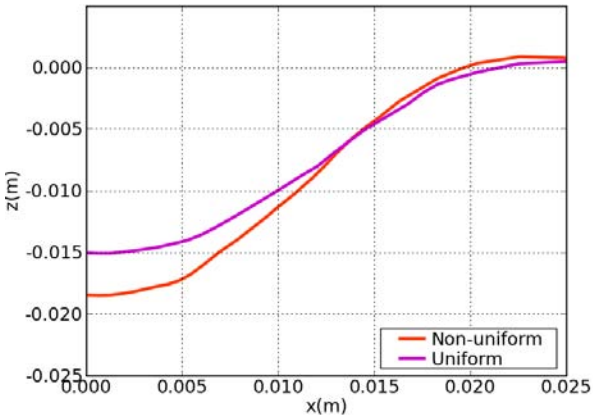

Figure 36: Time-averaged interface for different outlet profiles of u, k and ε.

II.3.4 Comparison of two different k-ε turbulence models

In this section, the performance of the standard and the filtered k-ε models is compared with the following simulations parameters:

- Mesh of 45x83 cells
- Uniform profiles of *u*, *k* and ε specified at the nozzle outlet
- Standard or filtered (three different filter sizes) k-ε turbulence model
- CDM for the VOF scheme
- Hybrid differencing scheme

The time-averaged interfaces of the cavity predicted for the different cases are shown in **Figure 37**.

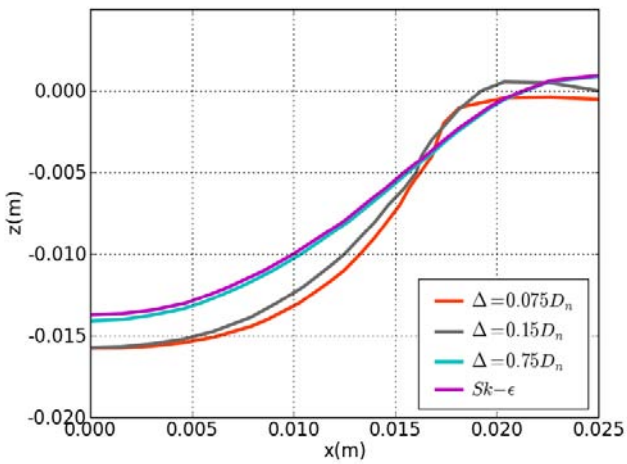

Figure 37: Time-averaged interface predicted using the standard and the filtered k-ε model.

Overall, the results obtained with the two different turbulence models in terms of shape and dimensions of the cavity are relatively similar. The results are all within ± 15%. It is observed that the jet penetration increases when the filter size decreases. Indeed, a decrease of the filter size reduces the turbulent viscosity, so the jet centreline velocity increases and therefore the cavity depth increases. Note that when the filter size becomes very large, the cavity obtained is the same as with the standard k-ε turbulence model because the filter has no effect.

II.3.5 Comparison of two different differencing schemes

Two different differencing schemes of the convective terms are compared: the third order Smart and Hybrid schemes. The simulations parameters are as follows:

- Mesh of 45x83 cells
- Uniform profiles of u, k and ε specified at the nozzle outlet
- Standard k-ε turbulence model
- CDM for the VOF scheme
- Hybrid or Smart differencing scheme

From **Figure 38**, it can be seen that the depths of the cavity predicted using the two schemes are of the same order of magnitude. The prediction using the Hybrid scheme is slightly deeper (by 5%). The width of the cavity is almost identical for the two schemes. The computational time of the run using Smart is 23% higher than the run using Hybrid. This is due to the fact that Smart is a higher order differencing scheme than Hybrid.

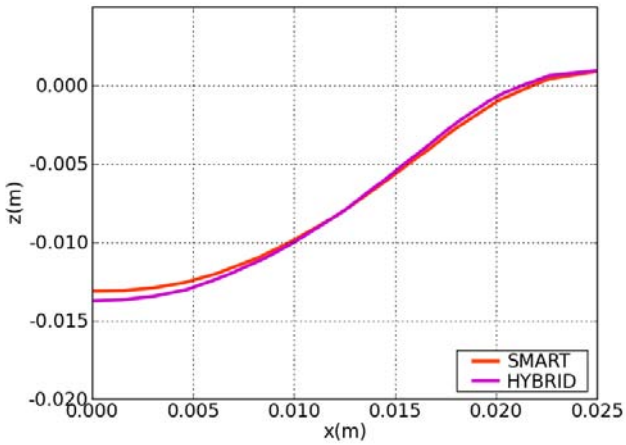

Figure 38: Time-averaged interface for two differencing schemes.

II.3.6 Optimal input and model validation

As presented above, different simulations have been performed to investigate separately the influence of various models and input data on the prediction of the cavity dimensions. In this section, the model predictions for different combinations of these input data are compared against the measurements performed by Qian et al. [**35**]. The parameters of the 10 cases simulated are displayed in **Table 13** and the simulation results are compared with the experimental data in **Figure 39**. One should note that the experimental data given by Qian et al. [**35**] are provided with a standard deviation of 0.5 mm (3 % of the cavity depth).

	Turbulence model		Mesh			VOF		Profiles of U, k and ε		Differencing scheme		Depth of the cavity (10^{-3} m)	Area of the cavity (10^{-3} m^2)	Volume of the cavity (10^{-6} m^3)
	standard k-ε	filtered k-ε	45 x 83 cells	51x 83 cells	91x83 cells	DA	CDM	uniform	non-uniform	HYBRID	SMART			
A	■		■			■		■		■		13.01	1.21	7.91
B	■		■				■	■		■		13.73	1.31	8.38
C		■	■				■	■		■		16.14	1.56	9.1
D	■		■				■	■			■	13.1	1.27	8.52
E	■			■		■		■		■		15.06	1.4	8
F	■			■		■			■	■		18.46	1.78	8.57
G		■		■			■		■	■		22.02	2.31	10
H	■			■			■		■	■		18.58	1.85	9.24
I	■				■		■		■		■	18.82	1.86	8.72
J	■				■	■			■		■	18.97	1.84	8.1
	QIAN ET AL. EXPERIMENTAL RESULTS											15.55	1.25	5

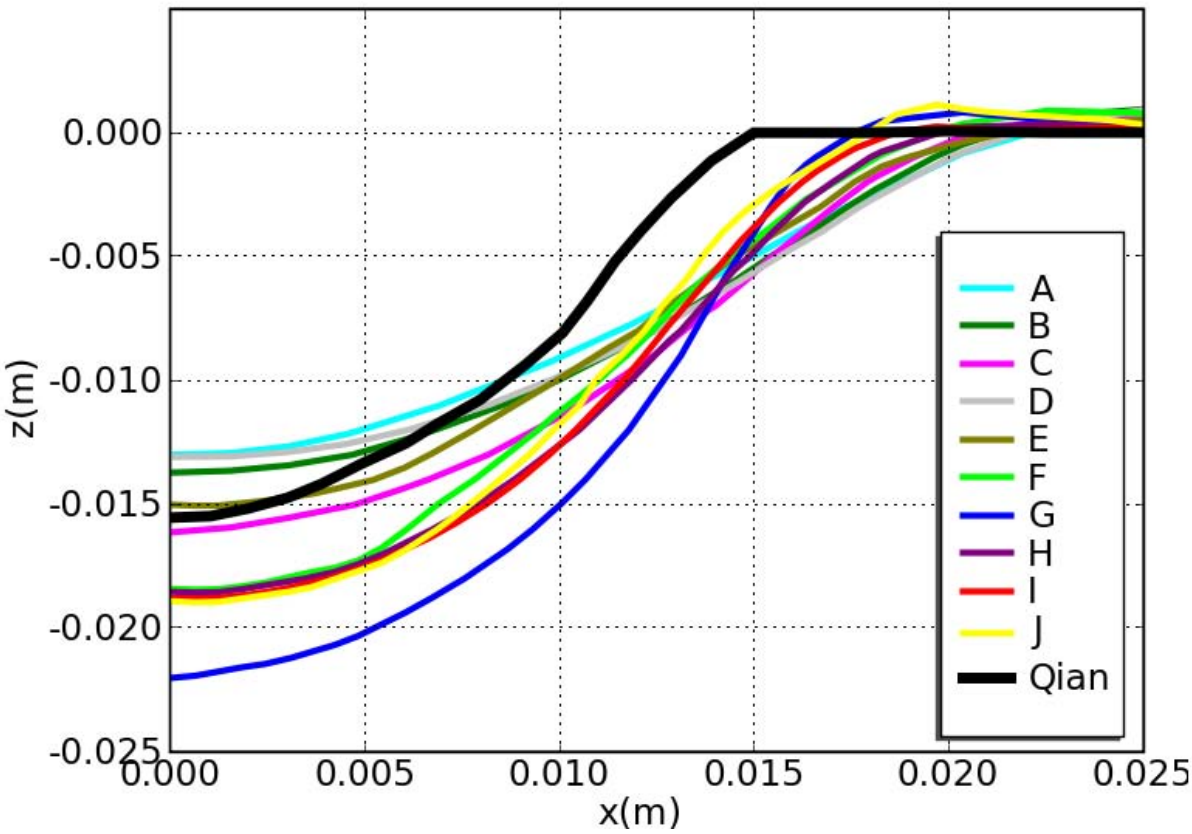

Figure 39: Time-averaged interface of the cavity for the 10 cases.

The depth of the cavity is either under- (cases A, B, D and E) or over-(cases C, F, G, H, I and J) predicted by the model, while the width is always over-predicted. The area and the volume of the cavity are systematically over-predicted by the model (except for the area in case A). Case E gives the best results (discrepancy of 3% for the depth, 11% for the area and 60% for the volume) among all the cases. This case combines the following models and parameters: a 51x83 cells mesh, standard k-ε turbulence model, Donor-Acceptor or Counter Diffusion Method scheme, uniform profiles for the velocity, k and ε at the lance outlet, Hybrid

differencing scheme. Note that the case E (which only differs from case F by the type of profiles of u, k and ε) leads to better results than case F, despite the fact that the non-uniform profiles are expected to be a more physically realistic representation of the jet outlet parameters than the uniform profiles. The parameters and models used in case E will be referred in the following as the optimal input parameters of the model and will be retained for all the simulations presented in the remaining of the manuscript. It is important to note that these optimal input parameters may include some compensating errors, since all possible combinations of parameters have not been tested.

It seems clear that the difficulties in reproducing accurately the surface cavity are for a large part related to the deficiencies of the k-ε turbulence model which, as illustrated previously, overestimates the spreading of the jet. In order to get better model predictions, it would be helpful in the future to resolve this turbulence modelling issue. It is also important to note that the effects of the 3D especially the rotation of the cavity around the symmetry axis can also be part of the discrepancy between our model and the experiment.

II.4 Simulation of the IJL jet-cavity experiment

II.4.1 Experiments made at IJL

The experiment developed at Institut Jean Lamour (IJL), which can be seen in **Figure 40,** aims at visualizing the impingement of a free gas jet onto a deformable surface. The facility consists of an interior cylindrical water bath of diameter 450 mm within a square vessel also filled with water for mechanical support and diffraction issues. The jet is created by blowing compressed air through a vertical lance with a 0.635 mm exit diameter nozzle. In this apparatus, the lance can be inclined at various angles from the horizontal water surface. Experiments are recorded using a high-speed camera. The recorded images are then processed in order to determine the profile of the cavity resulting from the jet impact. In addition to the cavity created by the gas jet, the observation of splashing and the measurement of the amount of water ejected have been also studied. However, this latter point will not be discussed here. The present experimental study was performed by an undergraduate student from the University of Alberta during a 6 month internship [**85**].

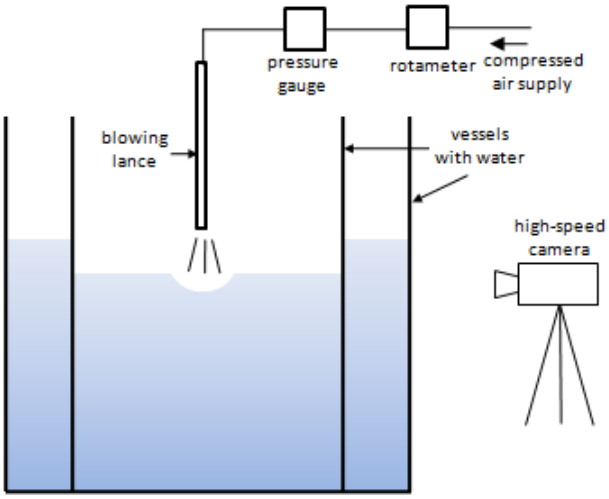

Figure 40: Experiment developed at IJL.

II.4.2 Results

II.4.2.1 *Example of experimental results*

Several experiments were conducted at 4 gas flow rates (1.58, 2.98, 4.08, and 4.97x10^5 m^3/s) and 5 lance heights (10, 20, 31, 62, and 91 mm). The cavity depths experimentally obtained have been reported in **Figure 41**. As it could be expected, the cavity depth increases with an increase of the flowrate or with a decrease of the lance height.

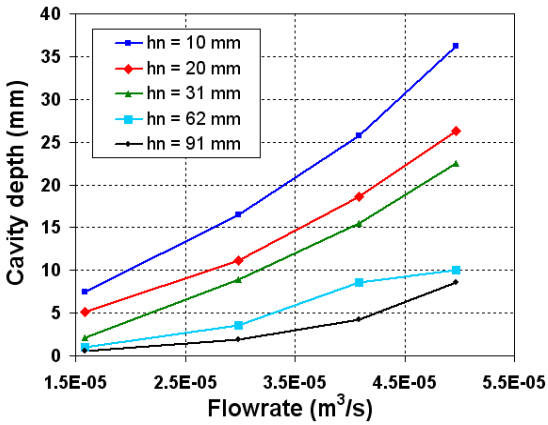

Figure 41: Cavity depth as a function of the flowrate for different lance heights.

II.4.2.2 *Simulation results*

The experiment which has been simulated here was conducted for a gas flow rate of 2.98x10^{-5} m^3/s and a lance 20 mm above the initial level of the bath. The "best performing" set of parameters determined in the previous section (coarse mesh, standard k-ε, uniform profiles for u, k and ε at the lance outlet and Hybrid and DA schemes) is applied to simulate the experiment. The coarse mesh, consisting of 66x63 cells, is shown in **Figure 42** where the

red line is the initial liquid level. A refinement of the mesh has been done near the lance outlet.

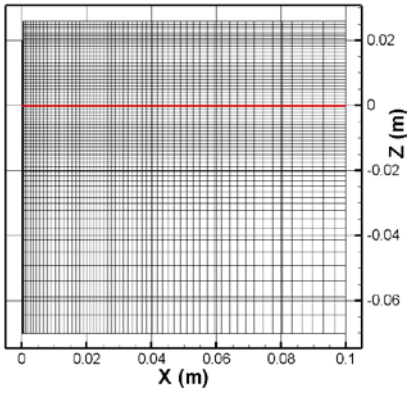

Figure 42: Mesh (66x63 cells) of the IJL model, red line is the initial liquid level.

The velocity distribution in the gas phase is depicted in **Figure 43**. The proximity of the lance to the bath surface prevents the gas to go outside the jet region after its impingement. All the gas is re-entrained inside the jet after escaping the cavity.

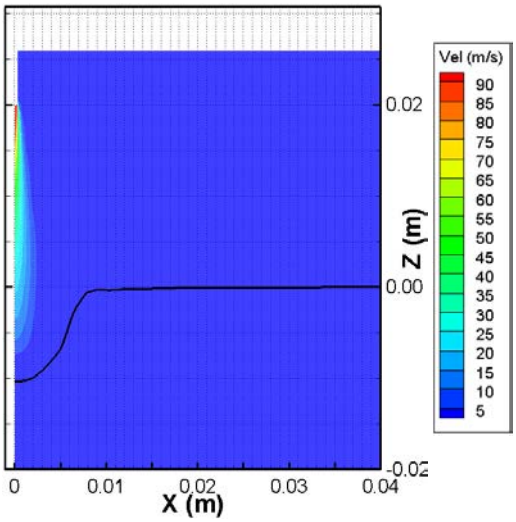

Figure 43: Time-averaged distribution of the velocity magnitude in the gas phase.

The time-averaged profiles of the interface between air and water measured in the experiment and predicted by the model are compared in **Figure 44**. Similarly to the simulation of the experiment of Qian et al. presented in the previous section, the cavity depth is well reproduced (with a 1 mm precision). However, the width of the cavity is greater (around 16%) in our simulation compared to the experiment.

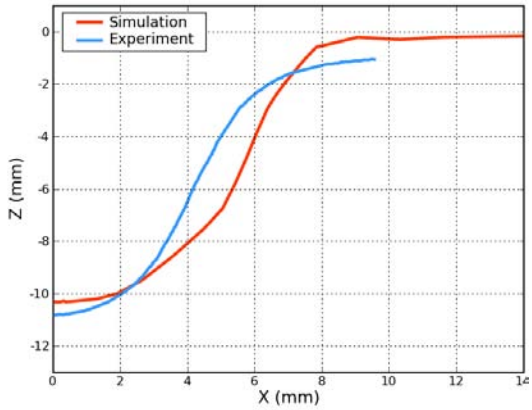

Figure 44: Time-averaged interface of the cavity in the IJL model.

II.5 Simulation of Qian et al. 3-phase experiment

The model of the steelmaking converter should deal with three phases, i.e. the molten steel, the liquid slag and the gaseous phase. In this section, a third phase representing a lighter liquid layer on top of the liquid bath is taken into consideration. The results obtained with this new model are compared against the experimental measurements performed by Qian et al. [**35**] for a two layer liquid bath configuration.

II.5.1 Three-phase handling

To deal with three types of interface (gas-liquid1, gas-liquid2 and liquid1-liquid2), the VOF model two marker functions (α and β) is introduced. The marker α is treated by means of the Counter Diffusion Method while the marker β is treated using the Donor-Acceptor scheme. Two different methods for the VOF have been used since it is impossible to treat the two markers with CDM in the current version of Physica. The two marker functions satisfy the following conditions:

- $\alpha = 0$ when the cell does not contain liquid2
- $\alpha = 1$ when the cell does not contain gas
- $\beta = 0$ when the cell does not contain liquid1
- $\beta = 1$ when the cell is full of liquid1

Using these two functions, fluid properties (density, viscosity) in each cell are defined as.

$$\phi = \beta\,\phi_{liquid1} + (1-\beta)\alpha\,\phi_{liquid2} + (1-\beta)(1-\alpha)\phi_{gas} \qquad \textbf{Eq. 61}$$

II.5.2 Experiment and boundary conditions

Simulations have been performed for two different systems (air-kerosene-water and air-corn oil-water) based on the experimental work from Qian et al. [**35**] to which the simulation results are compared. The gas blowing conditions and the properties (density and viscosity) of the various liquids considered are summarized in **Table 14**. Two different liquids (of viscosity 1.5 and 46 times the water viscosity respectively) have been used as a lighter liquid layer on top of the bath. Two different lance outlet flow conditions are considered for each system: respectively conditions A and B for the air-corn oil-water system and conditions C and D for the air-kerosene-water system. The mesh used in the simulations, which can be seen in **Figure 45**, contains 45x71 cells. This mesh has been refined around the interfaces to have a better description of the interface deformations. The thickness of the second liquid layer is set to 8 mm. Note that all the simulations presented here have been performed using the optimal input parameters of the model derived in the previous section (cf. **Section II.3.6**). Since the current version of PHYSICA can deal with surface tension forces at only one interface, only the surface tension associated to the interface between air and liquid2 (corn oil or kerosene) has been taken into account. It would be necessary in future simulations to extend the code to take into consideration the surface tension at each of the various interfaces i.e. gas-liquid2, gas-liquid1 and liquid1-liquid2.

Liquid	$\sigma_{liquid/air}$ (N/m)	ν_{liquid} ($m^2.s^{-1}$)	ρ_{liquid} ($kg.m^{-3}$)	Ref.	U_0 (m/s)	k ($m^2.s^{-2}$)	ε ($m^2.s^{-3}$)
Corn oil	0.0341	$4.6.10^{-5}$	860	**A**	4.42	0.129	9.04
				B	7.12	0.29	31.6
Kerosene	0.025	$1.5.10^{-6}$	810	**C**	6.38	0.104	6.56
				D	7.61	0.14	10.42
Water	0.0728	10^{-6}	1000				

Table 14: Properties of the liquids and gas blowing conditions at the nozzle outlet (3-phase model).

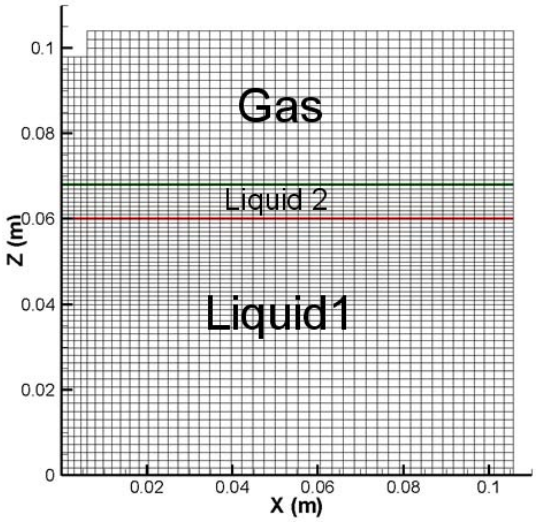

Figure 45: Mesh of the computational domain and initial regions occupied by the three phases.

II.5.3 Kerosene as the second liquid

Figure 46 and **Figure 47** show the numerical and experimental results in the case of kerosene for outlet gas velocities of 6.38 and 7.61 m/s respectively. It can be seen from the figures that naturally the higher the velocity, the deeper the cavity. It may be also noted that the kerosene-water remains little affected when the velocity is 6.38 m/s. This is due to the fact that the shear exerted by kerosene on water is not significant. One can see in **Figure 46** that the experiment and the simulation give very close results. The water-kerosene interface is perfectly predicted by the model while the air-kerosene interface is predicted with a precision less than 1 mm. Note that, at higher gas velocity (7.61 m/s), the numerical results are less accurate (precision less than 3 mm).

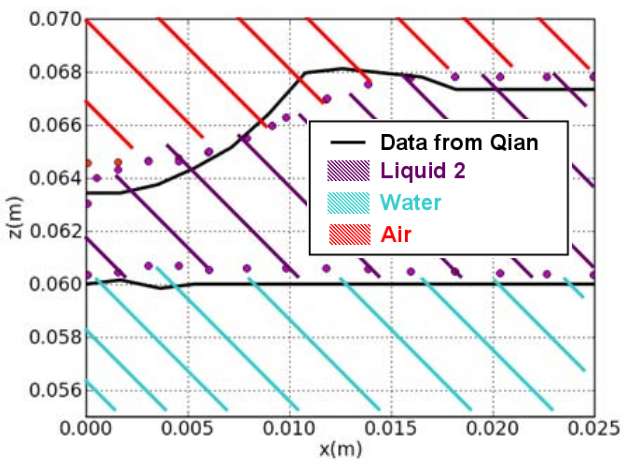

Figure 46: Time-averaged interfaces for air-kerosene-water (U_0=6.38 m/s).

In **Figure 47**, we can notice that, according to the model, the water is lifted up next to the nozzle axis and is in contact with the air jet. This phenomenon may be attributed to the kerosene flow induced by the action of the gas jet, which in turn induces some motion of the water in the bath. This lift-up phenomenon is not observed in the experiment. This discrepancy could be partly related to the fact that the model does not take into account the surface tension at the water/kerosene interface.

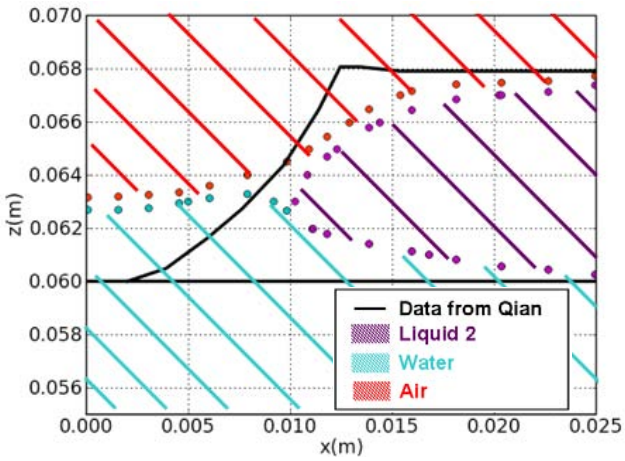

Figure 47: Time-averaged interfaces for air-kerosene-water (U_0=7.61 m/s). The "white regions" (non-hatched parts) represent regions where the three different phases are present.

II.5.4 Corn oil as the second liquid

As shown in **Figure 48 and Figure 49**, the time-averaged interfaces calculated with corn oil used as the covering liquid layer are in relative good agreement (precision less than 2 mm) with those obtained experimentally for both velocities. At low velocity, the water is lifted up by around 2 mm near the jet axis compared to its initial level. The water is raised more than in the case of kerosene due to the higher viscosity of corn oil. Indeed, the high viscosity of corn oil enhances the transmission of the shear to the corn oil/water interface.

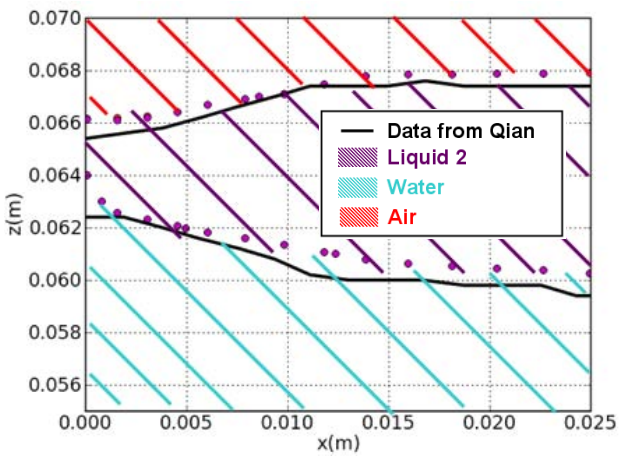

Figure 48: Time-averaged interfaces for air-corn oil-water (U_0=4.42 m/s).

When increasing the jet velocity from 4.42 m/s to 7.12 m/s, more water is lifted-up and the water layer is now in contact with the air in the impingement region (**Figure 49**), with the corn oil pushed laterally away. This behaviour may be attributed to the fact that the higher the velocity, the higher the shear transmitted to the corn-oil/water interface. The influence of the viscosity of the upper liquid layer is well-represented here. As it was shown, in the case of a kerosene layer (i.e. low viscosity), the transmission of the shear from the gas jet to the water interface is less than in the case of a corn oil layer (i.e. high viscosity).

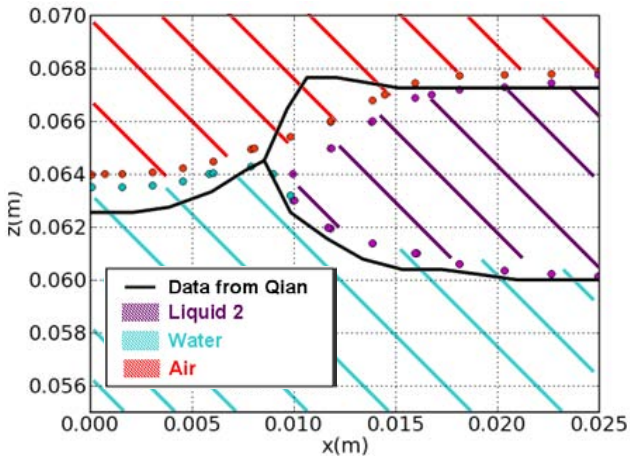

Figure 49: Time-averaged interfaces for air-corn oil-water (U_0=7.12 m/s). The "white regions" (non-hatched parts) represent regions where the three different phases are present.

II.6 Simulation of a supersonic oxygen jet impacting a liquid steel bath

The model is used in this section to simulate the deformation of a liquid steel bath under the impact of a supersonic oxygen jet in a pilot-scale converter, which was located, until recently, at ArcelorMittal Maizières. Similar calculations carried out for the case of 355 tons industrial converter are presented in **Appendix B**. The pilot represented in **Figure 50** is 3.8 m high with an inner diameter of 1.4 m. The liquid steel bath is 0.5 m deep, which represents a mass of metal of around 5 tons. A vertically oriented lance located 1 m above the bath supplies the oxygen. The physical properties of the oxygen and liquid steel are listed in **Table 15**.

	ρ (kg/m^3)	μ (Pa.s^{-1})	λ (W.m^{-1}.K^{-1})	Cp (J.kg^{-1}.K^{-1})	σ (N/m)
Oxygen	Ideal gas law	1.9.10^{-5}	0.025	1024	-
Liquid steel (at 1650°C)	6940	0.5.10^{-2}	40	611	1.54

Table 15: Physical properties of the oxygen and liquid steel used in the simulations.

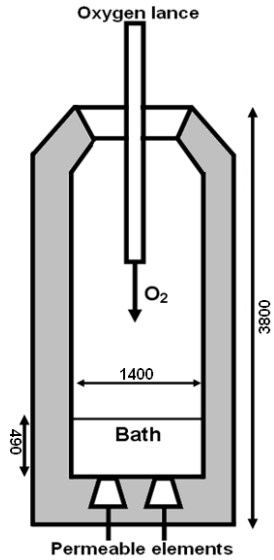

Figure 50: **Schematic representation of the pilot-scale converter (dimensions in mm).**

The pilot furnace has been simulated under the following conditions:

- Oxygen at the nozzle outlet: velocity of 378 m/s (corresponding to a Mach number of 1.39), temperature of 203 K, density of 1.92 kg/m^3
- Ambient gas temperature equal to 300 K, wall furnace temperature equal to 1273 K and lance wall temperature equal to 323 K
- Nozzle diameter: 22 mm

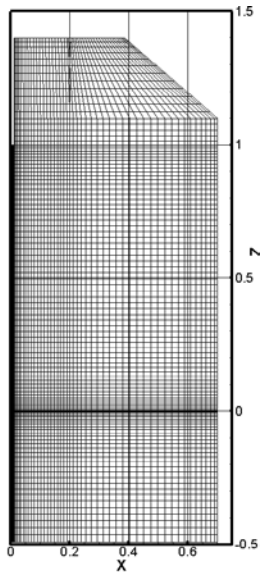

Figure 51: Mesh (51x107 cells) of the pilot-scale converter.

The simulations parameters are as follows:

- Mesh: 51x107 cells (**Figure 51**)
- Uniform profiles of u, k and ε specified at the nozzle outlet

- Modified standard k-ε turbulence model with C_μ as defined in **Eq. 53**
- CDM for the VOF scheme
- Hybrid differencing scheme
- Zonal GALA with a criterion of Ma = 0.3

Figure 52 shows the transient evolution of the velocity distribution when the liquid metal is impinged by the supersonic oxygen jet. As we can see on these figures, the jet hits the liquid surface and goes up next to the wall after sweeping the liquid surface. A part of the flow is entrained inside the jet while the rest of it leaves the converter. The flow structure is composed of a single recirculation loop created by the entrainment of the surrounding gas inside the jet. The velocity distribution inside the gaseous phase reaches very quickly (after approximately 2 s) a quasi-steady state regime. The jet is strongly decelerated downstream the nozzle exit, and the oxygen velocity near the bath surface in the impinging region is of the order of 10 m/s, which corresponds to a low subsonic (incompressible) regime. **Figure 52** indicates that the induced motion of liquid steel in the bath is weak, with a maximum velocity of 0.05 m/s. The streamlines inside the bath reveals the motion of the liquid metal. As we can see, it takes more time for the flow inside the bath to be steady (around 21 s). The recirculation loop centre created at the edge of the cavity at the beginning of the process, moves along the free surface to the wall of the vessel. This loop centre is then definitely located at the same radius that the loop centre inside the gaseous phase (0.5 m).

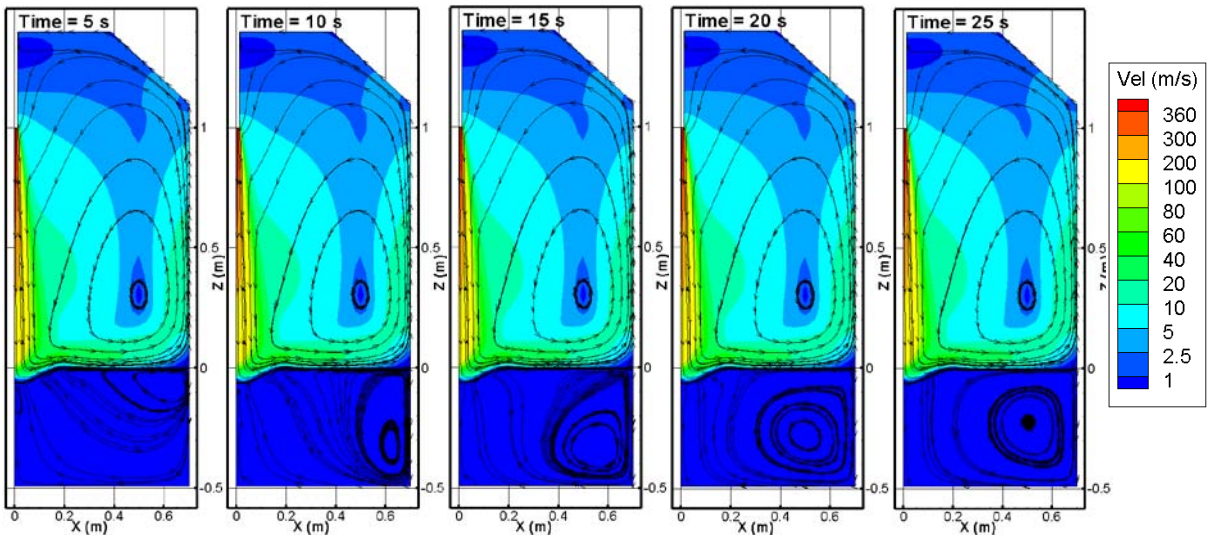

Figure 52: Streamlines and velocity distributions in the pilot-scale converter (U_0=378 m/s) at five different time instants.

The time-averaged distribution of the density is plotted in **Figure 53** where the gas and the liquid are represented by the blue and the red regions respectively. The black line represents the boundary which separates the inner region of the jet where compressible effects need to be accounted for (Mach number greater than 0.3) and the outer region where compressibility is negligible (Mach number smaller than 0.3) and the gas may be treated as incompressible. The location of this boundary is computed by the model and is the basis of the zonal-GALA approach employed in the present calculations. It can be observed that for the present conditions, the compressible region is sufficiently far away from the bath surface to avoid any interference between the compressible model and the flow calculations in the free surface region.

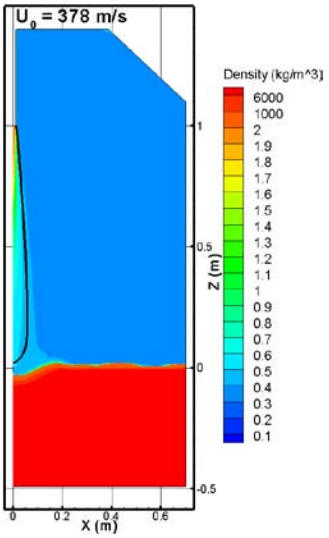

Figure 53: Time-averaged density distribution in the pilot-scale converter (U_0=378 m/s). The black curve represents the isoline of the Mach number relative to a value of 0.3.

The interface between the gas and the liquid is depicted in **Figure 54** where we can see that this interface is slightly fluctuating with time. The time-averaged dimensions of the cavity created by the oxygen jet are 60 mm for its depth and 182 mm for its width.

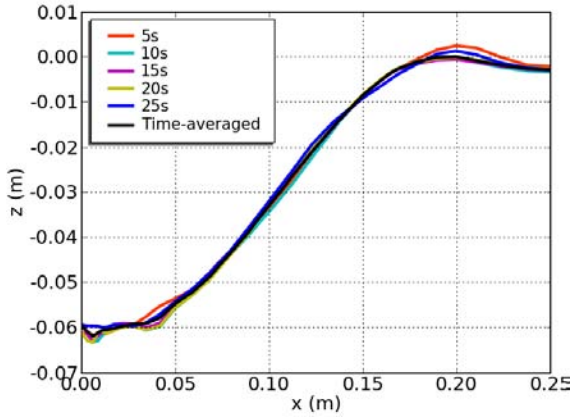

Figure 54: Pilot-scale converter simulation (U_0=378 m/s): interface profile at different time instants.

It is important to note that the value of the C_μ coefficient has an important effect on the centreline velocity and therefore on the cavity depth. A comparison of the results obtained using the standard value of C_μ recommend for incompressible flow (i.e. 0.09) and those computed using the corrected value of C_μ for compressible flow (i.e. 0.069 using **Eq. 53**) has been plotted in **Figure 55**. As we can see, the decrease of the C_μ coefficient increases significantly (by about 25 %) the cavity depth. Indeed the smaller the C_μ coefficient, the less the surrounding entrainment and the less the centreline velocity decrement. Thus, a proper prediction of the surface cavity requires a careful determination of the C_μ coefficient. It would be highly desirable to have the corrected values used in the present study confirmed by further verifications against a wider set of experimental data. It would be also helpful for the simulation of the steelmaking converter to determine corrected values of C_μ for ambient temperatures greater than 1000 K.

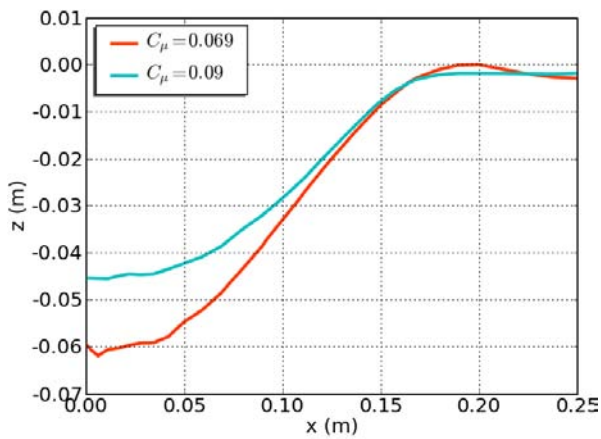

Figure 55: Pilot-scale converter simulation (U_0=378 m/s): interface profile for different C_μ values.

An investigation has been made on the effect of the jet velocity at the nozzle outlet on the cavity size. The adjusted values of the C_μ coefficient for the different outlet velocities considered are listed in **Table 16**.

U_0 (m/s)	C_μ
378	0.069
500	0.0712
750	0.0742

Table 16: Adjusted values of C_μ for different inlet velocities with T_{jet}=203 K and T_{amb}=300 K.

Figure 56 shows the time-averaged density distribution for the different velocities investigated. The size of the compressible region (marked by the black curve in **Figure 56**) obviously increases with the jet outlet velocity. In the same trend, we can also see that the

cavity dimensions increase with the velocity (see also **Figure 57**). It is interesting to observe the evolution of the thickness of the interface (orange colour in **Figure 57**). The present results suggest that as the velocity is increased, a foaming process occurs at the interface (mixing of the gas and the liquid phases), which results in a thicker interface.

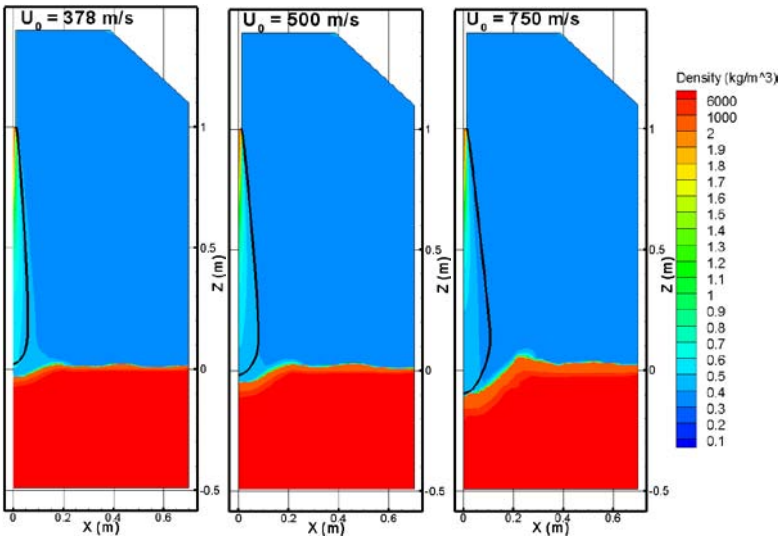

Figure 56: Time-averaged density distribution in the pilot-scale converter for different velocities. The black curve represents the isoline of the Mach number relative to a value of 0.3.

In **Figure 57**, the time-averaged interfaces for the different jet outlet velocities are depicted. Even if the cavity depth increases with the velocity, we can notice that the cavity width remains between 200 and 300 mm whatever the velocity. Besides, we can see the different cavity deformation modes reported by Molloy [**27**]. It starts with a shallow cavity at 378 m/s and evolves towards a deep cavity at 750 m/s.

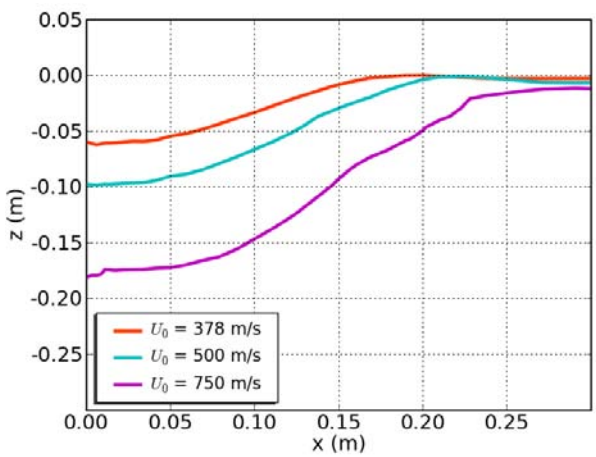

Figure 57: Pilot-scale converter simulation: interface profile for different velocities.

The predicted depth of the cavity has been plotted as a function of the inlet velocity in **Figure 58**. The data may be fitted using a linear regression model equation (**Eq. 62**). They have been compared using the Koria et al. [**32**] (see **Table 4**) correlation for a supersonic jet impinges a free surface. The model developed is quite accurate on the cavity depth when comparing to the Koria experimentally obtained equation for the maximum cavity depth. This difference between our calculated depth and the maximum one reported increases when increasing the inlet velocity from 7% to 16%. When increasing the velocity, we increase the mixing between the gas and the liquid leading to a greater maximum depth and a cavity more difficult to be captured. This can be one reason of the increase of this difference.

Let note that the equation used to fit our curve has been established for the 6t pilot-scale converter with the lance height at 1 m and should be used carefully in any other case.

$$h_{cav}(mm) = -0.00032\,U_0 + 0.06 \qquad \textbf{Eq. 62}$$

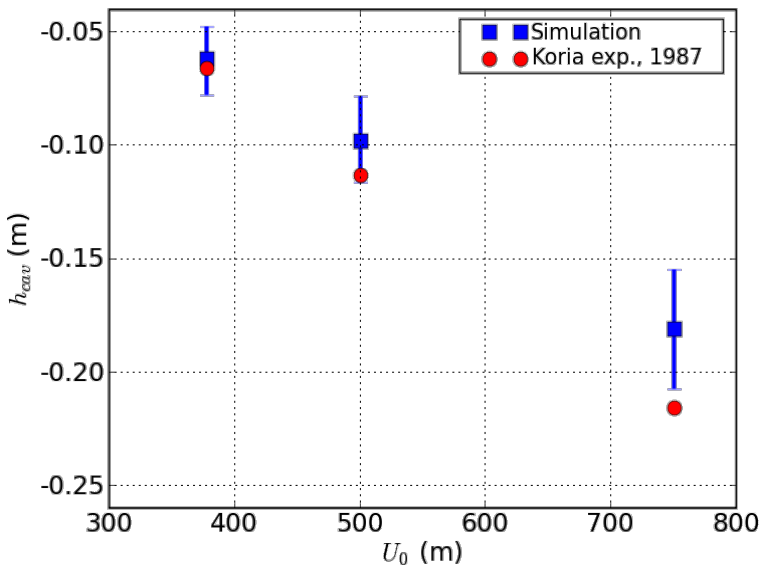

Figure 58: Cavity depth as a function of the inlet velocity.

II.7 Conclusions

This chapter was about the numerical modelling of the impingement of a jet onto a liquid surface. The model presented takes into account fluid flow, energy transport, and turbulence phenomena and the dynamic behaviour of the liquid free surface. The model includes gas compressibility effects. After a description of the equations used, the model was tested on a cold model experiment and a pilot-scale converter.

First, an evaluation of the performance of four variants of the k-ε turbulence model for the

description of the behaviour of a free subsonic jet has been presented. The simulation results were compared to experimental data reported by Hussein et al. [**80**]. None of them was able to reproduce perfectly the measured velocity profiles of the jet. Among the models tested, the standard k-ε model shows the smallest discrepancy with the experimental data, but the half width of the jet is overestimated by 24%. Regarding the calculation of the deformation of the bath free surface, the influence of different VOF schemes, k-ε turbulence models, differencing schemes and boundary conditions at the lance outlet on the computed bath surface cavity has been examined. When comparing the two different VOF methods (DA and CDM) or the two different differencing scheme (Smart and Hybrid), it was found that the cavity dimensions remain of the same order of magnitude. A relatively coarse mesh was found to be sufficient to prevent any significant influence of the mesh size on the model results. At the lance outlet, the specification of non-uniform profiles of the jet parameters leads to a deeper cavity than when using uniform profiles. The filtered k-ε model produces slightly deeper cavity than the standard k-ε. Several combinations of parameters have been tested and the results of these tests have been compared against experimental data obtained in the present work and by Qian et al. [**35**] for the case of a subsonic jet. The best agreement, yet not completely satisfactory, was found when combining uniform profiles of u, k and ε at the nozzle outlet, the DA and Hybrid schemes and the standard k-ε turbulence model. Some results obtained for a 3-phase system were also presented, which show a relative good agreement with measurements made by Qian. Finally, the model has been used to simulate the impact of a supersonic oxygen jet onto a liquid metal surface. The cavity depth for different inlet velocities has been compared to the equation experimentally obtained by Koria et al. [**32**]. The cavity depth is reasonably well reproduced.

Chapter III Post-combustion numerical model

III.1 Mathematical model

Post-combustion is the reaction in the gaseous phase between the oxygen from the lance and the CO from the decarburisation process. As indicated before, this reaction is highly exothermic and the resulting heat is to be transferred to be bath. It is then of paramount importance to model the process to know the parameters affecting the post-combustion and the heat created.

The real combustion phenomena consist of many intermediate reactions. The modelling of the combustion does not need to take into account all the intermediate reactions since we are only interested in the masses of the species at the end of the combustion. Moreover, this simplification helps decrease the resolution time of the combustion. The model used is the Simple Chemical Reaction Scheme where a small number of equations is used to find the solution.

The Simple Chemical Reaction Scheme (SCRS) was developed by Spalding [**86**]. With this model, the kinetically controlled method is used, which assumes that the oxidant and the fuel can coexist in an element for a certain time due to turbulence.

The model has been tested on three configurations of various scales and compared to the experimentally obtained data.

III.1.1 Main assumptions

The main assumptions used for the simulations of post-combustion are as follows:

- The bath surface is assumed to be steady
- The geometry is axisymmetric
- As a first approximation, slag can be neglected
- The gas density obeys the ideal gas law and is composition dependent

Moreover, it is assumed that as the oxygen enters the bath, the ensuing reactions produce CO as the only gas resulting from the decarburisation process. The only reaction occurring in the gaseous part is:

$$CO + 1/2\ O_2 \rightarrow CO_2 \qquad \textbf{Eq. 63}$$

So the gases considered in our study are CO as fuel, O_2 as oxidant and CO_2 as product.

III.1.2 Governing equations

III.1.2.1 Transport equations

The conservation equation of a quantity ϕ may be expressed as:

$$\frac{\partial \rho\phi}{\partial t} + \frac{\partial}{\partial x_i}(\rho u_i \phi) = \frac{\partial}{\partial x_i}\left[\Gamma_\phi \frac{\partial \phi}{\partial x_i}\right] + R_\phi \qquad \textbf{Eq. 64}$$

The different source and diffusion terms for the quantities in the case of the post-combustion model can be seen in **Table 17**.

	ϕ	Γ_ϕ	R_ϕ
Continuity	1	0	0
Momentum	u_j	$\mu_+\mu_t$	$-\frac{\partial P}{\partial x_j} + \rho g_j$
Kinetic turbulent energy	K	$\mu + \frac{\mu_t}{\sigma_k}$	$\mu_t G - \rho\varepsilon$
Dissipation rate of the kinetic turbulent energy	ε	$\mu + \frac{\mu_t}{\sigma_\varepsilon}$	$C_{1\varepsilon}\,\mu_t G \frac{\varepsilon}{k} - C_{2\varepsilon}\,\rho \frac{\varepsilon^2}{k}$
Mass fraction of remaining fuel	m_{CO}	Γ	R_{CO}
Mixture fraction	f	Γ	0
Enthalpy	h	$\frac{\lambda}{Cp} + \frac{\mu_t}{\sigma_T}$	$a(R-E) + div\left(\lambda h\, grad\left(1/Cp\right)\right)$

Table 17: Source and diffusion terms of the system of equations.

Note that the model includes compressibility effects due to pressure variations.

First of all, consider the transport equation of the reacting species (i.e. CO and O_2)

$$\frac{\partial}{\partial t}(\rho\, m_i) + div\left(m_i\, \rho u - \Gamma_i\, grad\ m_i\right) = R_i \qquad \textbf{Eq. 65}$$

With the sum of the mass fraction $\sum m_i = 1$.

If we introduce a variable $\phi = st \cdot m_{CO} - m_{O2}$ were $st = \frac{1/2\, W_{ox}}{W_{fu}} = \frac{16}{28} = 0.571$ is the stoichiometric ratio of the reaction, then

$$\frac{\partial}{\partial t}(\rho\phi) + div\left(\phi\rho u - \Gamma_{\phi} grad\ \phi\right) = st \cdot R_{CO} - R_{O2} = 0 \qquad \textbf{Eq. 66}$$

Without any source term, ϕ becomes a passive scalar.

Like in the VOF, the same approach is used and a mixture fraction variable is introduced and defined as $\phi = f.\phi_{CO} + (1- f)\phi_{O2}$ where ϕ_{CO} and ϕ_{O2} denote the inlet of CO and O_2 respectively.

Hence $f = \frac{\phi - \phi_{O2}}{\phi_{CO} - \phi_{O2}}$ so $f = \frac{(st \cdot m_{CO} - m_{o2}) - (st \cdot m_{CO} - m_{O2})_{O2}}{(st \cdot m_{CO} - m_{O2})_{CO} - (st \cdot m_{CO} - m_{O2})_{O2}}$ and $\boxed{f = \frac{st \cdot m_{CO} - m_{O2} + 1}{st + 1}}$

The enthalpy is chosen as the conserved variable when using the SCRS and it is related to the temperature by **Eq. 67**.

$$h = CpT + m_{CO}H_{react} + \tfrac{1}{2}U^2 \qquad \textbf{Eq. 67}$$

The term $\left(\tfrac{1}{2}U^2\right)$ is included only if the flow regime is supersonic. The heat of the reaction H_{react} = -10.1 MJ/kg [**87**].

And the chemical reaction is:

$$1\text{kg CO} + st\ \text{kg } O_2 \leftrightarrow (1+st)\ \text{kg } CO_2 \qquad \textbf{Eq. 68}$$

Or by dividing by 1+st,

$$f_{st}\ \text{kg CO} + (1-f_{st})\ \text{kg } O_2 \rightarrow 1\ \text{kg } CO_2 \qquad \textbf{Eq. 69}$$

Where f_{st} is the stoichiometric mixture fraction $f_{st} = \frac{1}{1+st} = 0.636$.

The dissipation rate of CO is calculated using the Eddy Break-up (EBU) [**88**] model which assumes that the limiting factor in the sink of fuel is driven by the turbulent mixing of the species.

$$R_{CO,EBU} = -C_{EBU}\rho \min\left[m_{CO}, \frac{m_{O2}}{st}\right]\frac{\varepsilon}{k} \qquad \textbf{Eq. 70}$$

where C_{EBU} is the EBU constant, m_{CO} and m_{O2} the mass fractions of CO and O_2 respectively.

The radiation plays an important role in the heat transfer occurring in an absorbing, scattering and emitting medium. Many different radiation models solve the radiation fluxes along a determined direction. This is not applicable when the mesh is not structured. On an unstructured mesh, one method is the composite radiosity equation (**Eq. 69**). The radiosity being the average of the incoming and outgoing radiation fluxes integrated over all directions.

$$div\left[\frac{4}{3(a+s)}grad\,R\right]+a(E-R)=0 \qquad \textbf{Eq. 71}$$

The term in the enthalpy transport equation a(R-E) is used when the radiation model is activated with E, the black body emissive power $E=\sigma T^4$. a, R and σ are the absorption coefficient, the radiosity and the Stefan-Boltzmann constant respectively.

Additional sources or sinks may be associated with different boundaries of the domain. These are used to implement the necessary boundary conditions and may be different from case to case.

III.1.2.2 Derived parameters

From the enthalpy, the temperature is derived following **Eq. 72**.

$$T=\frac{h-m_{CO}H_{react}-\left(\frac{1}{2}U^2\right)}{Cp} \qquad \textbf{Eq. 72}$$

The masses of the oxidant and the product are derived from the mass of fuel and the mixture fraction (**Eq. 73** and **Eq. 74**).

$$m_{O2}=st\left[m_{CO}-\frac{f-f_{st}}{1-f_{st}}\right] \qquad \textbf{Eq. 73}$$

$$m_{CO2}=1-m_{O2}-m_{CO} \qquad \textbf{Eq. 74}$$

The density is computed from the ideal gas law: $\rho=\frac{pW}{rT}$ with $\frac{1}{W}=\frac{m_{CO}}{W_{CO}}+\frac{m_{O2}}{W_{O2}}+\frac{m_{CO2}}{W_{CO2}}$.

Where W_i is the molecular weight of the specie i and r the gas constant (r=8.314 $J.K^{-1}.mol^{-1}$).

III.1.2.3 Penetration of the oxygen in the bath

In the industrial process, the oxygen reacts with the species in the bath. The model needs to take into account these reactions by simulating the penetration of the oxygen into the bath. Since the only equations of species transport solved are the ones of fuel and mixture fraction, we need to modify their source terms to represent the loss of oxygen from the top space, in addition to the required mass sink. The modification of the source term has been applied to the cells of the gaseous phase at the cavity surface. **Eq. 75** denotes the modification applied to the source term of the continuity equation.

$$\Delta R_{mass}=-\frac{1}{V_i}\dot{m}_{O_2}Coef\,m_{O_2,i}\,A_i \qquad \textbf{Eq. 75}$$

Where $\dot{m}_{O_2}$, A_i and V_i are the mass flux density of the oxygen entering the bath, the area and the volume of the present cell respectively. Coef is calculated over the "gaseous cells" at the cavity surface as:

$$Coef = \frac{\sum_j A_j}{\sum_j A_j \, m_{O_2,j}} \qquad \textbf{Eq. 76}$$

The Coef term prevents the take-up of more mass than the mass of oxygen available in the "gaseous cells" at the interface between the gas and the liquid bath. The mixture fraction and the CO transport equation are updated as a function of the mass taken. When this mass is a mixture of O_2, CO and CO_2, the masses of CO and CO_2 are pushed back in the domain.

III.1.3 Boundary conditions

The computational domain is represented in **Figure 59** and the boundary conditions employed are listed in **Table 18**. Sometimes, at the outlet, referred here as boundary condition 2, some "extern" gas enter in the vessel. In the simulation, the gas entered in the vessel is assumed to be the product i.e. CO_2.

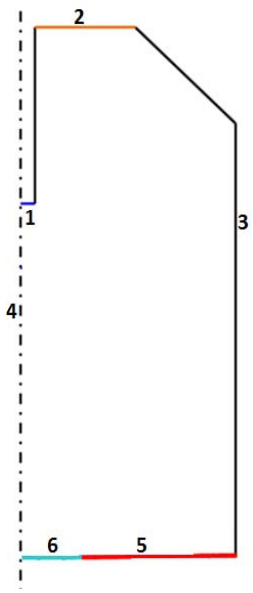

Figure 59: Boundary conditions of the post-combustion model.

	Type	Density	Velocity	k and ε	h	m_{CO}	f
1	Supersonic O_2 inlet	ρ_0	U_0	k_0 and ε_0	h_0	0	0
2	Pressure outlet	0	$\frac{\partial \phi}{\partial n} = 0$			-	-
3	Wall	-	0	Log law wall function	h_{wall}	-	-
4	Symmetry	$\frac{\partial \phi}{\partial n} = 0$					
5	CO inlet	ρ_{CO}	U_{CO}	k_{CO} and ε_{CO}	h_{co}	1	1
6	O_2 outlet	-	0	Log law wall function	h_{bath}	-	-

Table 18: Boundary conditions of the post-combustion model.

III.2 Numerical results

III.2.1 Nippon Steel Corp. Case

III.2.1.1 Experiment and boundary conditions

Nippon Steel Corp. has performed an experiment [**89**] in a cylindrical reacting tube (**Figure 60**) to better understand the post-combustion occurring in the gaseous part of the steelmaking converter.

The oxygen and the CO inlets are from 4 mm and 10 mm diameter lances located at the top and at the bottom of the tube respectively. The gas outlet is an annular section located 5 mm from the right-top of the domain in the simulation while in the experiment, it is a 125 mm diameter pipe.

The operating parameters are:

- U_{O2} = 29.15 m/s
- U_{CO} = 14 m/s
- T_{O2}= T_{CO} = 300 K
- The walls are considered adiabatic in the simulation

The mesh used in our PHYSICA model is depicted in **Figure 61**.

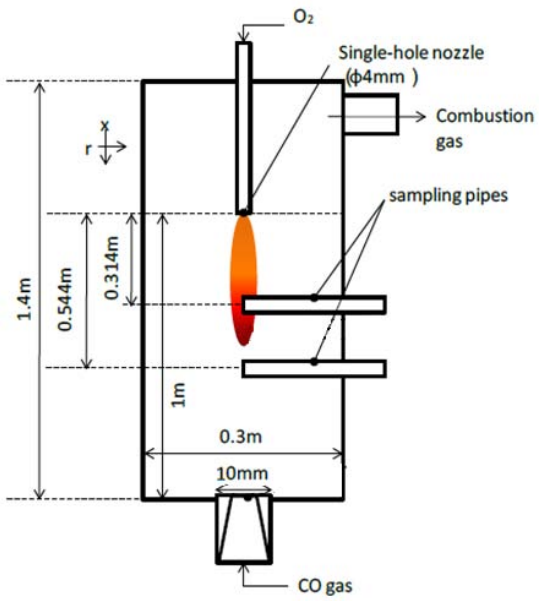

Figure 60: Schematic representation of the NSC reacting tube apparatus [89].

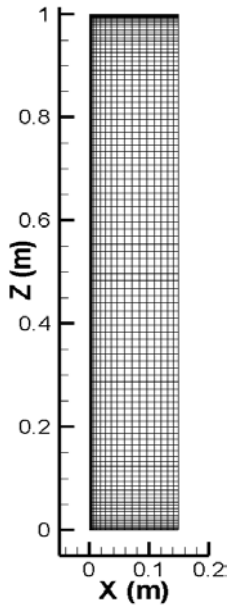

Figure 61: Mesh of the NSC case (20x104 cells).

One should note that compressibility effects are not into the picture in these simulations since the jets are purely subsonic.

III.2.1.2 ***Results***

Since in PHYSICA we used the mass fraction of the species, they need to be converted to mole fraction for comparison against the experimental data reported by NSC. This conversion has been done through **Eq. 77**.

$$n_i = m_i \frac{W}{W_i} \qquad \textbf{Eq. 77}$$

where n_i, is the mole fraction of the species i.

The computed velocity and temperature distributions in the reacting tube have been plotted in **Figure 62**. We can see from the velocity profile that the bulk of the domain is quite stagnant with velocity lower than 2 m/s. The jet entrances are the two spots where the velocity is the highest. These jets drive the motion of the fluid in this reacting tube. The temperatures are in the same order of magnitude inside the tube except at the jet entrances where the gas remains cold and around the oxygen jet where the substantial part of the reaction takes place. Indeed, due to the Kelvin-Helmholtz vortices, the CO is entrained inside the oxygen jet surrounding and reacts with it. Therefore we have an increase of the temperature enhanced by the formation of CO_2. One should also note that at the middle of the domain the temperature is at its maximum value. This is coherent with the variations of

the species mole fraction at the centreline where we can see that the product is high (above 0.75) in the region of maximum temperature (**Figure 66**).

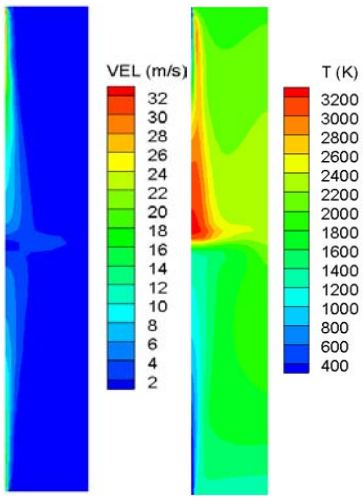

Figure 62: Velocity and temperature distributions in the reacting tube.

Figure 63 depicts the species mole fraction for the fuel, the oxidant and the product. The regions rich of fuel and oxidant are at their entrances. The oxygen entering the reacting tube reacts with the CO at the edge of its jet. This can be confirmed with the **Figure 63c** where the region rich of product is located at the oxygen jet boundary.

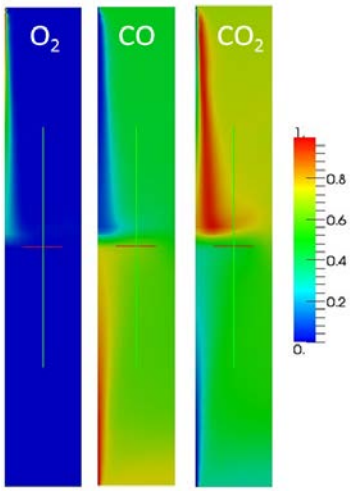

Figure 63: Distributions of the mole fractions of the species.

The mole fractions of the species in sections located at 0.314 m and 0.544 m from the lance tip have been plotted against experimental data in **Figure 64** and **Figure 65** respectively. The experimental data are shown on a continuous line in the figures.

At 0.314 m from the oxygen entrance, the line-graphs follow the same tendency and are less accurate in the jet region (0 < r < 20 mm). Inside the oxygen jet region, our simulation

predicts more oxygen and less product than in the experimental case. The fuel is relatively the same and found to be low inside this oxygen jet region. This discrepancy may be due to the use of the incompressibility in the entire domain. Indeed, Kaizawa et al. [**89**] shows the influence of the compressibility effects on this case. Adding for compressibility allows the core jet to be higher and to mix less with the surrounding. Another explanation could be related to the use the standard k-ε which overestimates the spreading of the jet. Outside the oxygen jet, the precision is better when going away from the symmetry axis (from 0.2 % to less than 0.06 % of mole fraction). This is concomitant with the fact that the jet expansion is not well reproduced.

At 0.544 m, the simulation model reproduces the experimental data with an average precision 10% and the tendencies are the same before the crossing-over point located near the wall of the reacting tube. The crossing-over appears when there is more product than fuel. In experiment case, it appears near to the tube wall. In our model, the crossing-over point is not visible.

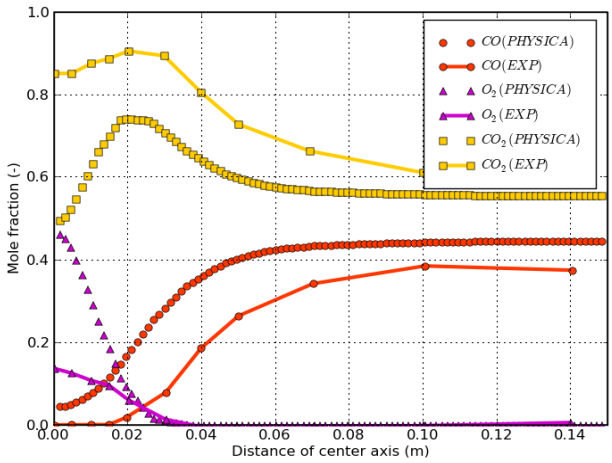

Figure 64: Species mole fraction at 0.314 m from the O_2 lance tip.

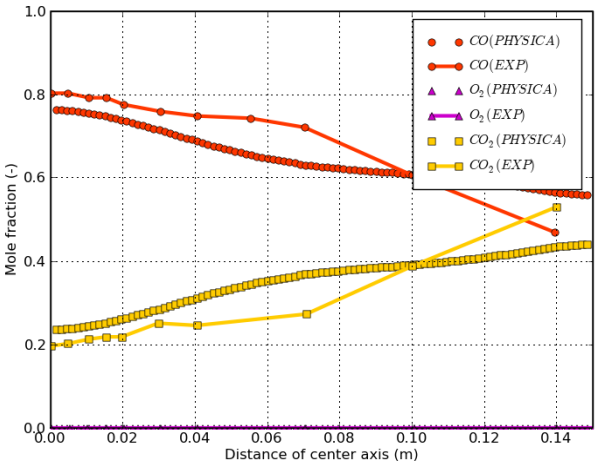

Figure 65: Species mole fraction at 0.544 m from the O_2 lance tip.

The species mole fraction at the centreline is plotted in **Figure 66**. The previous remarks can be better seen in the centreline species mole fraction. In fact, the simulation does not match the experiment before x=0.5 m: the oxygen and the CO_2 mole fractions are over- and under-estimated respectively by the model. As aforementioned this may be due to the oxygen jet expansion. It is also important to note that in the present simulation, the rate of the reaction has been modelled using the Eddy Break-Up model which assumes that the reaction is driven by the turbulence. Since here, the flow is not entirely turbulent, the use of this model is questionable and may contribute to the observed discrepancies. After 0.5m from the oxygen

inlet, the model is in good agreement with the experimental data. The precision of our model varies from 0.3 (30%) to 0.025 (2.5%) when going away from the oxygen entrance.

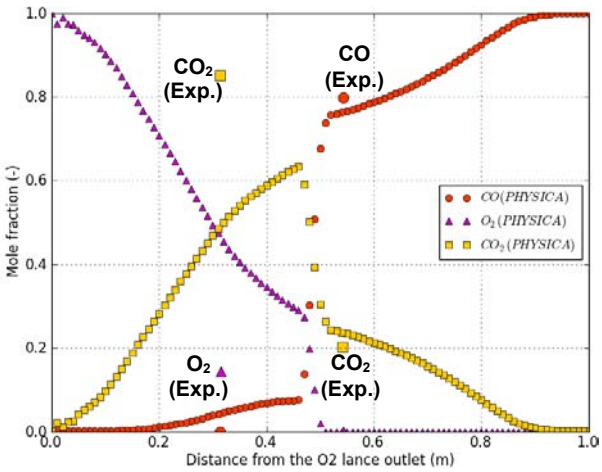

Figure 66: Species centreline mole fraction.

III.2.2 6t pilot case

III.2.2.1 Experiment and boundary conditions

ArcelorMittal Maizières has carried out experiments on a 6t pilot to study the post-combustion mechanisms. Those experiments included a gas analysis (O_2, CO, CO_2, Ar and N_2) and a temperature measurement inside the pilot. The diameters of the nozzle and vessel were 22 mm and 1.4 m respectively.

The computational geometry is considered to be axisymmetric and is displayed in **Figure 67**.The outlet is located at the top of the domain and the bath located at the bottom of the domain is divided into two parts, the first part under the jet impingement zone is where the O_2 can get into the bath, whereas the second one, further from the axis, is where the CO can get out of the bath. These two zones occupy two sevenths and five sevenths of the radius for the O_2 region and CO region respectively. The division has been chosen from previous VOF runs showing that the cavity width is around 200 mm for different lance heights and velocities.

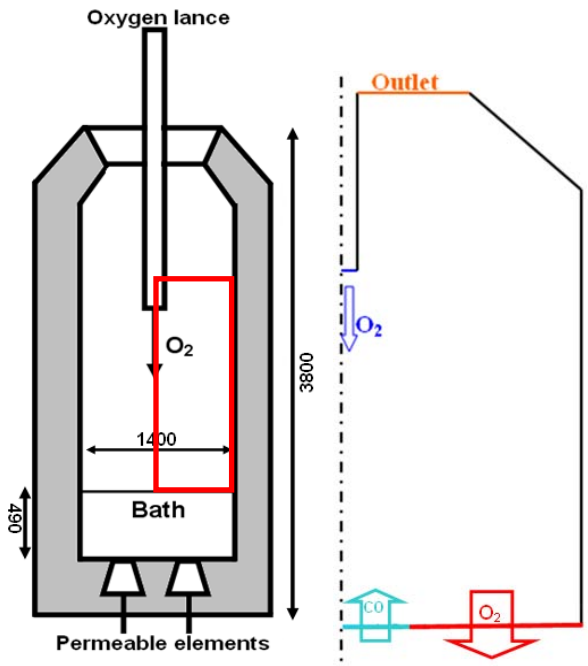

Figure 67: Geometry and boundary conditions of the 6t pilot.

The experimental values given for the 6t pilot by ArcelorMittal are as follows:

- Duration of the process: 5.9 min (354 s)
- Mass of carbon combusted in the bath: 41.8 kg
- Post-combustion ratio (**Chapter I , Eq. 29**) of the off-gases: 76%
- Measured temperatures inside the converter less than 2500 K [**62**]

Since some data are missing, we derived them from the procedure explained below.

The decarburisation and the post-combustion reactions are as follows:

$$\mathbf{1kg\ C + 4/3\ kg\ O_2 \rightarrow 7/3\ kg\ CO} \qquad \textbf{Eq. 78}$$

$$\mathbf{1kg\ O_2 + 7/4\ kg\ CO \rightarrow 11/4\ kg\ CO_2} \qquad \textbf{Eq. 79}$$

The decarburisation reaction (**Eq. 78**) shows that to oxidise 1 kg of carbon, 4/3 kg of oxygen is needed and 7/3 kg of CO is created. That means 55.73 kg of oxygen get in the bath in 5.9 min to combust 41.8 kg of carbon. Therefore the mass flowrates of oxygen entering the bath and of CO released from the bath are respectively: $\boxed{\dot{m}_{O_2,bath} = 0.157\ kg/s}$ and $\boxed{\dot{m}_{CO,bath} = 0.275\ kg/s}$.

The next step is to determine the total oxygen that enters the furnace through the lance and its velocity. In this step, it is assumed that all the oxygen not “absorbed” by the bath is consumed in the gaseous phase. Experimental and industrial observations have validated this assumption by showing no oxygen in the off gases analysis. Let x be the mass ratio of

oxygen getting in the bath ($x = \frac{\dot{m}_{O_2,bath}}{\dot{m}_{O_2,total}}$) and (1-x) the mass ratio of oxygen used for the post-combustion. We have then:

$$3x/4\ C + x\ O_2 \rightarrow 7x/4\ CO \qquad \textbf{Eq. 80}$$

$$(1\text{-}x)\ O_2 + 7x/4\ kg\ CO \rightarrow (11/4\text{-}11x/4)\ CO_2 + (7x/2\text{-}7/4)\ CO \qquad \textbf{Eq. 81}$$

Rewriting the post-combustion ratio, we have: $\text{pcr} = 0.76 = \frac{\frac{11}{4} - \frac{11}{4}x}{\frac{11}{4} - \frac{11}{4}x + \frac{7}{2}x - \frac{7}{4}} = \frac{11 - 11x}{4 + 3x}$ so $x = \frac{11 - 4\,\text{pcr}}{11 + 3\,\text{pcr}} = 0.6$. x was determined as the mass ratio of oxygen in the bath so: $x = \frac{\dot{m}_{O_2,bath}}{\dot{m}_{O_2,total}} \Rightarrow \dot{m}_{O_2,total} = \frac{\dot{m}_{O_2,bath}}{x}$; $\boxed{\dot{m}_{O_2,total} = 0.262\ \text{kg/s}}$

The velocity can be found as a function of the mass flowrate, density and nozzle outlet area as:

$$U_{O_2} = \frac{\dot{m}_{O_2,total} T_{O_2} R}{P W_{O_2} \pi R_n^2} \qquad \textbf{Eq. 82}$$

The relation between the temperature and the Mach number is given by **Eq. 12**. From this, we derived the relation between the temperature and the velocity as:

$$T_{O_2} = T_0 - \frac{\gamma - 1}{2\gamma R} W_{O_2} U_{O_2} \qquad \textbf{Eq. 83}$$

Iterative method is applied between **Eq. 82** and **Eq. 83** to know the temperature and the velocity of the oxygen at the nozzle outlet.

Uniform values of the velocity and the turbulence variables (k and ε) were specified at the nozzle outlet. The temperature of the nozzle wall has been set to 313 K since it is water cooled.

III.2.2.2 Results

Two lance heights of 2.2 m and 1 m have been studied. The first one leads to an undisturbed liquid surface while the latter to a cavity. Boundary conditions have been adjusted to match the experimental conditions.

III.2.2.2.1 Flat surface

The bath surface is assumed to be flat for a lance height of 2.2 m, since only a small depression is expected with the lance being so distant from the bath. Moreover in this case we do not take into account the oxygen absorbed by the bath, but only the CO exiting from the bath surface. When the lance is so far away from the bath surface, the decarburisation process occurs mainly with the product which is next to the depression zone. This case where CO_2 can also react with the carbon at the bath surface is not handled during this PhD.

The boundary conditions for this case are as follows:

- $\dot{m}_{O_2,bath} = 0\,\text{kg/s}$ so $\dot{m}_{O_2,total} = 0.105\,\text{kg/s}$
- U_{O2} = 197.62 m/s, determined from the iterative method (**Eq. 82** and **Eq. 83**)
- T_{O2} = 278.62 K, determined from the iterative method (**Eq. 82** and **Eq. 83**)

The mesh used for this set of simulations is depicted in **Figure 68** and contains 44x137 cells. As usual, the mesh has been refined near the jet entrance and near the bath surface.

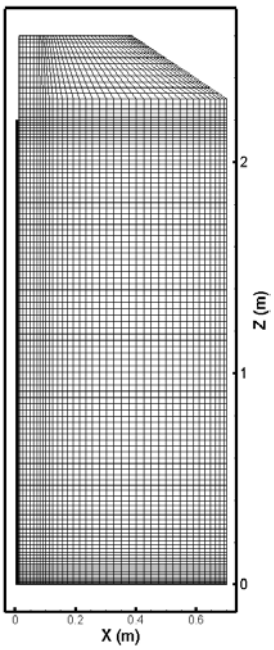

Figure 68: Mesh (44x137) of the 6t pilot simulation.

Different cases have been compared to a reference case to see the influence of various parameters on the model predictions (**Table 19**).

	Twall	Absorption and scattering coefficients	EBU coefficient
Reference	1000 K	0.3	1
Case 1	500K and 2000K	0.3	1
Case 2	1000 K	0.1 and 0.5	1
Case 3	1000 K	0.3	3 and 5

Table 19: Cases of the 6t simulations with lance height at 2.2 m.

Figure 69 represents the velocity and the temperature inside the 6t pilot for the reference case. We can see that the flow decays rapidly away from the lance outlet, it hits the bath surface and then it follows the bath surface and the converter wall until it leaves the domain through the outlet. A single recirculation zone is observed close to the bath, and the streamlines show strong entrainment of the gas from the bulk of the converter into the jet.

Regarding the temperatures, we can first see that they are a bit higher but in a realistic range (1600-2700 K outside the jet potential core). Moreover, the temperature decreases when going away from the bath. Indeed, the highest temperature near the bath is the place where the CO_2 created is pushed by the jet. Another important aspect to notice in this case is the large temperature values along the flame front (black curve in **Figure 69**) which is defined as the line where the mixture fraction is at its stoichiometric value.

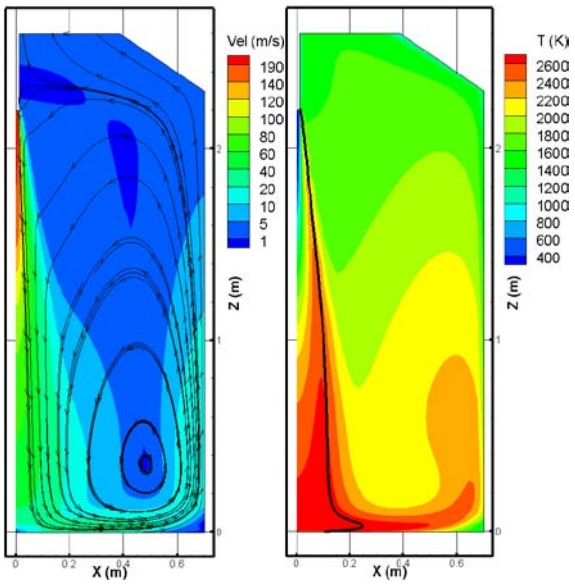

Figure 69: Streamlines, velocity and temperature distribution in the 6t pilot simulation (Ref. case).

Figure 70 represents the mass fraction of the species. One should observe that despite the O_2 being entirely consumed, there is some CO left inside the domain. As stated before, the CO_2 created is pushed to the bath surface by the jet as we can see in **Figure 70c**.

One explanation for the position of the flame front (black line in **Figure 69b**) at the jet boundary and near to the bath surface may be due to the fact that the bath surface is swept by the flow of oxidant coming from the jet at a high velocity and the reaction takes place then when the CO in entrained inside the surroundings of the jet. This explanation matches with the model proposed by Hirai et al. [**60**].

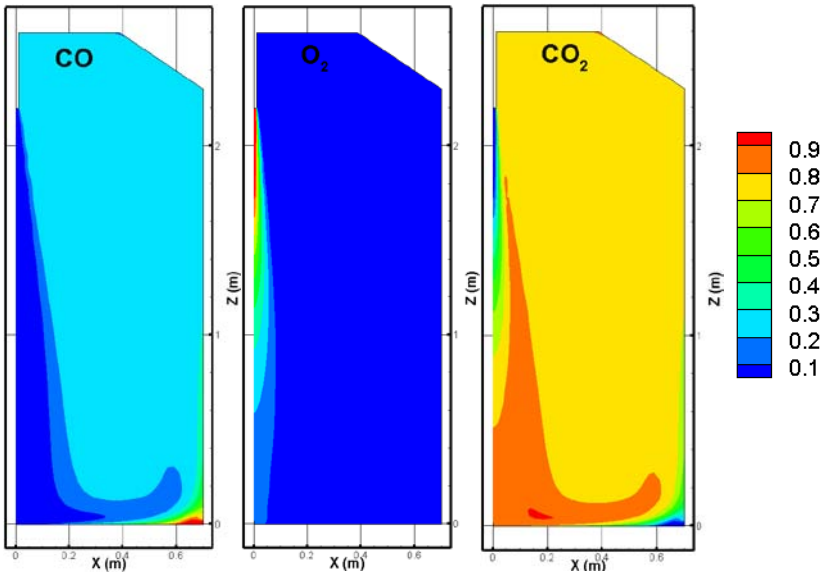

Figure 70: Species mass fraction distributions in the 6t pilot simulation (Ref. case): (a) CO, (b) O_2, (c) CO_2.

The post-combustion ratio at the converter outlet is numerically found to be 73.4%. This is in good agreement with the experimental data for this configuration which gives us a value around 76%.

Influence of the wall temperature (case 1)

The wall temperature has been estimated at 1000 K but in the real process, it varies substantially between the beginning and the end of the process. Comparisons have been made with wall temperature of 500, 1000 and 2000 K. The velocity and the species mass fraction do not change significantly with the wall temperature so only the temperature distribution has been depicted in **Figure 71**. The temperature distribution changes and its maximum value increases with the increase of the wall temperature. When increasing the wall temperature, we increase the radiated heat flux from the wall to the gaseous phase. The more the radiated flux, the higher the gaseous temperature.

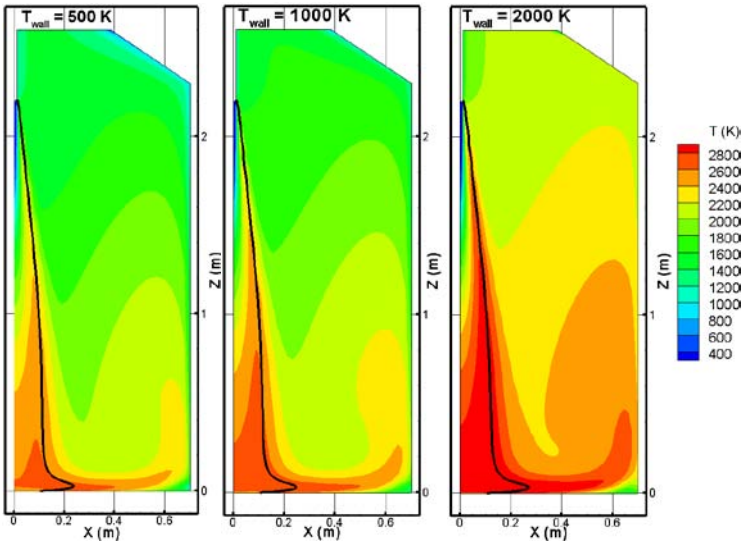

Figure 71: Temperature distribution for different wall temperatures: (a) 500K, (b) 1000K, (c) 2000K.

Influence of the absorption and scattering coefficients (case 2)

The scattering and the absorption coefficients are implemented in the radiosity calculation as a source for thermal energy redistribution. Their values change with the gaseous phase composition: dust, soot, gas composition etc. The actual values are unknown since there is no experimental measurement of light extinction length in the reactor. **Figure 72** depicts the only significant difference between the results for different values of the absorption and scattering coefficients: the temperature distribution. The temperatures inside the vessel decrease with the increase of the absorption and scattering coefficients. Indeed, these coefficients increase the proportion of the heat absorbed and scattered and therefore tend to decrease the temperatures in the gaseous phase.

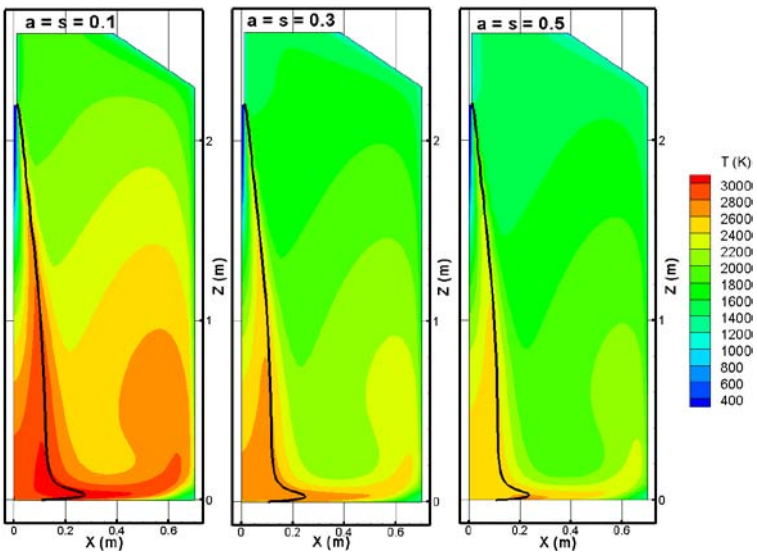

Figure 72: Temperature distribution for different absorption and scattering coefficients: (a)0.1 (b)0.3 (c)0.5.

Influence of the Eddy Break-up constant (case 3)

In the sink term of the equation of the remaining fuel (**Eq. 70**), the Eddy Break-Up coefficient has to be adjusted to the combustion case studied. In this case, a range of values of this coefficient from the literature [**88,90,91**] (i.e. 1 to 5) is tested. The calculated temperature distributions have been displayed in **Figure 73**. The temperatures inside the vessel increase with the increase of the Eddy Break-Up coefficient. Increasing the coefficient increases the reaction rate and so increases the product creation and the amount of heat released by the chemical reaction. **Figure 74** is coherent with these remarks since the mass fraction of product increases with the Eddy Break-Up coefficient.

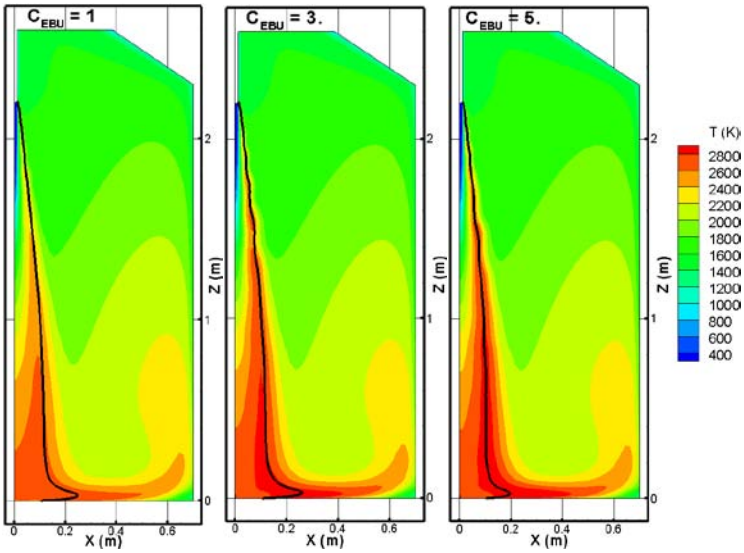

Figure 73: Temperature distribution for different Eddy Break-Up coefficients: (a) 1, (b) 3, (c) 5.

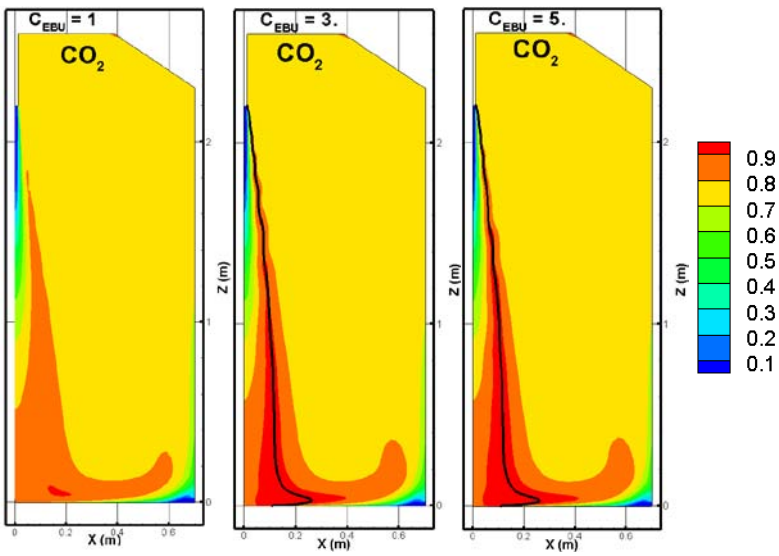

Figure 74: CO_2 mass fraction distribution for different Eddy Break-Up coefficient: (a) 1, (b) 3, (c) 5.

Summary

The different cases tested have been summarised in **Table 20** and compared on their maximum temperature and post-combustion ratio. Besides the concluding remarks drawn earlier in this section, we can highlight the fact that all the PCR values are in the same order of magnitude. The wall temperature, the absorption and the scattering coefficients and the Eddy Break-Up coefficient do not alter significantly the physics driven by the chemical reaction inside the gaseous part. In case 1, the maximum temperature increases with the wall temperature since we increase the radiated flux from the wall. The temperature can be brought down when increasing the absorption and the scattering coefficients since the radiated flux are less absorbed as it can be seen in case 2. In case 3, the maximum temperature increases with the EBU coefficient since we enhance the creation of the product and the associated heat released.

	Ref.	Case 1 (T_{wall})		Case 2 (absorption and scattering coefficients)		Case 3 (C_{EBU})	
		500 K	2000 K	0.1	0.5	3	5
Maximum temperature (K)	2776	2700	3028	3096	2634	2968	3033
PCR (%)	73.4	74.8	72.6	73.6	73.3	73.9	74.1

Table 20: Summary of the test cases on the 6t pilot (U_0=197 m/s, h_n=2.2 m).

III.2.2.2.2 Prescribed cavity

The bath surface was assumed flat in the previous test because the lance distance from the bath surface was high enough not to create a cavity. In the real process, a cavity is usually formed at the liquid metal surface while the post-combustion occurs in the gaseous phase. In this section the post-combustion is modelled with a time-averaged interface computed using the jet-cavity model (lance height at 1 m). A simple coupling is achieved. First a time-dependent case with a supersonic oxygen jet impinging onto a steel liquid surface is computed and the free surface profile is then time-averaged. Then the mesh is deformed according to the time-averaged cavity shape and the post-composition case is run.

The boundary conditions for this case are as follows:

- $\boxed{\dot{m}_{O_2,total} = 0.262 \text{ kg/s}}$ and $\boxed{\dot{m}_{O_2,bath} = 0.157 \text{ kg/s}}$
- U_{O2} = 385.6 m/s, determined from the iterative method (**Eq. 82** and **Eq. 83**)
- T_{O2} = 218 K, determined from the iterative method (**Eq. 82** and **Eq. 83**)
- T_{wall} = 1000 K
- C_{EBU}=1 and absorption and scattering coefficients are 0.3

As mentioned above, the mesh used for these simulations was deformed to fit the cavity shape on the liquid surface and is depicted in **Figure 75**. As usual, the mesh was refined near the jet entrance and near the bath surface. It is assumed that there is no mass ejection by the jet in the form of droplets into the top space.

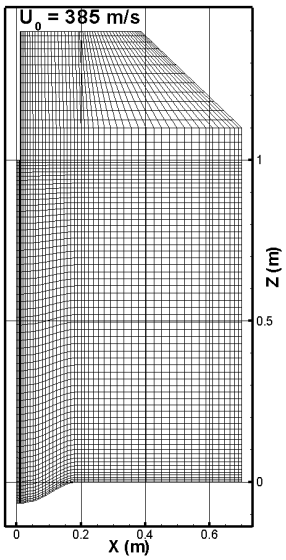

Figure 75: Deformed mesh (51x107 cells) for the 6t pilot (U_0=385 m/s and h_n=1 m).

The computed velocities and temperature are depicted in **Figure 76**. Similarly to the case with the flat surface, the streamlines show the path followed by the fluid. In this case, the cavity slightly changes the flow since the fluid sweeps off bath free surface before reaching the lateral wall. The reported temperatures on the same figure depict the highest values next to the bath surface. The temperatures are in the same order of magnitude in the bulk of the gaseous phase. Spots are reported at the inlet where the temperature is low and near the bath surface.

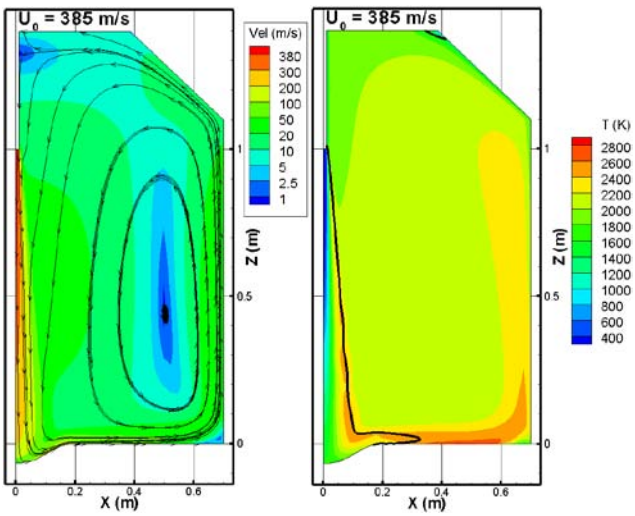

Figure 76: Streamlines, velocity and temperature distributions in the 6t pilot (U_0=385 m/s; h_n=1 m).

The oxygen is absent in the gaseous phase except in the jet region as it can be seen in **Figure 77**. We can also see that the CO mass fraction is less than 0.2 in the bulk of the gaseous phase meaning that almost all of it is combusted by the oxygen creating a high mass fraction of CO_2. Another interesting observation is in the last cell under the jet impingement. As stated before, a sink of oxygen at the cavity surface has been implemented.

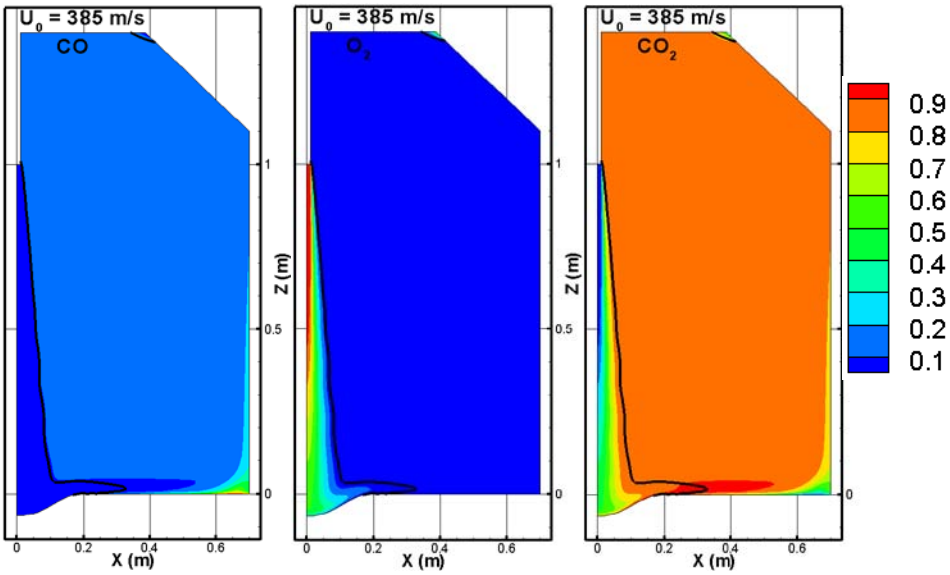

Figure 77: Species mass fraction distributions in the 6t pilot (U_0=385 m/s; h_n=1 m).

Simulations have been made for different velocities (500 and 615 m/s) and compared to the reference velocity. When increasing the velocity, we increase the oxygen reacting with the bath and therefore we increase the CO released from the bath. Since we defined our boundary conditions as a function of the PCR, the mass flowrate of CO is increased when increasing the O_2 velocity at the lance outlet. The computed velocity distributions are reported in **Figure 78** where we can see that the velocity streamlines are similar in all cases. The spots of low velocity reported at the centre of the recirculation loop and near the lance wall are the same whatever the inlet velocity. The increase in cavity depth is not important enough to create a deep cavity which will completely change the streamlines.

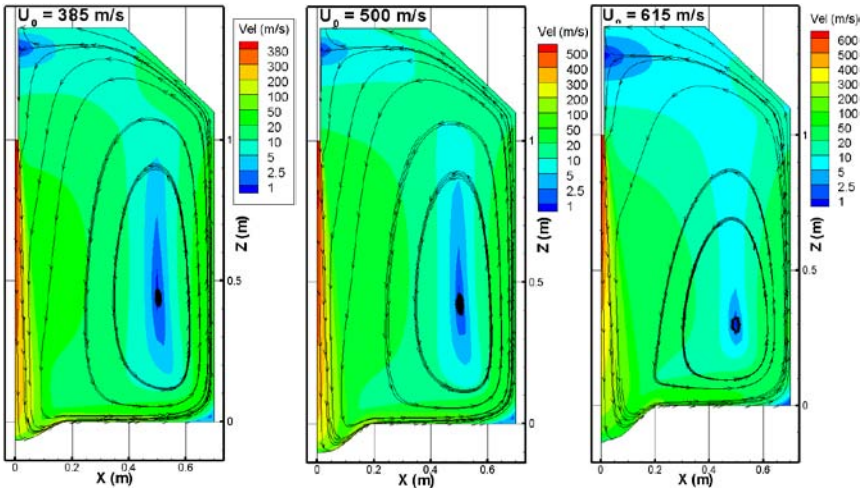

Figure 78: Streamlines and velocity distributions for different inlet velocity in the 6t pilot (h_n=1 m): a)U_0=385 m/s, b)U_0=500 m/s, c)U_0=615 m/s.

The comparison of the temperature distributions in **Figure 79** shows that the temperatures inside the vessel increase with the velocity. The increase of the velocity enhances indeed the proportion of the oxygen which sweeps the bath surface. This increases the CO_2 production and therefore the temperature. The flame front is still at the edge of the jet as reported earlier in this chapter.

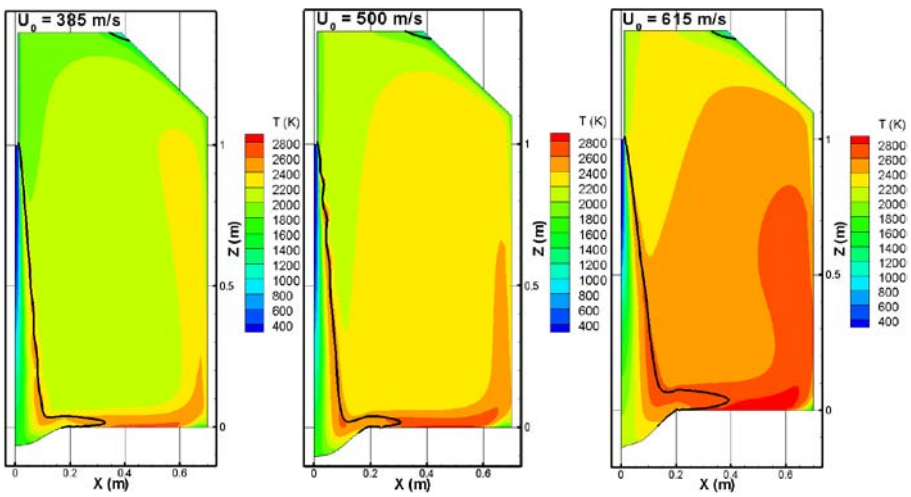

Figure 79: Temperature distributions for different inlet velocity in the 6t pilot (h_n=1 m): a)U_0=385 m/s, b)U_0=500 m/s, c)U_0=615 m/s.

The previous remarks are confirmed by **Figure 80** where we can see that the increase of the velocity increases the mass fraction of the CO_2 near the bath. This is more obvious when the inlet velocity is at 615 m/s. The PCR calculated for the different velocity values are 85, 82 and 87 % for inlet velocity of 385, 500 and 615 m/s respectively. The gas composition leaving the vessel is not significantly changed when increasing the velocity.

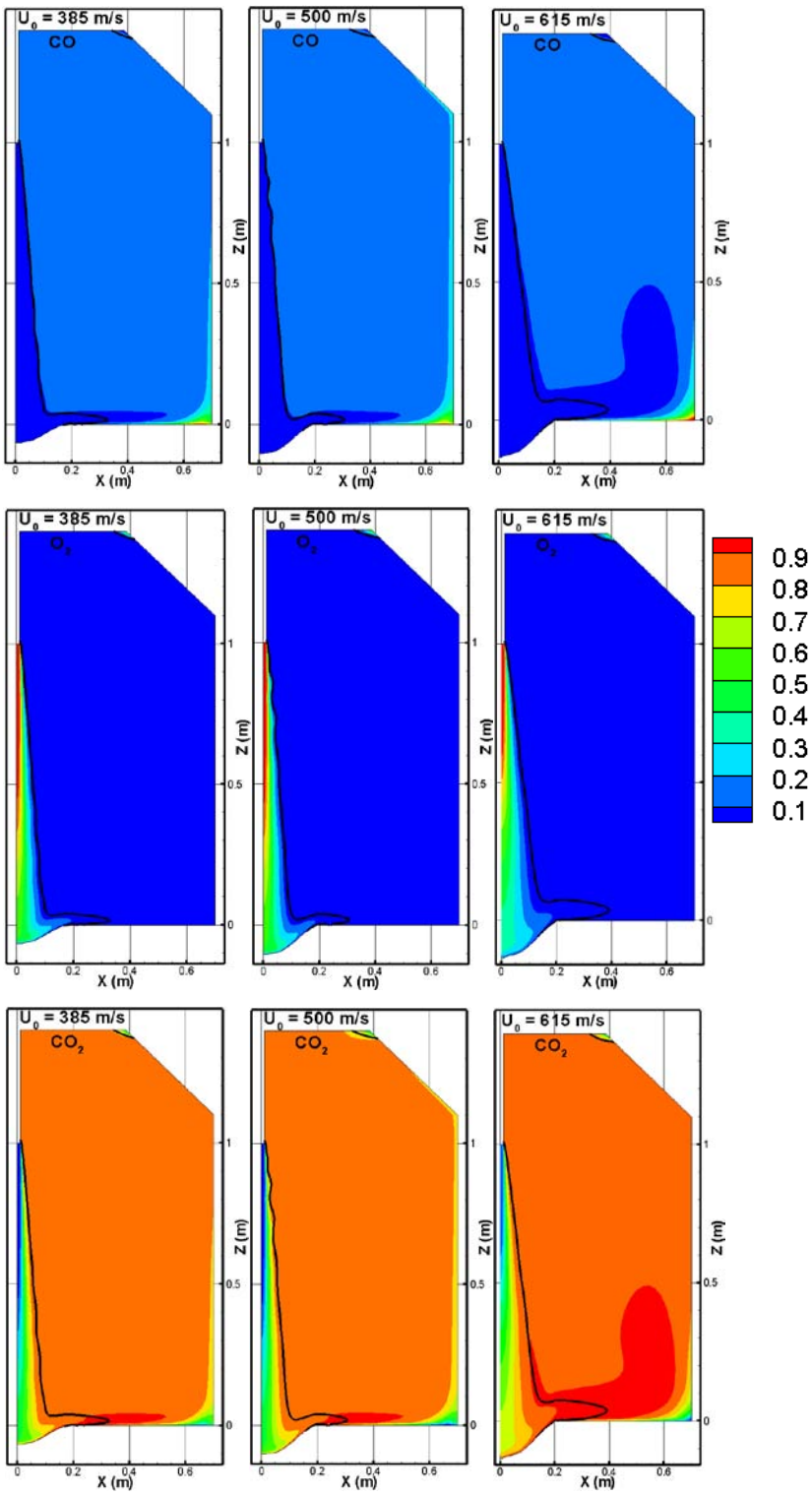

Figure 80: Species mass fraction distributions for different inlet velocity in the 6t pilot (h_n = 1 m): a) U_0=385 m/s, b) U_0=500 m/s, c) U_0=615 m/s.

III.2.3 Industrial converter

III.2.3.1 Boundary conditions

Our model has been tested on an industrial converter displayed in **Figure 81**. This converter is a top-blown converter with a lance containing 6 nozzles which works with 355 tons of steel. The boundary conditions taken from the industrial data are as follows:

- Lance: 6 de Laval nozzles with outlet diameter of 54.9 mm
- Inlet O_2 velocity: 514 m/s (Mach number of 2.18)
- T_{O2} : 152.5 K, corresponding to a density of 3.03 kg/m^3
- T_{bath} : 1873 K
- Ambient pressure: 1.2 bar
- Lance height: 1.5 m
- Mass flowrate of oxygen in the bath: 3.48 kg/s

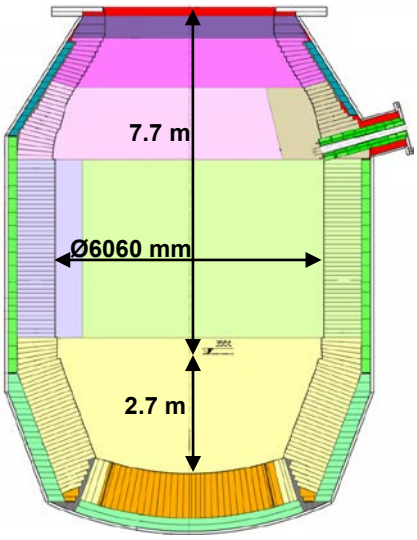

Figure 81: FOS converter.

Since our model is 2D axisymmetric, only one nozzle vertically oriented is modelled. Because of the latter, it was decided to reduce artificially the dimensions (i.e. the diameter and height of the converter). The mesh has been deformed following the time-averaged interface from a VOF simulation (**see Appendix B**) and is depicted in **Figure 82**.

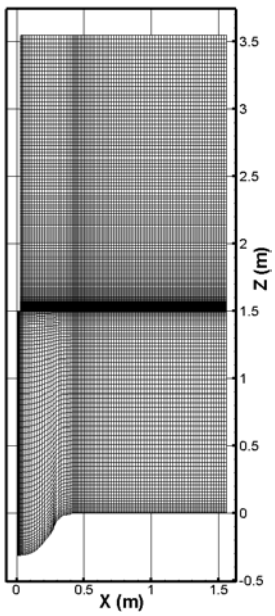

Figure 82: Mesh (95x232 cells) of the industrial converter.

III.2.3.2 Results

The velocity and the temperature distribution in the converter have been plotted in **Figure 83**. The streamlines indicate the path followed by the fluid after it leaves the lance outlet. The fluid velocity decays while approaching the bath surface. Once touching the bath surface, the gas is deviated and sweeps a part of the non-deformed bath surface before being entrained again inside the jet creating a recirculation loop. We can observe next to the jet boundary that the gas is entrained in the jet following waved streamlines.

As usual, the lowest temperature inside the vessel is the one of the oxygen jet. Outside the jet, a gradient of temperature can be observed with the temperature increasing towards the wall. The maximum temperature is located not far from the wall where the maximum mass fraction of CO_2 can be observed. The reported temperatures are in the range 1400-3000K in the bulk of the vessel. These temperatures are higher than the ones usually reported in the literature i.e. lower than 2500 K. This is partly due to the absence of the dissociation of the CO_2 above 2300K and the changes in the dimensions of the vessel. The black curve represents the flame front. As reported in the literature, it is located at the edge of the jet.

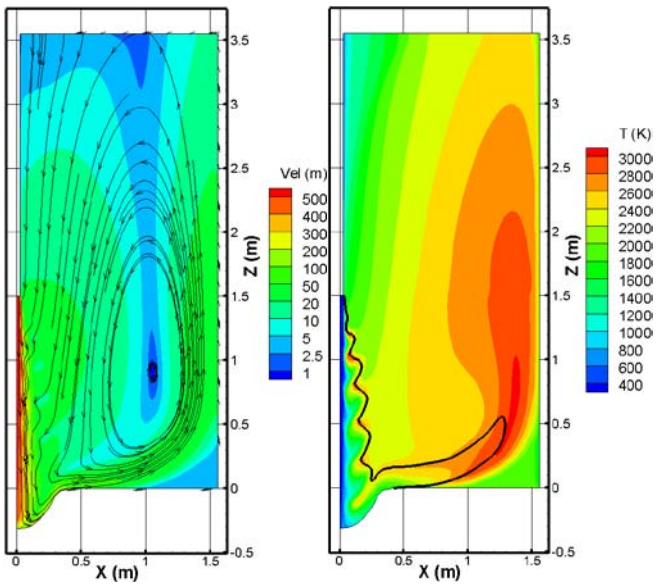

Figure 83: Streamlines velocity and temperature distributions in the FOS converter.

The mass fractions of the species are depicted in **Figure 84**. The CO is at its maximum near the wall of the vessel. Indeed, the CO leaves the bath only at the undisturbed surface of the bath and is swept by the oxygen from the lance. The non-combusted CO follows the wall. A part of it is entrained inside the oxygen jet while the rest leaves the vessel at the outlet located at the top of the furnace. The oxygen is totally consumed by the oxidation of CO. The "waves" mentioned earlier are more visible here since they are located at the boundary between the oxidant (oxygen) and the fuel (CO). It is important to note the abundance of oxygen inside the cavity. The CO_2 is the dominant species in the vessel except in the jet core and at the low corner of the vessel. In the centre of the recirculation loop, there is only CO_2. Indeed the flow enriches this region with new product created at the edge of the jet.

The PCR has been numerically found at 68%. This is much higher than the one industrially reported (11%) for this case. The assumptions made might explain this high PCR. Indeed, when neglecting the dissociation of CO_2, we increase the mass fraction of CO_2 leaving the vessel and therefore the PCR. Moreover, the vessel dimensions have been changed to account for the fact that only one nozzle is simulated. Decreasing the volume of the vessel reduces the total volume of the gas, mainly the CO in the gaseous phase. The decrease of CO leads to the increase of the PCR. At last, we considered that the gas entering the vessel by the outlet is purely CO_2 which can increase the total mass of CO_2, leaving the vessel.

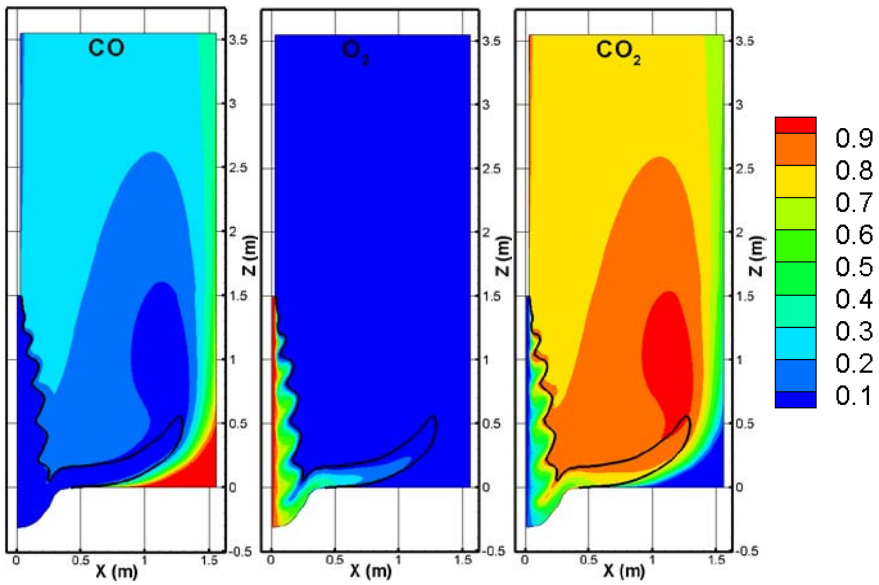

Figure 84: Species mass fraction inside the FOS converter: a) CO b) O_2 c) CO_2.

III.3 Conclusions

A mathematical model has been developed to simulate the post-combustion occurring in the gaseous phase of the steelmaking converter. After a description of the equations, the model has been tested on three different scales: a laboratory-scale experiment and 6-ton and 355-ton converters.

At the laboratory-scale, the model has been compared against experiments from Nippon Steel Corp. The computed mole fractions are in good agreement with the experimental results especially outside the oxygen jet. However, the spread of the jet has been found to be overpredicted by the model possibly due to a known deficiency of the standard k-ε turbulence model. The Eddy Break-Up model has been used to calculate the rate of the post-combustion reaction in this case whereas the flow is barely turbulent. The use of a more appropriate model (e.g. the Arrhenius model) could probably improve the predictions especially outside the jet.

Different tests have been performed on the 6-ton pilot and their results compared against the temperatures inside the bath and the post-combustion ratio. Two different configurations were analysed with the lance placed at 2.2 m and 1 m from the bath surface.
With the lance at 2.2 m, the bath surface was considered flat. Moreover, the loss of the oxygen inside the bath was not taken into account. The results show that the wall temperature, the Eddy-Break-Up constant and the absorption and scattering coefficients do

not have a drastic effect on the post-combustion ratio. However, these parameters influence the maximum temperature inside the vessel.

The surface is deformed by the creation of a cavity when the lance is located at 1 m from the bath surface. The cavity shape computed using the jet-cavity model was time-averaged and used to deform the mesh for the post-combustion model. At the cavity surface, a mass sink of oxygen has been applied to simulate its penetration into the bath. The increase in velocity increases the cavity depth and the production of CO_2 even if the PCR at the converter outlet is not affected. The flame front is located at the edge of the jet as expected and reported in the literature.

An industrial converter has also been simulated, considering a deformed bath free surface. The computed temperatures are a bit higher than the ones usually reported in the literature. The PCR calculated are higher than the one reported. This could be due to the size of the vessel simulated, the lack of dissociation of CO_2 and the gas considered entering the vessel by the outlet.

Conclusions and prospects

This PhD work was about the modelling of some aspects of the steelmaking converter. Two separate models were developed using the CFD code PHYSICA to simulate the deformation of the metal bath free surface under the oxygen jet impact and the post-combustion occurring in the gaseous phase respectively. We present here the concluding remarks drawn from the study and the future works which could be done following this project.

Conclusions

The first model describes the impingement of a gas jet onto a liquid surface. A multiphase mathematical model was presented, which deals with both incompressible and compressible fluid flows, energy transport and turbulence phenomena. The dynamic behaviour of the liquid free surface was solved using the VOF method. An approximate method, called zonal GALA, was used to account for the gas compressibility while also computing the deformation of the free surface. As the description of the gas jet development is of paramount importance when considering the impingement of a gas jet onto a liquid surface, we have first compared four different k-ε turbulence models for the simulation of the gas jet, by considering a test case investigated experimentally by Hussein et al. [**80**]. Among the models tested, the standard k-ε turbulence model has shown the smallest discrepancy with the experimental data, although the jet half width was over-predicted by 24 %. The model was then used to simulate two- and three-phase cold model experiments reported by Qian et al. [**35**]. First, we have tested the influence of different parameters on the cavity dimension predictions. A relatively coarse mesh (around 4000 cells) was found to be sufficient to prevent any significant influence of the mesh size on the model results. When comparing two different VOF schemes (Donor-Acceptor and Counter Diffusion Method) or two different differencing schemes of the convective fluxes (Smart and Hybrid), it was found that the cavity dimensions remain of the same order of magnitude. At the lance outlet, the specification of non-uniform profiles of the jet parameters leads to a deeper cavity than when using uniform profiles. Finally, the filtered k-ε model produces slightly deeper cavity than the standard k-ε model. The best agreement between the numerical predictions and the experimental results of Qian, but yet not completely satisfactory (the discrepancy is of 25 % for the cavity width), was obtained by combining the following parameters and models: uniform profiles of u, k and ε at the nozzle outlet, the Donor-Acceptor and Hybrid schemes and the standard k-ε turbulence model. Some results obtained for a 3-phase system (i.e. an air jet impacting a two-layer liquid bath) show a relatively good agreement with measurements made by Qian. As a last test case, the

model has been used to simulate the deformation of a liquid steel bath caused by a supersonic oxygen jet (with a Mach number ranging from 1.4 to 2.8) in a pilot scale converter. In this latter case, the cavity depth was observed to vary linearly with the jet velocity at the lance outlet. These depths are in reasonable agreement when compared to the experimental equation reported by Koria et al. [**32**].

A second mathematical model has been developed to simulate the behaviour of the gaseous phase in a steelmaking converter, considering hydrodynamic aspects, the post-combustion reaction and heat transfer (convection and radiation). Assuming that the rate of the post-combustion reaction is driven by the turbulent mixing, the sink term of fuel (i.e. CO) has been calculated with the Eddy Break-Up model. The penetration of a certain amount of oxygen in the bath, which is employed for the decarburisation of the metal, has also been tackled with the addition of a sink term at the cavity surface. The CO is supplied by the bath to the gaseous phase through the non-deformed interface. After a description of the equations related to the phenomena stated above, the model has been tested on three different scales: a laboratory experiment and 6-ton and 355-ton converters. On the laboratory scale, the post-combustion model has been compared against the experimental data reported by the Nippon Steel Corp. As far as the gas composition (i.e. O_2, CO and CO_2 concentrations) is concerned, a reasonable agreement has been found with the measurements. Indeed, the discrepancy between experimental and numerical results was observed to decrease from 30% to 2.5% when going away from the oxygen jet. The spread of the oxygen jet has been found to be over-predicted by our model since we use the standard k-ε turbulence model. Regarding the 6-ton converter, two different free surface deformations were tested: a flat free surface (corresponding to a lance height of 2.2 m) and a deformed (but fixed) free surface with a deep cavity (corresponding to a lance height of 1 m). For the flat surface, different tests were conducted regarding the effects of the specified values of the wall temperature, the absorption and scattering coefficients in the radiative transfer model and the Eddy Break-Up model constant. The PCR at the converter outlet was shown not to be affected by these parameters in opposite to the maximum temperature of the gas. When dealing with a deformed surface, the time-averaged cavity shape was determined in a separate simulation using the jet-cavity model. This result was then used as basis to deform the mesh used in the post-combustion simulation. Simulations were conducted for three different jet velocities varying between 385 and 615 m/s. Increasing the velocity increases the cavity depth and the production of CO_2 in the gaseous phase since the entrainment of the CO inside the jet is higher. Nevertheless, the PCR calculated in the offgases (around 84%) is not significantly affected by the velocity increase. The flame front in all cases (lance height at 1 and 2.2 m) is

located at the edge of the jet as reported in the literature. The gas temperatures and PCR values predicted by the model are in the same range than the ones observed experimentally. At last, the model has been used to simulate the post-combustion in an industrial converter. A part of the converter has been used in our model. The temperatures and the PCR have been found to be higher than those experimentally reported. This is partly due to the dissociation of CO_2 which is not taken into account in this simulation and to the fact that the actual dimensions of the vessel are not identified to the simulated ones.

Prospects

Various approximations have been made to develop the two models. Future work is needed to avoid some of these approximations and to consider additional phenomena. Regarding the jet-cavity model, the following developments would be necessary:

- The surface tension has been considered constant in our model. However, Morohoshi et al. [**92**] shows that the liquid metal surface tension is dependent on the temperature and the oxygen activity. Moreover, in our 3-phase model, the surface tension at each interface between the three fluids (air, liquid2 and water) should be considered.
- An approximate method (zonal-GALA) was used to handle the compressibility of the gas jet and the deformation of the liquid surface. Further work is necessary to allow for a full coupling between the gas compressible model and the calculation of the deformation of the free surface in order to avoid the need to treat the gas as incompressible near the free surface.

The post-combustion model can be improved on the following aspects:

- The post-combustion can be driven by turbulence or temperature. In our model, we supposed that it was only driven by turbulence and we therefore used the Eddy Break-Up model to calculate the sink term. When the flow is laminar, the post-combustion is driven by the temperature. To account for this case, an Arrhenius sink term may be used. The coupling of the Eddy Break Up and the Arrhenius terms will allow us to deal with all cases (laminar to turbulent).
- At high temperature (above 2300 K), CO_2 dissociates into CO and oxygen. To take into account this phenomenon, a limiting factor could be added to reduce the sink of fuel at high temperatures.

Regarding both models, turbulence modelling needs to be improved:

- Appropriate corrections of the standard k-ε turbulence model needs to be implemented to prevent the over-estimation of the spreading of the jet
- It would be desirable to improve the compressibility correction of the C_μ coefficient in the turbulent viscosity equation. In this study, we have assumed that this coefficient

remains uniform all over the domain. This needs to be modified to let it varies as a function of the local values of the temperature and Mach number.

Eventually, it would be desirable to fully couple the two models developed in the present study, which will allow to better understand the coupling between various phenomena. To couple the two main phases (gas and liquid), a model has been roughly imagined, named as "VOF chemistry" model. The trickiest part of this model will be related to the handling of transient mass and heat transfer between the two phases since the interface is moving with time.

As a final point, three main directions may be envisaged to further develop this coupled model of the converter:

- In the real process, multiple jets originating from a multi-hole lance impinge generally the surface of the liquid steel. Our model considers only a single jet of oxygen from the lance. It should be interesting to account for multiple jets by the use of a 3D model. This extension will help us to better understand the interaction between the jets and to design new lances to boost the decarburisation and the post-combustion.
- The generation of droplets at the jet impact has been discussed in the literature review but not yet considered in the model. Since the droplets may take part in the decarburisation process and in the transfer of heat from the gaseous phase to the bath, the modelling of the droplet behaviour (both in terms of trajectory and chemical evolution) would be of utmost importance in the future.
- The representation of the slag layer should be improved. The slag cannot be considered in the same way as the liquid steel since it is porous and its properties change with the blowing parameters.

References

[1]"How Steel is Made: Steelmaking Flowline." http://www.knightsbridgeinternational.ca/flowline/index.htm. [Accessed on 17-Oct-2011].

[2] G. Denier, "Aciéries de conversion - Aspects opérationnels, équipements et ingénierie," in *Les techniques de l'ingénieur*, 2010.

[3]"An Introduction to Iron and Steel Processing." http://www.jfe-21st-cf.or.jp/index2.html. [Accessed on 17-Oct-2011].

[4] A. Berthet, "Comparaison entre les procédés de conversion à soufflage par le haut et à soufflage par le fond," *Revue de Metallurgie. Cahiers D'Informations Techniques*, vol. 77, no. 3, pp. 213-228, 1980.

[5] S.C. Koria, "Principles and applications of gas injection in steelmaking practice," *Scandinavian Journal of Metallurgy*, vol. 22, no. 5, pp. 271-279, 1993.

[6] F. Kawa, "Beitrag zur Dimensionierung von Sauerstoffkonvertern (Contribution to the steelmaking converter sizing)," *Berg- und Hüttenmännische Monatshefte*, vol. 176, no. 9, p. 431, 1979.

[7]"Vadémécum ArcelorMittal." Internal document, IRSID, ArcelorMittal Maizières, 1994.

[8] N. Croft, K. Pericleous, and M. Cross, "PHYSICA: A multiphysics environment for complex flow processes," *Numerical Methods in Laminar and Turbulent Flow*, vol. 9, pp. 1269-1280, 1995.

[9] N. Rajaratnam, *Turbulent Jets*, Elsevier science Ltd. 1976.

[10] G.N. Abramovich, *The theory of turbulent jets*. Cambridge, Massachusetts: The MIT PRESS, 1963.

[11] P. Chassaing, *Turbulence en mécanique des fluides : analyse du phénomène en vue de sa modélisation à l'usage de l'ingénieur*. Cépaduès-Editions, 2000.

[12] C. Bailly and G. Comte-Bellot, *Turbulence*. CNRS Editions, 2003.

[13] M.H. Gazzah, M. Sassi, B. Sarh, and I. Gokalp, “Simulation numérique des jets turbulents subsoniques à masse volumique variable par le modèle k-epsilon,” *International Journal of Thermal Sciences*, vol. 41, no. 1, pp. 51-62, 2002.

[14] H.Y. Hwang, “A study of impinging gas jets on liquid surfaces,” PhD thesis, McMaster University, 2008.

[15] B. Cushman-Roisin, *Environnemental fluid mechanics*, John Wiley & Sons, Inc. 2009.

[16] E. Krause, *Fluid mechanics: with problems and s olutions*. Springer-Verlag Berlin and Heidelberg GmbH & Co. K, 2005.

[17] S. Candel, *Mécanique des fluides : Cours, 2nd edition*. Dunod, 2001.

[18] W.J. Devenport, “Flow pattern of de Laval nozzle,” *http://www.engapplets.vt.edu/fluids/CDnozzle/cdinfo.html*, 2009. .

[19] K. Naito, Y. Ogawa, T. Inomoto, S. Kitamura, and M. Yano, “Characteristics of jets from top-blown lance in converter,” *ISIJ International*, vol. 40, no. 1, pp. 23-30, 2000.

[20] V. Okhotskii, “Structure of gas jets,” *Steel in the USSR*, vol. 13, no. 11, pp. 489-490, 1983.

[21] B. Allemand, P. Bruchet, C. Champinot, S. Melen, and F. Porzucek, “Theoretical and experimental study of supersonic oxygen jets. Industrial application in EAF,” *Revue de Metallurgie. Cahiers D'Informations Techniques*, vol. 98, no. 6, pp. 571-587, 2001.

[22] H. Odenthal, J. Kempken, J. Schlu?ter, and W. Emling, “Advantageous numerical simulation of the converter blowing process,” *Iron and Steel Technology*, vol. 4, no. 11, pp. 71-89, 2007.

[23] Yukari TAGO and Yoshihiko HIGUCHI, “Fluid Flow Analysis of Jets from Nozzles in Top Blown Process,” *ISIJ International*, vol. 43, no. 2, pp. 209-215, Oct 2002.

[24] S. Eletribi, D.K. Mukherjee, and V. Prasad, “Experiments on liquid surface deformation upon impingement by a gas jet,” *American Society of Mechanical Engineers, Fluids Engineering Division (Publication) FED*, vol. 244, pp. 43-52, 1997.

[25] S.K. Sharma, J.W. Hlinka, and D.W. Kern, “The bath circulation, jet penetration and high temperature reaction zone in BOF steelmaking,” *Steelmaking Conference Proceedings, ISS*, vol. 60, pp. 181-197, 1977.

[26] R.B. Banks and D.V. Chandrasekhara, “Experimental investigation of the penetration of a high-velocity gas jet through a liquid surface,” *Journal of Fluid Mechanics*, vol. 15, no. 1, pp. 13-35, 1963.

[27] N.A. Molloy, “Impinging jet flow in a two-phase system. The basic flow pattern,” *J. Iron Steel Inst*, vol. 208, no. 10, pp. 943-950, 1970.

[28] W.E. Olmstead and S. Raynor, “Depression of an infinite liquid surface by an incompressible gas jet,” *Journal of Fluid Mechanics Digital Archive*, vol. 19, no. 4, pp. 561-576, 1964.

[29] T. Kumagai and M. Iguchi, “Instability phenomena at bath surface induced by top lance gas injection,” *ISIJ International*, vol. 41, pp. 52-55, 2001.

[30] A. Balabel, “RANS modeling of gas jet impinging onto a deformable liquid surface,” *Emirates Journal for Engineering Research*, vol. 12, no. 3, pp. 35-46, 2007.

[31] A. Nordquist, N. Kumbhat, L. Jonsson, and P. Jonsson, “The effect of nozzle diameter, lance height and flow rate on penetration depth in a top-blown water model,” *Steel Research International*, vol. 77, no. 2, pp. 82-90, 2006.

[32] S.C. Koria and K.W. Lange, “Penetrability of impinging gas jets in molten steel bath,” *Steel Research*, vol. 58, no. 9, pp. 421-426, 1987.

[33] T. Shimada, T. Akiyama, E. Kasai, and J.-I. Yagi, “Observation of molten slag surface under gas impingement by X-ray Computed Tomography,” *ISIJ International*, vol. 40, no. 10, pp. 958-963, 2000.

[34] F.R. Cheslak, J.A. Nicholls, and M. Sichel, “Cavities formed on liquid surfaces by impinging gaseous jets,” *Journal of Fluid Mechanics*, vol. 36, no. 1, pp. 55-63, 1969.

[35] F. Qian, R. Mutharasan, and B. Farouk, “Studies of interface deformations in single- and multi-layered liquid baths due to an impinging gas jet,” *Metallurgical and M aterials Transactions B*, vol. 27, no. 6, pp. 911-920, 1996.

[36] O. Olivares, A. Elias, R. Sanchez, M. Diaz-Cruz, and R. Morales, “Physical and mathematical models of gas-liquid fluid dynamics in LD converters,” *Steel Research*, vol. 73, no. 2, pp. 44-51, 2002.

[37] A.R.N. Meidani, M. Isac, A. Richardson, A. Cameron, and R.I.L. Guthrie, “Modelling shrouded supersonic jets in metallurgical reactor vessels,” *ISIJ International*, vol. 44, no. 10, pp. 1639-1645, 2004.

[38] D. Huin, “Profondeur de pénétration d'un jet d'oxygène dans le métal liquide.” Internal report, IRSID, ArcelorMittal Maizières, 1986.

[39] J. Szekely and S. Asai, “Turbulent fluid flow phenomena in metals processing operations: Mathematical description of the fluid flow field in a bath caused by an impinging gas jet,” *Metallurgical Transactions*, vol. 5, no. 2, pp. 463-467, 1974.

[40] D.H. Wakelin, PhD thesis, Imperial College, University of London, 1966.

[41] J. Zhang, S. Du, and S. Wei, “Flow field in bath agitated by symmetrically placed impinging gas jet and submerged gas stream,” *Ironmaking and Steelmaking*, vol. 12, no. 6, pp. 249-255, 1985.

[42] A.V. Nguyen and G.M. Evans, “Computational fluid dynamics modelling of gas jets impinging onto liquid pools,” *Applied Mathematical Modelling*, vol. 30, no. 11, pp. 1472-1484, 2006.

[43] “ANSYS Fluent Flow Modeling Simulation Software.” http://www.ansys.com/Products/Simulation+Technology/Fluid+Dynamics/ANSYS+Fluent. [Accessed on 17-Oct-2011]

[44] M. Ersson, A. Tilliander, L. Jonsson, and P. Jonsson, “A mathematical model of an

impinging air jet on a water surface," *ISIJ International*, vol. 48, no. 4, pp. 377-384, 2008.

[45] M. Ersson, A. Tilliander, and P. Jonsson, "Coupled thermodynamic and kinetic modeling of a top-blown bath," Proceedings of Sohn International Symp. Advanced Processing of metals and materials, Thermo and Physicochemical Principles, Stockholm, Sweden, 2006, vol. 2, pp. 271-281.

[46] M. Ersson, L. Hoglund, A. Tilliander, L. Jonsson, and P. Jonsson, "Dynamic coupling of computational fluid dynamics and thermodynamics software: Applied on a top blown converter," *ISIJ International*, vol. 48, no. 2, pp. 147-153, 2008.

[47]"Thermo-Calc Software - Home." http://www.thermocalc.com/. [Accessed on 17-Oct-2011]

[48] M. Barron, C. Lopez, and I. Hilerio, "Numerical evaluation of the performance of a BOF steelmaking lance," 2008, pp. 303-310.

[49] S. Koria and K. Lange, "A new approach to investigate the drop size distribution in basic oxygen steelmaking," *Metallurgical Transactions B*, vol. 15, no. 1, pp. 109-116, 1984.

[50] N. Standish and Q.L. He, "Drop generation due to an impinging jet and the effect of bottom blowing in the steelmaking vessel," *ISIJ International*, vol. 29, no. 6, pp. 455-461, 1989.

[51] Q.L. He and N. Standish, "Model study of droplet generation in the BOF steelmaking," *ISIJ International*, vol. 30, no. 4, pp. 305-309, 1990.

[52] Qing Lin He and N. Standish, "Model study of residence time of metal droplets in the slag in BOF steelmaking," *ISIJ International*, vol. 30, no. 5, pp. 356-361, 1990.

[53] Y. Higuchi and Y. Tago, "Effect of lance design on jet behavior and spitting rate in top blown process," *ISIJ International*, vol. 41, no. 12, pp. 1454-1459, 2001.

[54] M. Luomala, T. Fabritius, E. Virtanen, T. Siivola, and J. Härkki, "Splashing and spitting behaviour in the combined blown steelmaking converter," *ISIJ International*, vol. 42, no. 9, pp. 944-949, 2002.

[55] Subagyo, G.A. Brooks, K. Coley, and G. Irons, “Generation of droplets in slag-metal emulsions through top gas blowing,” *ISIJ International*, vol. 43, no. 7, pp. 983-989, 2003.

[56] Y. Higuchi and Y. Tago, “Effect of nozzle twisted lance on jet behavior and spitting rate in top blown process,” *ISIJ International*, vol. 43, no. 9, pp. 1410-1414, 2003.

[57] A. Koohi, M. Halali, M. Askari, and M. Manzari, “Investigation and modeling of splashing in the Peirce Smith converter,” *Chemical Product and Process Modeling*, vol. 3, no. 1, 2008.

[58] N.I. Kolev, *Multiphase Flow Dynamics 2: Thermal and Mechanical Interactions*, 3 ed., vol. 2. Springer, 2005.

[59] H. Gou, G. Irons, W. Lu, and Z. Du, “Entrainment and post-combustion in oxygen jets under steelmaking and smelting/reduction conditions,” *I&SM*, vol. 22, no. 1, pp. 47-54, 1995.

[60] M. Hirai, R. Tsujino, T. Mukai, T. Harada, and M. Omori, “Mechanism of post combustion in the converter,” *Transactions of the Iron and Steel Institute of Japan*, vol. 27, no. 10, pp. 805-813, 1987.

[61] D. Huin, J. Landry, J. Reboul, and Y. Zbaczyniak, “Study of post combustion mechanisms in a 6 t pilot oxygen converter,” *Revue de Metallurgie. Cahiers D'Informations Techniques*, vol. 86, no. 10, pp. 775-781, 1989.

[62] D. Huin, H. Gaye, J.P. Reboul, and Y. Zbaczyniak, “Modélisation de la post-combustion au convertisseur.” Internal report, IRSID, ArcelorMittal Maizières, 1988.

[63] D. Nakazono, K. Abe, M. Nishida, and K. Kurita, “Supersonic O2-jet impingement on liquid iron with surface chemistry,” *ISIJ International*, vol. 44, no. 1, pp. 91-99, 2004.

[64] J. Huber, J. Lehmann, and R. Cadet, “Comprehensive dynamic model for BOF process: A glimpse into thermal efficiency mechanisms,” *Revue de M etallurgie. Cahiers D'Informations Techniques*, vol. 105, no. 3, pp. 121-126+III-IV, 2008.

[65] L. Zhang and F. Oeters, “Model of post-combustion in iron-bath reactors, part 1: theoretical basis,” *Steel Research*, vol. 62, no. 3, pp. 95-106, 1991.

[66] L. Zhang and F. Oeters, “Model of post-combustion in iron-bath reactors, part 2: results for combustion with oxygen,” *Steel Research*, vol. 62, no. 3, pp. 107-116, 1991.

[67] H. Gou, G. Irons, and W. Lu, “Mathematical modeling of postcombustion in a KOBM converter,” *Metallurgical Transactions B*, vol. 24, no. 1, pp. 179-188, 1993.

[68] S.T. Johansen, J. Wu, and W. Shyy, “Filter-based unsteady RANS computations,” *International Journal of Heat and Fluid Flow*, vol. 25, no. 1, pp. 10-21, 2004.

[69]“PHYSICA Documentation.” http://staffweb.cms.gre.ac.uk/~physica/. [Accessed on 24-Aug-2011].

[70] D.B. Spalding, “A novel finite difference formulation for differential expressions involving both first and second derivatives,” *International Journal for Numerical Methods in Engineering*, vol. 4, no. 4, pp. 551-559, 1972.

[71] P.H. Gaskell and A.K.C. Lau, “Curvature-compensated convective transport: SMART, A new boundedness- preserving transport algorithm,” *International Journal for Numerical Methods in Fluids*, vol. 8, no. 6, pp. 617-641, 1988.

[72] C.W. Hirt and B.D. Nichols, “Volume of fluid (VOF) method for the dynamics of free boundaries,” *Journal of Computational Physics*, vol. 39, no. 1, pp. 201-225, 1981.

[73] K. Pericleous, G. Djambazov, B. Lebon, T.-N. Croft, J.-F. Domgin, and P. Gardin, “Time-dependent modelling and experimental validation of the metal/flux interface in a continuous casting mould,” *Revue de Metallurgie. Cahiers D'Informations Techniques*, vol. 105, no. 1, pp. 207-217, 2008.

[74] G.S.B. Lebon, “Unstructured finite volume algorithms for compressible multiphase flow,” University of Greenwich, 2011.

[75] S. Heinz, “A model for the reduction of the turbulent energy redistribution by compressibility,” *Physics of Fluids*, vol. 15, no. 11, pp. 3580-3583, 2003.

[76] K. Abdol-Hamid, S. Paul Pao, S. Massey, and A. Elmiligui, “Temperature corrected

turbulence model for high temperature jet flow," *Journal of Fluids Engineering, Transactions of the ASME*, vol. 126, no. 5, pp. 844-850, 2004.

[77] M. Alam, J. Naser, and G. Brooks, "Computational fluid dynamics simulation of supersonic oxygen jet behavior at steelmaking temperature," *Metallurgical and Materials Transactions B: Process Metallurgy and Materials Processing Science*, vol. 41, no. 3, pp. 636-645, 2010.

[78] D.C Wilcox, *Turbulence modeling for CFD*, DCW Industries. 1994.

[79] I. Sumi, Y. Kishimoto, Y. Kikuchi, and H. Igarashi, "Effect of high-temperature field on supersonic oxygen jet behavior," *ISIJ International*, vol. 46, no. 9, pp. 1312-1317, 2006.

[80] H.J. Hussein, S.P. Capp, and W.K. George, "Velocity measurements in a high-Reynolds-number, momentum-conserving, axisymmetric, turbulent jet," *Journal of Fluid Mechanics*, vol. 258, pp. 31-75, 1994.

[81] S.B. Pope, "An explanation of the turbulent round-jet/plane-jet anomaly," *AIAA Journal*, vol. 16, no. 3, pp. 279-281, 1978.

[82] T. Shih, W. Liou, A. Shabbir, Z. Yang, and J. Zhu, "A new k-ε eddy viscosity model for high reynolds number turbulent flows," *Computers and Fluids*, vol. 24, no. 3, pp. 227-238, 1995.

[83] B.E. Launder, "Second-moment closure: present... and future?," *International Journal of Heat and Fluid Flow*, vol. 10, no. 4, pp. 282-300, 1989.

[84] P.A. Durbin, "Separated flow computations with the k-ε-v2 model," *AIAA journal*, vol. 33, no. 4, pp. 659-664, 1995.

[85] D. Rutledge, *Study of a gas jet impinging a liquid surface*, Internship final report, Institut Jean Lamour, Nancy (France), 2009.

[86] D.B. Spalding, *Combustion and Mass Transfer*, 1er ed. Elsevier, 1978.

[87] I. Glassman, *Combustion, Third Edition*. Academic Press, 1996.

[88] L. Hjertager, B. Hjertager, and T. Solberg, “CFD modelling of fast chemical reactions in turbulent liquid flows,” *Computers and Chemical Engineering*, vol. 26, no. 4, pp. 507-515, 2002.

[89] A. Kaizawa, N. Sasaki, T. Inomoto, and Y. Ogawa, “Influence of post combustion on characteristics of oxygen jet in BOF,” Proceedings of 8th International Conference on CFD in Oil & Gas, Metallurgical and Process Industries SINTEF/NTNU, Trondheim, Norway, 2011.

[90] Thierry Poinsot and Denis Veynante, *Theoretical and numerical combustion, Second edition*. R.T. Edwards, Inc., 2005.

[91] F.A. Williams, *Combustion theory: The fundamental theory of chemically reacting flow systems*, 2 ed. Benjamin-Cummings Publishing Company, 1985.

[92] K. Morohoshi, M. Uchikoshi, M. Isshiki, and H. Fukuyama, “Surface tension of liquid iron as functions of oxygen activity and temperature,” *ISIJ International*, vol. 51, no. 10, pp. 1580-1586, 2011.

Appendix A: Industrial converter: jet-cavity simulation

In **Chapter II** , the impingement of a supersonic oxygen jet onto a liquid steel surface in a 6 ton converter has been simulated (**Section II.6**). In this appendix, the model on a full scale industrial configuration (i.e. 335-ton converter) is tested, characterized by the following conditions:

- Bath diameter: 1.55 m
- Blowing conditions: U_{O2} = 514 m/s (Mach number of 2.18), T_{O2}=152.5 K corresponding of a density of 3.03 kg/m^3
- Lance height: 1.5 m
- Nozzle diameter: 54.9 mm

For the simulation, a mesh consisting of 85x192 cells is used (**Figure 85**).

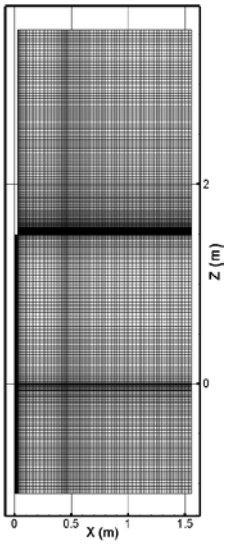

Figure 85: Mesh (85x192 cells) of a full scale industrial converter.

Figure 86 shows the transient evolution of the velocity distribution and of the streamlines in the gas phase when the liquid metal is impinged by the supersonic oxygen jet. Similarly to the 6t pilot case, the jet is strongly decelerated while going away from the lance outlet and hitting the bath creating a cavity. However, in the present case, the cavity is so deep that the flow out of the cavity does not entirely sweep the bath. This leads to the formation of two recirculation loops observed in the gaseous phase. The first one is located near the edge of the cavity and the second one is close to the lateral wall of the vessel. One should note that the entrainment of the surrounding gas into the jet is responsible of the near-cavity-edge-loop.

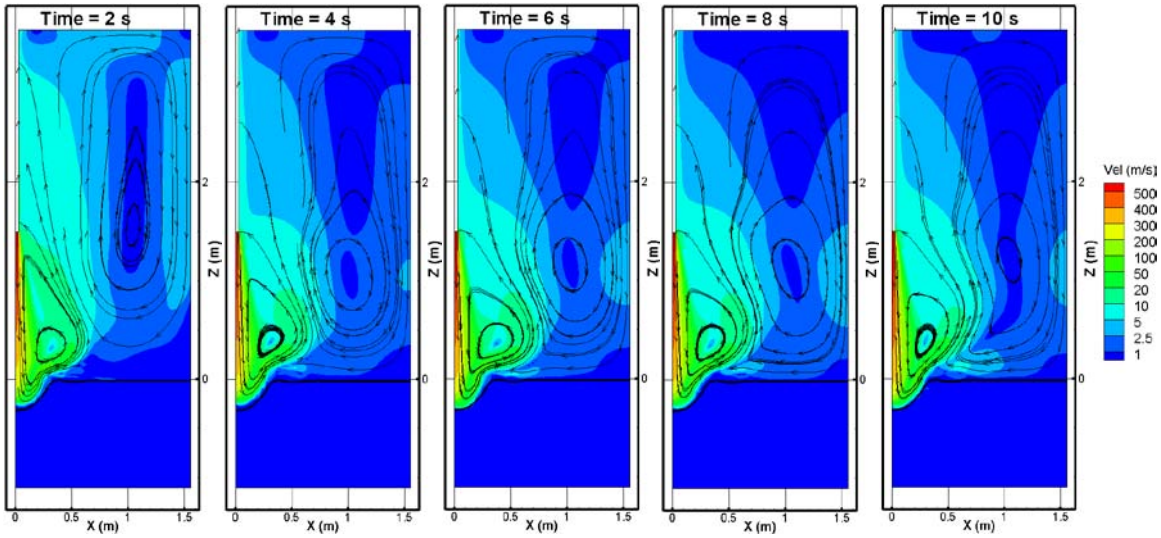

Figure 86: Distribution of the velocity magnitude and streamlines in the gas phase at different time instants.

The time-averaged density distribution is depicted in **Figure 87**. The black line in this figure represents the iso-contour line of the Mach number relative to a value of 0.3. Inside this contour, the flow is considered compressible and outside it is incompressible. As it can be seen, the jet is still compressible at the initial bath level.

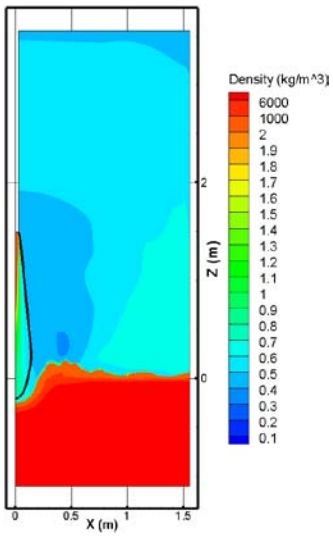

Figure 87: Time-averaged density distribution.

The instantaneous and time-averaged profiles of the cavity are plotted in **Figure 88**. The instantaneous profiles are observed to fluctuate around the time-averaged one. The time-averaged cavity is 319 mm deep and 400 mm wide. These dimensions are significantly higher than the ones reported in the simulations of the 6t pilot.

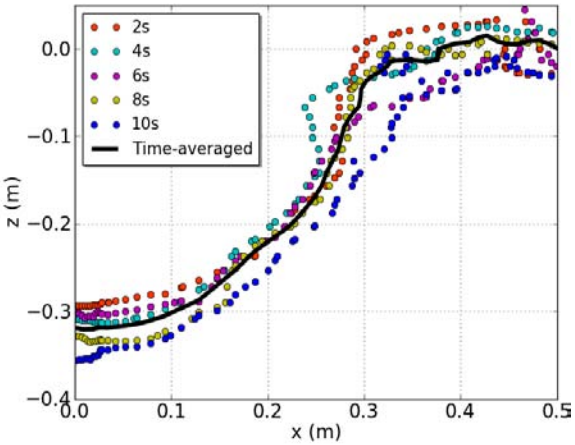

Figure 88: Profile of the gas-metal interface.

The operating values of the Mach number are between 2 and 2.4 for the oxygen out of the nozzle [**5**]. Simulations have been run in this range.

Figure 89 shows the density map for three different Mach numbers at the inlet. One can note the obvious increase of the cavity and compressible region dimensions with the velocity.

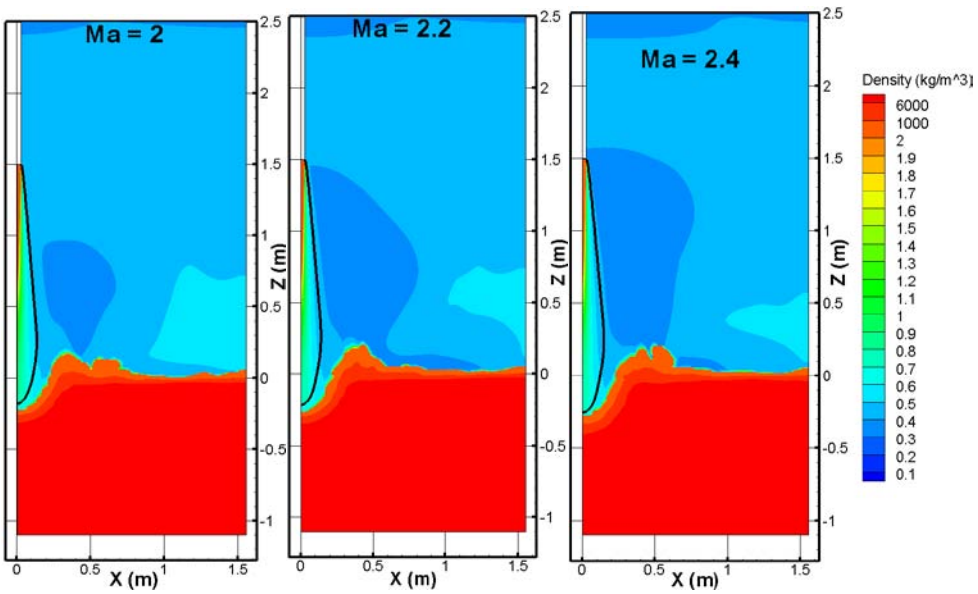

Figure 89: Time-averaged density distribution for three different Mach numbers at the inlet. The black curve represents the isoline of the Mach number relative to a value of 0.3.

The time-averaged gas-liquid interfaces computed for each case are displayed in **Figure 90**.

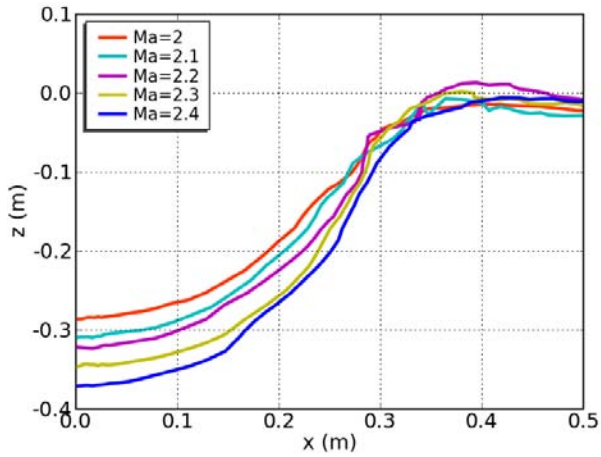

Figure 90: Profile of the gas-metal interface for different Mach number.

The cavity depths reported in **Figure 90** have been compared against the inlet velocity. In **Figure 91**, it is interesting to see that similarly to what was observed for the 6-ton pilot simulation, the cavity depth varies again linearly with the inlet velocity.

$$h_{cav}(m) = -879.2.10^{-6}\ U_0 + 128.04.10^{-3} \qquad \textbf{Eq. 84}$$

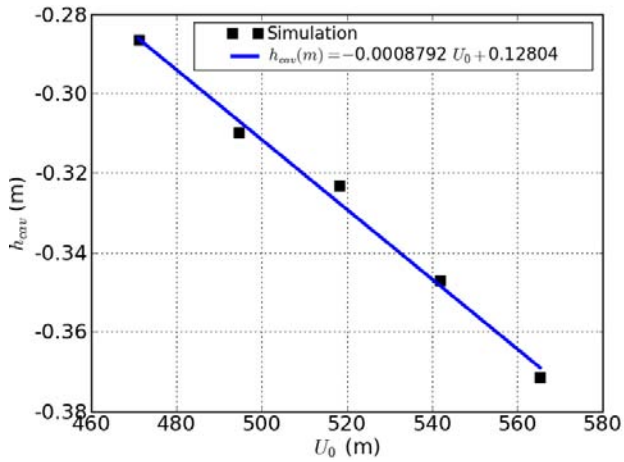

Figure 91: Depth of the cavity as a function of the inlet velocity.

Résumé étendu en français

Introduction

Le convertisseur d'aciérie est le procédé qui permet de convertir la fonte issue des hauts-fourneaux en acier liquide. Cette conversion est faite par soufflage d'oxygène pur à la surface de la fonte liquide permettant sa décarburation. Dans les convertisseurs de type "top blown converter", l'oxygène est introduit à vitesse supersonique via une lance située verticalement au-dessus du bain entrainant la création d'une cavité à la surface du bain métallique (Figure 1). Les dimensions et la forme de la cavité sont des paramètres importants car elles contrôlent l'aire de l'interface réactionnelle entre l'oxygène et le métal. La réaction de décarburation produit du monoxyde de carbone (CO) qui peut aussi réagir avec l'oxygène de la phase gazeuse produisant ainsi du dioxyde de carbone (CO_2). Cette réaction est la postcombustion et est très exothermique (deux fois plus que celle de décarburation). Améliorer l'efficacité énergétique du procédé est nécessaire afin de pouvoir augmenter le taux de ferrailles recyclées dans le convertisseur. Cela peut être réalisé en favorisant la postcombustion et le transfert de la chaleur produite par cette réaction vers le bain de métal liquide. Le travail de thèse présentée dans ce document est inclus dans un projet de recherche visant à développer un modèle unifié du convertisseur d'aciérie. Dans ce document, deux aspects majeurs du convertisseur sont abordés : la déformation de la surface libre du bain de métal due à l'impact du jet gazeux et les transferts couplés, y compris la postcombustion, dans la phase gazeuse.

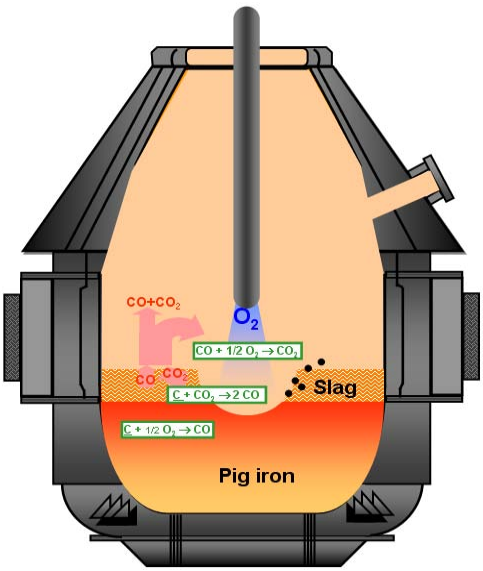

Figure 92: Schéma du convertisseur d'aciérie.

De nombreuses études de la bibliographie traitent de l'impact d'un jet gazeux sur une surface déformable. Les expériences, depuis celles de Banks and Chandrasekhara [1] dans les années soixantes à celles récemment faites par Nordquist et al. [2], ont été effectuées en utilisant, pour des raisons pratiques, des maquettes froides dans lesquelles l'oxygène est remplacé par de l'air et l'acier liquide par de l'eau. Ces expériences ont eu pour but de visualiser les dimensions de la cavité et mettre en place des corrélations permettant de calculer ces dimensions. Pour une synthèse des résultats de ces différentes expériences, nous renvoyons le lecteur à l'article de Nordquist et al. [2]. D'un point de vue théorique, plusieurs simulations numériques de la déformation de la surface libre d'un bain liquide due à l'impact d'un jet gazeux ont également été rapportées. L'approche la plus couramment utilisée pour représenter les déformations de la surface libre du bain est la méthode "Volume Of Fluid" (VOF) (e.g. [3-6]). Presque tous les modèles traitent le jet gazeux comme un fluide incompressible, ce qui limite leur champ d'application à des jets subsoniques à faibles vitesses. Seul le travail d'Odenthal et al. [5] prend en compte, de manière approximative, les effets de compressibilité dans un jet supersonique.

La bibliographie existante sur les phénomènes physiques et chimiques dans la phase gazeuse du convertisseur, en particulier sur la réaction de postcombustion, est plus rare. Des études numériques ont été rapportées, par exemple par Zhang et Oeters [7,8], Gou et al. [9] et Huber et al. [10]. Il a été établi que le taux de postcombustion (PCR) dans les gaz en sortie du convertisseur, défini comme le rapport de la concentration de dioxyde de carbone sur celles de CO et CO_2, augmente avec la hauteur de la lance de soufflage ou la quantité de ferrailles. D'autre part, une augmentation de la température et de la teneur en carbone du bain conduit à des valeurs du PCR plus petites.

Nous présentons dans cette thèse le développement de deux modèles distincts qui seront couplés à l'avenir. Le premier modèle concerne l'interaction hydrodynamique entre le jet gazeux et le bain de métal et plus particulièrement la prédiction de la cavité due à l'impact du jet gazeux. Ce modèle prend en compte les effets de compressibilité dus aux fortes vitesses du gaz. Il faut cependant remarquer que le gaz est traité comme incompressible au voisinage de la surface libre, car la compressibilité du gaz dans cette région est masquée par la diffusion numérique de l'interface entre le gaz (léger et compressible) et le liquide (lourd et incompressible). Cette approximation restreint l'éventail des configurations que notre modèle est capable de gérer. Tout d'abord, les calculs ont été effectués pour des configurations de type maquette froide avec deux

ou trois phases, dans lesquelles les vitesses du gaz sont subsoniques. La bibliographie fournit en effet une grande quantité de données expérimentales pour de tels systèmes, utilisables pour la validation du modèle. Contrairement aux précédentes études rapportées dans la littérature, notre modèle est également utilisé pour tester l'influence de plusieurs paramètres et/ou modèles, parmi lesquels les conditions aux limites d'entrée du jet, le schéma d'advection de la surface libre et le modèle de turbulence. Enfin, nous montrons un exemple d'application du m odèle à un j et d'oxygène à grande vitesse (dans le régime supersonique) impactant un bain d'acier liquide. Le second modèle décrit les phénomènes de transport de quantité de mouvement, de chaleur et de masse, et la réaction de postcombustion dans la phase gazeuse. La détermination du t aux de postcombustion et l'identification des régions où se produit cette réaction sont parmi les objectifs de ce modèle.

Chapter I Modèle mathématique

Dans le présent travail, nous considérerons une géométrie axisymétrique et utilisons une approche transitoire. Bien que les modèles de pénétration du jet et de postcombustion soient indépendants, ils décrivent tous les deux la dynamique du gaz au-dessus du bain métalliques. Les caractéristiques communes aux deux modèles sont présentées dans la première section de ce chapitre. Ensuite, nous décrivons les hypothèses, les équations et les conditions aux limites propres à chaque modèle. Toutes les simulations présentées dans cette étude ont été effectuées avec PHYSICA, un logiciel de CFD (Computational Fluid Dynamics) développé à l'Université de Greenwich [11].

I.1 Simulation de la dynamique de la phase gazeuse

Les régimes incompressible et compressible sont pris en compte dans le modèle. Les équations de conservation de la masse, de la quantité de mouvement et de l'énergie qui sont résolues sont données ci-dessous.

$$\frac{\partial \rho}{\partial t} + \frac{\partial (\rho u_i)}{\partial x_i} = 0 \qquad \textbf{Eq. 1}$$

$$\frac{\partial (\rho u_i)}{\partial t} + \frac{\partial}{\partial x_j}(\rho u_j u_i) = -\frac{\partial P}{\partial x_i} + \frac{\partial}{\partial x_i}\left[(\mu + \mu_t)\left(\frac{\partial u_i}{\partial x_j} + \frac{\partial u_j}{\partial x_i}\right)\right] + \rho g_i \qquad \textbf{Eq. 2}$$

$$\frac{\partial (\rho h)}{\partial t} + \frac{\partial}{\partial x_i}(\rho u_i h) = \frac{\partial}{\partial x_i}\left[\left(\frac{\lambda}{c_p} + \frac{\mu_t}{\sigma_T}\right)\frac{\partial h}{\partial x_i}\right] + \frac{\partial}{\partial x_i}\left[\lambda h \frac{\partial (1/c_p)}{\partial x_i}\right] \qquad \textbf{Eq. 3}$$

Dans les équations décrites ci-dessus, μ_t et σ_T sont la viscosité turbulente et le nombre de Prandtl turbulent de la chaleur. Dans l'équation de l'énergie, l'enthalpie a été choisie comme variable principale. Elle est reliée à la température par $h = c_p T + 0.5V^2$, avec le terme $0.5V^2$ inclus seulement si le régime est supersonique. Dans les cas compressibles, le système nécessite l'ajout de l'équation des gaz parfaits afin de prendre en compte la variation de densité avec la pression :

$$\rho = \frac{PW}{RT} \qquad \textbf{Eq. 4}$$

Avec W est la masse molaire du gaz.

La viscosité turbulente est calculée à partir du modèle de turbulence k-ε standard. Ce modèle de turbulence résout les équations de transport de deux variables additionnelles : l'énergie cinétique

turbulente (k) et son taux de dissipation (ε). Ces équations sont données par exemple dans [12]. La viscosité turbulente, dans cette approche, est :

$$\mu_t = \rho C_\mu \frac{k^2}{\varepsilon} \qquad \textbf{Eq. 5}$$

Avec la constante C_μ qui a pour valeur 0.09.

Des modifications doivent être apportées au modèle k-ε standard pour tenir compte des effets de compressibilité sur la turbulence lorsque nous simulons le cas d'un jet à forte vitesse. Un des effets les plus importants pour les jets supersoniques est une diminution du taux d'élargissement du jet avec la compressibilité. Plusieurs modèles correctifs ont été décrits dans la littérature tels que ceux d'Abdol-Hamid et al. [13] et d'Alam et al. [14] qui simulent le développement d'un jet supersonique pour différentes températures ambiantes. Ces modèles sont basés sur une modification du coefficient C_μ, qui n'est pas pris uniforme, mais qui est calculé en fonction des valeurs locales du gradient de la température de stagnation et du nombre de Mach turbulent. Dans cette étude, une approche similaire mais simplifiée a été utilisée. C_μ est pris uniforme dans tout le domaine de calcul, mais sa valeur est réduite par rapport à la valeur utilisée dans le cas incompressible. Des valeurs ajustées de C_μ ont été déterminées dans le manuscrit de thèse de B. Lebon [15] en comparant les résultats numériques avec les données expérimentales publiées par Sumi et al. [16] pour un jet compressible froid entrant dans une atmosphère chaude. Les valeurs ajustées de C_μ, déterminées pour différentes températures ambiantes, sont listées dans le Tableau 1. De ces valeurs, une corrélation est obtenue, où C_μ est calculé en fonction du rapport de l'enthalpie du gaz ambiant (h_{amb}) sur l'enthalpie du jet à la sortie de la lance (h_{jet}).

$$C_\mu = A \exp\left(-B \frac{h_{amb}}{h_{jet}}\right) \qquad \textbf{Eq. 6}$$

Avec A =0.081 et B = 0.14.

Ambient temperature (K)	C_μ
285	0.07
772	0.06
1002	0.05

Tableau 1: Valeurs du coefficient C_μ pour différentes temperatures ambiantes [15]. A la sortie de la tuyère, le jet a une température de 190 K et une vitesse de 450 m/s.

Enfin, certaines simulations présentées dans ce document ont été réalisées en utilisant un modèle k-ε hybride, connu sous le nom de modèle k-ε filtré. Ce modèle, qui a été proposé par Johanssen

et al. [17], a pour but de compenser partiellement les lacunes du modèle k-ε standard pour des écoulements instationnaires. Contrairement à l'approche statistique qui est à la base du modèle k-ε standard, les petits tourbillons turbulents sont modélisés alors que les grands tourbillons sont résolus numériquement. Le modèle k-ε filtré utilise des équations de transport de k et ε identiques à celles du modèle k-ε standard avec toutefois, une nouvelle expression de la viscosité turbulente:

$$\mu_t = \min\left[1, C_3 \Delta \frac{\varepsilon}{k^{3/2}}\right] \mu_{t,std} \qquad \textbf{Eq. 7}$$

Avec $\mu_{t,std}$ la viscosité turbulente définie dans le modèle k-ε standard, C_3 une constant comprise entre 0.61 et 2.3 (C_3=1 dans nos simulations) et Δ est la taille du filtre. Ce filtre permet de séparer les petits tourbillons qui seront modélisés des grands qui seront résolus. La taille minimum du filtre est donc limitée par le maillage et respecte la condition suivante :

$$\Delta \geq \max\left(\Delta r_{\min}, \Delta z_{\min}, \sqrt{(\Delta r \Delta z)_{\min}}\right) \qquad \textbf{Eq. 8}$$

Avec Δr_{min} et Δz_{min} les tailles minimales des cellules du maillage dans les directions radiale et axiale. Dans Eq. 7, nous pouvons voir que la viscosité turbulente aura une valeur inférieure à celle calculée par le modèle k-ε standard. La taille du filtre est constante dans toutes les cellules du domaine pour nos calculs.

I.2 Hypothèses et équations spécifiques du modèle d'un jet impactant une surface déformable

Ce modèle a pour but de calculer la forme de la surface libre d'un bain liquide déformée par l'impact d'un jet gazeux. C'est un modèle multiphasique qui décrit, en plus de la dynamique de l'interface gaz-liquide, l'écoulement du fluide et le transfert de chaleur dans des différentes phases (gazeuse et liquide). Il est possible de prendre en compte deux phases liquides dans le modèle afin de représenter la présence éventuelle d'une couche de liquide plus légère recouvrant le bain (laitier dans le convertisseur). Le système d'équations de transport décrit ci-dessus (Eq. 1 à Eq. 3) est résolu dans les phases gazeuse et liquide avec des propriétés physiques spécifiques pour chacune des phases. Rappelons que dans la phase liquide le fluide est considéré incompressible.

Une variante de la méthode VOF est utilisée pour suivre l'interface entre les phases gazeuse et liquide [18]. Le suivi de l'interface est fait via la résolution des équations de transport des fractions volumiques de phase, qui peuvent être écrites sous la forme générale suivante:

$$\frac{\partial \alpha}{\partial t} + u_i \frac{\partial \alpha}{\partial x_i} = 0 \qquad \textbf{Eq. 9}$$

Avec α la fraction volumique de phase.

Durant cette thèse, deux schémas différents ont été testés pour traiter le terme convectif de l'équation de transport de la fraction volumique α (terme gauche de Eq. 9): le traditionnel schéma explicite Donor-Acceptor (DA) [18] et une nouvelle méthode appelée Counter Diffusion Method (CDM). Dans le schéma DA, le flux convectif de α à travers la face de chaque cellule d'interface est calculée en définissant une cellule en tant que donneur d'une quantité de fluide et la cellule voisine comme accepteur de la même quantité de fluide et en considérant que l'interface dans une cellule est strictement parallèle à l'une des faces de la cellule. Le CDM, quant à lui, est un schéma implicite développé par Pericleous et al. [19] afin d'éviter la nécessité d'utiliser des petits pas de temps sur des maillages raffinés tout en préservant la finesse de l'interface. Avec cette méthode, le flux convectif de α est calculé en utilisant un schéma décentré de premier ordre avec un flux de correction (counter diffusion) qui est ensuite appliqué pour contrebalancer la diffusion numérique de l'interface due au schéma décentré. Ce flux correctif permet aux "gouttelettes" et aux "bulles" numériques de retourner respectivement dans le bain et dans la phase gazeuse. Ce flux par unité de surface est exprimée par:

$$F = C\left|\vec{u}.\vec{n}\right|(1-\alpha_A)\alpha_D \qquad \textbf{Eq. 10}$$

avec $\vec{u}$ et $\vec{n}$ la vitesse du fluide et la normale au centre de la face de la cellule. α_A et α_D sont les valeurs de α dans les cellules donneuses et accepteuses respectivement. C est un coefficient ajustable dépendant du problème. Plusieurs études, non publiées, réalisées par le groupe du Professeur K. Pericleous à l'Université de Greenwich, ont donné la gamme de valeurs de C suivante: $1 \leq C \leq 2{,}5$. L'équation ci-dessus du flux garantit la conservation de la masse sachant que la masse prise du "donneur" est la même que celle reçue par l'"accepteur".

Les effets de tension superficielle à la surface libre du bain sont pris en compte lors de la résolution des équations de Navier-Stokes, en ajoutant à ces équations un terme source supplémentaire dépendant de la valeur de la tension de surface et de la courbure de l'interface [20].

Le modèle développé est capable de prendre en compte à la fois des jets à faible (i.e. incompressible) et forte vitesse (i.e. compressible) impactant une surface liquide. Néanmoins, lors de la simulation d'un jet à forte vitesse, le modèle dans sa version actuelle, est utilisable uniquement dans les cas où la lance de soufflage est suffisamment loin du bain de sorte que le jet ait une vitesse subsonique près de la surface afin d'ignorer les effets de compressibilité dans cette région. Une telle condition est compatible avec les situations généralement rencontrées dans un convertisseur industriel. La raison principale de cette approximation vient du fait que dans la version originale de Physica, le champ de vitesse au voisinage de la surface libre est résolu en utilisant la conservation du volume plutôt que celle de la masse. Or, prendre en compte la compressibilité dans la phase gazeuse nécessite la résolution de l'équation de continuité exprimée sous forme de conservation de la masse (plutôt que sous forme de conservation du volume). La prise en compte précise de la compressibilité du gaz près de la surface libre est une tâche difficile. En effet, même la plus petite “contamination” de la phase gazeuse par le liquide (résultant par exemple de la diffusion numérique de la surface libre) rend l'algorithme compressible inexact. Ceci est dû au fait que les changements de densité dues à la composition de phase peuvent être beaucoup plus importants que ceux dus à la pression du gaz. En l’état actuel, notre modèle n'est pas en mesure de résoudre cette difficulté et des recherches supplémentaires sont nécessaires pour le faire. Dans le présent modèle, une approche zonale est utilisée [15]. Elle divise le domaine de calcul en deux régions délimitées par l'isoligne du nombre de Mach correspondant à une valeur de 0,3. Dans la première région (où Ma > 0,3), située en aval de la sortie de la buse de soufflage, les effets de compressibilité sont pleinement pris en compte en utilisant la conservation de la masse dans l'équation de continuité, tandis que dans la partie restante du domaine (où Ma ≤ 0,3), le gaz peut être considéré incompressible et l'équation de continuité est résolue sous sa forme de conservation du volume. Notons que la limite entre les deux régions n'est pas un paramètre d'entrée mais est déterminée dynamiquement par le modèle pendant le calcul.

La Figure 2 représente les conditions aux limites pour la simulation d’un jet gazeux impactant une surface déformable. L’intérieur de la lance n’est pas simulé. Une condition de non glissement avec des fonctions de parois standards est appliquée aux parois dont les températures sont imposées (1000 K pour les parois réfractaires et 313 K pour les parois de la lance). À la sortie du convertisseur, une pression constante est appliquée avec un gradient nul pour les autres

variables. Les conditions aux limites à la sortie de la lance sont des valeurs fixées pour la vitesse, la température, k et ε. Lorsque les vitesses sont supersoniques, la pression du gaz à la sortie de buse est également fixée. k et ε à la sortie de buse sont calculés comme suit:

$$k = \frac{3}{2}\left(I\,U_0\right)^2 \qquad \textbf{Eq. 11}$$

$$\varepsilon = C_\mu^{3/4}\,\frac{k^{3/2}}{\ell} \qquad \textbf{Eq. 12}$$

Avec I, l'intensité turbulente déterminée à partir de la corrélation empirique suivante $I = 0.16\,\mathrm{Re}^{-1/8}$ [21] et ℓ l'échelle de turbulence $\ell = 0.07\,D_n$.

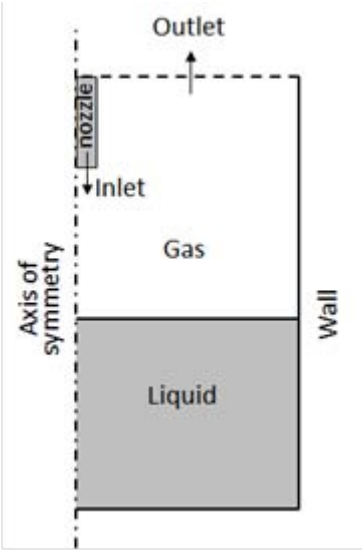

Figure 93: Conditions aux limites du modèle d'un jet impactant une surface deformable.

I.3 Hypothèses et équations spécifiques de la modélisation des transferts couplés dans la phase gazeuse

L'objectif de ce modèle est la description de la phase gazeuse réactive située au-dessus du bain de métal. On suppose que la surface du bain est fixe et qu'en dehors de la région d'impact du jet, il y a une émission d'un flux de CO résultant de la décarburation du métal liquide. La prise en compte du laitier (qui peut avoir une influence importante sur les interactions chimiques et thermiques entre le gaz et le métal) n'est pas faite dans le modèle actuel et sera abordée dans une étude future, de même que la présence de gouttelettes liquides provenant du bain et de particules solides en suspension dans la phase gazeuse. Les espèces chimiques décrites ici sont : CO, O_2 et CO. La seule réaction traitée par le modèle est l'oxydation du CO:

$CO + 1/2\,O_2 \rightarrow CO_2$

Pour la description de l'hydrodynamique de la phase gazeuse, nous employons le système d'équations données dans la section I.1 qui prend en compte le caractère compressible du gaz.

Simple Chemical Reaction Scheme (SCRS)

Le transport des espèces chimiques est traité en utilisant l'algorithme Simple Chemical Reaction Scheme [22], dans lequel sont résolues deux équations de transport, pour la fraction massique de CO et la fraction de mélange appelée f.

$$\frac{\partial(\rho x_{CO})}{\partial t}+\frac{\partial}{\partial x_i}(\rho u_i x_{CO})=\frac{\partial}{\partial x_i}\left[\Gamma\frac{\partial x_{CO}}{\partial x_i}\right]+R_{CO} \qquad \textbf{Eq. 13}$$

$$\frac{\partial(\rho f)}{\partial t}+\frac{\partial}{\partial x_i}(\rho u_i f)=\frac{\partial}{\partial x_i}\left[\Gamma\frac{\partial f}{\partial x_i}\right] \qquad \textbf{Eq. 14}$$

La fraction de mélange f dépend des fractions massiques de CO et de O_2 par la relation suivante:

$$f=\frac{1-str}{1+str}(str\, x_{CO}-x_{0_2}) \qquad \textbf{Eq. 15}$$

Avec str le rapport massique stœchiométrique pour la réaction de postcombustion (str = 16/28 = 0,571). Notons que l'équation de transport de f ne contient pas de terme source ce qui rend sa convergence numérique plus rapide. Le coefficient effectif de la diffusion de masse Γ (apparaissant dans les équations 13 et 14) est considéré le même pour toutes les espèces et est exprimé par la relation suivante:

$$\Gamma=\rho\,(D+D_t)=\frac{\lambda}{c_p\,L_e}+\frac{\mu_t}{\sigma_t} \qquad \textbf{Eq. 16}$$

avec L_e et σ_t le nombre de Lewis et le nombre de Prandtl turbulent (qui sont tous les deux égaux à 1). Lorsque C_p n'est pas constant dans tout le domaine, le terme diffusif se divise en deux termes : un terme standard de diffusion avec Γ et un terme additionnel respectant :

$$\frac{\partial}{\partial x_i}\left[\lambda\phi\frac{\partial(1/c_p)}{\partial x_i}\right] \text{ (avec } \phi=x_{CO} \text{ or } f\text{)} \qquad \textbf{Eq. 17}$$

Dans l'équation 13, R_{CO} est le taux de disparition de CO. En supposant que la vitesse de réaction est contrôlée par le mélange turbulent des espèces réactives, ce terme est obtenu en utilisant le modèle Eddy Break-Up (EBU) [24], par l'intermédiaire de l'expression suivante:

$$R_{CO}=-C_{EBU}\rho\min\left[x_{CO},\frac{x_{O_2}}{str}\right]\frac{\varepsilon}{k} \qquad \textbf{Eq. 18}$$

Avec C_{EBU} la constante du modèle Eddy Break-Up prise égale à 1 dans le présent modèle. L'approche actuelle est un cas limite et un modèle plus raffiné devrait prendre en compte, en

plus des effets de mélange dus à la turbulence, les effets cinétiques évalués en utilisant un terme d'Arrhenius.

Notons que, dans le cadre du modèle SCRS, la densité du gaz est calculée en utilisant la loi des gaz parfaits:

$$\rho = \frac{pW}{RT} \qquad \textbf{Eq. 19}$$

Avec W la masse molaire du mélange calculée comme:

$$\frac{1}{W} = \frac{x_{CO}}{W_{CO}} + \frac{x_{O_2}}{W_{O_2}} + \frac{x_{CO_2}}{W_{CO_2}} \qquad \textbf{Eq. 20}$$

Afin de représenter la pénétration d'oxygène dans le bain associée à la réaction de décarburation, un puits de masse est ajouté comme terme source supplémentaire à l'équation de continuité (Eq. 1) pour les mailles adjacentes à la cavité créée par l'impact du jet. Ce terme source est défini de la manière suivante:

$$\Delta R_{mass} = -\dot{m}_{O_2} COEF\, x_{O_2,i} \frac{A_i}{V_i} \qquad \textbf{Eq. 21}$$

avec $\dot{m}_{O_2}$ la densité de flux massique de l'oxygène entrant dans le bain. A_i et V_i sont l'aire de la face de la cellule en contact avec le métal et le volume de cette cellule. Le paramètre COEF est défini comme $COEF = \sum_j A_j \Big/ \sum_j A_j x_{O_2,j}$ et est utilisé pour éviter de prendre plus de masse que la masse d'oxygène présente dans la cellule. Lorsque la masse prise est un mélange de O_2, CO et CO_2, un terme source est appliqué à l'équation de x_{CO} et de f afin de remettre dans la phase gazeuse les masses de CO et CO_2 prises à tort.

Transfert de chaleur

Le modèle est basé sur la résolution de l'équation de transport d'énergie donnée dans la section I.1 pour les transferts de chaleur, mais avec deux modifications. Tout d'abord, l'enthalpie est maintenant définie par l'expression suivante $h = c_p T + x_{CO} H_{react} + 0.5V^2$, avec H_{react} l'enthalpie de la réaction de postcombustion (H_{react} = -10,1 MJ/kg). Ensuite, le transport d'énergie par rayonnement est pris en compte par l'ajout dans le terme source de l'équation 3 du t erme S_h représentant la puissance rayonnée à partir du gaz:

$$S_h = R_d - E \qquad \textbf{Eq. 22}$$

avec $E=\sigma T^4$ l'émissivité d'un corps noir et R_d la radiosité, qui représente la moyenne des flux rayonnants entrants et sortants intégrés sur toutes les directions du solide.

R_d est obtenue en résolvant l'équation de transport suivante:

$$\frac{\partial}{\partial x_i}\left[\frac{4}{3(a+s)}\frac{\partial R_d}{\partial x_i}\right] = -a\,(E - R_d) \qquad \textbf{Eq. 23}$$

Dans cette équation, a est le coefficient d'absorption et s le coefficient de diffusion. Les valeurs de ces coefficients dans la phase gazeuse du convertisseur, qui peuvent dépendre de la composition et de la température du gaz ainsi que de la présence de gouttelettes et de particules solides en suspension, ne sont pas connues à l'heure actuelle. Les simulations présentées dans ce document ont été réalisées avec des valeurs des deux coefficients de 0,3.

La Figure 3 montre les conditions aux limites associées au modèle. La surface du bain déformée est maintenu fixe durant la simulation. L'émission de CO à la surface du bain est modélisée par une condition à la limite de type flux imposé. Quant aux phénomènes hydrodynamiques et thermiques, nous utilisons des conditions aux limites similaires à celles considérées dans le modèle du j et impactant une surface liquide tout en considérant en plus les flux radiatifs à chaque paroi.

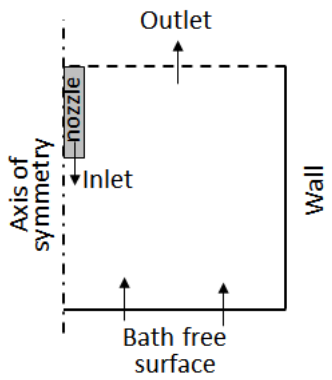

Figure 94: Conditions aux limites du modèle de postcombustion.

Chapter II Aspects expérimentaux

Dans ce chapitre, nous présentons brièvement les différents cas simulés pour la validation de nos modèles.

II.1 Maquette froide de Qian

Qian et al. [24] ont effectué des expériences dans une maquette froide consistant à visualiser la forme de la cavité créée lors de l'impact d'un jet d'air sur un bain d'eau. Les expériences ont été faites avec une ou plusieurs (huile de maïs-eau et kérosène-eau) couches de liquides. Leur appareillage se compose d'un conteneur de section carré contenant un second conteneur cylindrique en verre ayant un diamètre de 29,8 cm et une hauteur de 20,3 cm comme nous pouvons le voir sur la Figure 4. La position de l'interface a été mesurée par une sonde electrorésistive et les images ont été enregistrées grâce à une caméra rapide. Le débit du gaz était compris entre 1.43×10^{-4} et 3.57×10^{-3} m^3/s avec une hauteur de lance variant entre 1,5 et 21 cm. De plus, trois lances de diamètres 0,25, 1,2 et 2,3 cm ont été utilisées.

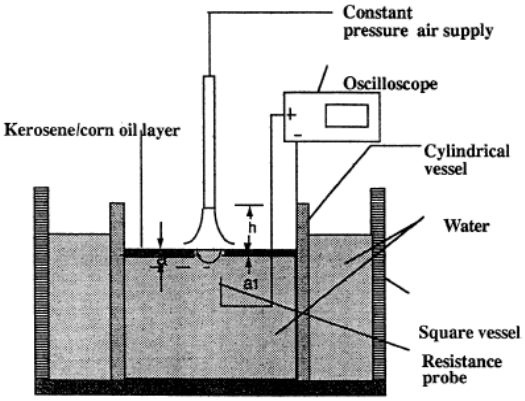

Figure 95: Maquette expérimentale de Qian et al. [23].

II.2 Expérience de Kaizawa

Kaizawa et al. [25] ont mené des expériences dans un tube cylindrique (Figure 5) afin de mieux comprendre la réaction entre un jet de monoxyde de carbone et un jet d'oxygène. Le tube a un diamètre intérieur de 30 cm et une hauteur de 140 cm. Les réactifs O_2 et CO ont été introduits grâce à deux lances de soufflage (de respectivement 0,4 cm et 1 cm de diamètre) situées respectivement en haut et en bas du tube de réaction. Dans cette expérience, les profils radiaux de la composition du gaz ont été mesurés en utilisant une sonde de prélèvement de gaz

introduite dans la cuve à travers des trous placés à 31,4 et 54,4 cm de la pointe de la lance d'oxygène.

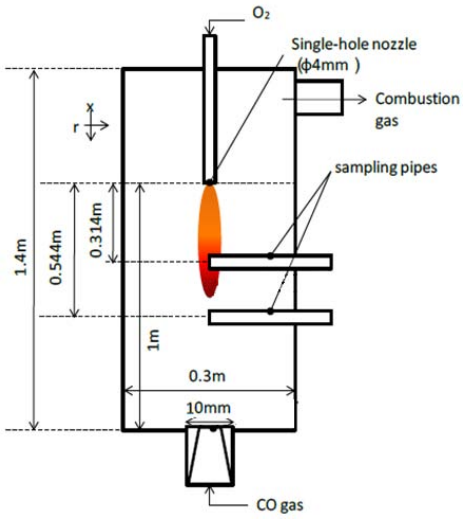

Figure 96: Schéma descriptif de l'expérience menée par Kaizawa et al. [25].

II.3 Convertisseur pilote d'ArcelorMittal

Dans les années quatre-vingt, ArcelorMittal a mené des expériences dans un convertisseur de taille pilote afin d'étudier l'influence de différents paramètres sur le taux de postcombustion. Ces expériences ont été réalisées dans un réacteur axisymétrique de 380 cm de haut et de 140 cm de diamètre interne contenant un bain d'acier liquide d'environ 6 tonnes (Figure 6). La lance de soufflage, placée verticalement au-dessus du bain à des hauteurs variant entre 100 et 220 cm, a été équipée d'une buse à trou unique de 2,2 cm de diamètre. Au cours de ces essais, des mesures de la température du gaz dans la phase gazeuse ont été aussi effectuées.

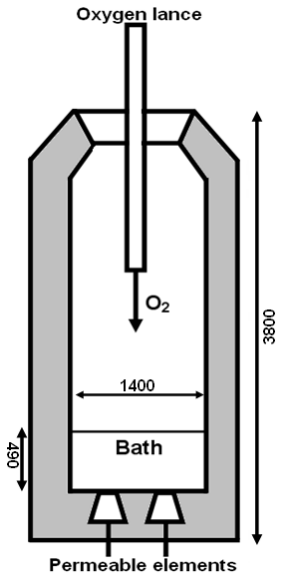

Figure 97: Schéma du convertisseur pilote d'ArcelorMittal (dimensions en mm).

Chapter III Résultats du modèle d'un jet impactant une surface déformable

Les résultats présentés dans cette section sont divisées en deux parties. Tout d'abord, les calculs sont effectués pour des jets incompressibles à faible vitesse en utilisant la géométrie et les conditions expérimentales de la maquette froide de Qian. Une comparaison entre les prédictions de notre modèle et les données obtenues par Qian (pour des systèmes à 2 et 3 phases) est présentée et l'effet de différents paramètres et/ou méthodes de modélisation est discuté. La seconde partie, quant à elle, présente des résultats pour un jet compressible à forte vitesse en utilisant la géométrie et les conditions expérimentales du convertisseur pilote d'ArcelorMittal.

III.1 Jet incompressible à faible vitesse

III.1.1 Système à deux phases

Le modèle est utilisé pour simuler une expérience de Qian et al. [24] réalisée avec les conditions suivantes: diamètre de lance de 1,2 cm, distance entre la lance et la surface libre du bain de 5 cm et vitesse du gaz à la sortie de buse de 16,2 m/s. Les propriétés physiques des deux fluides, l'air et l'eau, sont données dans le Tableau 2.

	ρ (kg.m^{-3})	μ (Pa.s^{-1})	$\sigma_{liquide/air}$ (mN.m^{-1})
Eau	1000	10^{-3}	72.8
Huile de maïs	860	$40x10^{-3}$	34.1
Kérosène	810	$1.2x10^{-3}$	25
Métal liquide	6940	$5x10^{-3}$	1540
Air	Eq. 4	$1.9x10^{-5}$	-
Oxygène	Eq. 4	$1.9x10^{-5}$	-

Tableau 2 : Propriétés physiques des différents fluides utilisés dans les simulations.

III.1.1.2 Influence du maillage

Les profils moyennés dans le temps de la cavité prédite par le modèle sont représentés sur la Figure 7 pour quatre maillages différents (2643, 5280, 10899 et 14277 cellules). Notons que

nous utilisons un maillage irrégulier, localement raffiné près de la surface libre du bain. Les résultats présentés ici ont été obtenus en utilisant le schéma donor-acceptor pour le modèle VOF. Le raffinement du maillage ne change que légèrement la forme de la cavité. Quant aux dimensions, nous pouvons voir que la cavité est sensiblement plus large pour les deux premiers maillages et que la profondeur a tendance à augmenter avec le nombre de cellules. D'après les résultats présentés sur la Figure 7, on peut conclure qu'un maillage relativement grossier (de l'ordre de 10000 cellules) est suffisant pour minimiser l'influence du maillage sur les résultats obtenus.

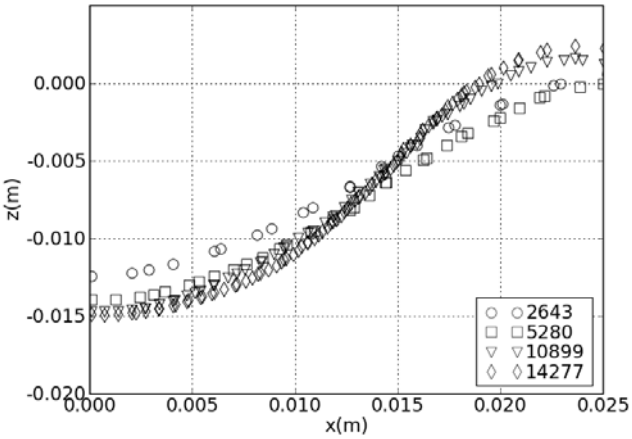

Figure 98: Interface moyennée dans le temps pour différentes tailles de maillage.

III.1.1.3 Influence des paramètres à la sortie du jet

Les conditions aux limites imposées à la sortie de la buse, présentées dans la section I.2, sont basées sur l'hypothèse selon laquelle les distributions de tous les paramètres du jet dans la section de sortie sont uniformes. Ci-dessous, nous testons un autre type de conditions aux limites basé sur des distributions non-uniformes (à priori plus réaliste). Pour ce dernier cas, nous considérons que le flux de gaz dans la lance est établi et donc que le profil radial de la vitesse obéit au profil analytique de vitesse en loi de puissance. Cependant, vu que les profils des variables de turbulence k et ε sont inconnus, ils ont été calculés en utilisant un modèle séparé en 2D axisymétrique traitant de l'écoulement du gaz à l'intérieur d'une lance de 60 cm de long avec des parois droites. Les Figure 8 et Figure 9 montrent les profils radiaux de k et ε calculés à la sortie de la buse et les courbes de tendance polynomiales utilisées pour représenter ces données. Les polynômes qui ont été utilisés, en plus du profil de vitesse en loi de puissance, comme conditions aux limites dans le modèle d'impact d'un jet sur une surface déformable, sont de la forme :

$$k = -1.1046 \cdot 10^{13}\left(\frac{r}{R_n}\right)^3 + 2.26 \cdot 10^{9}\left(\frac{r}{R_n}\right)^2 + 5.662 \cdot 10^{3}\left(\frac{r}{R_n}\right) + 1.48 \qquad \textbf{Eq. 24}$$

$$\varepsilon = 6.634 \cdot 10^{37}\left(\frac{r}{R_n}\right)^7 - 7.281 \cdot 10^{33}\left(\frac{r}{R_n}\right)^6 + 3.158 \cdot 10^{29}\left(\frac{r}{R_n}\right)^5 - 6.852 \cdot 10^{24}\left(\frac{r}{R_n}\right)^4 + 7.778 \cdot 10^{19}\left(\frac{r}{R_n}\right)^3 - 4.361 \cdot 10^{14}\left(\frac{r}{R_n}\right)^2 + 1.022 \cdot 10^{9}\left(\frac{r}{R_n}\right) \qquad \textbf{Eq. 25}$$

avec R_n le rayon de sortie de la buse.

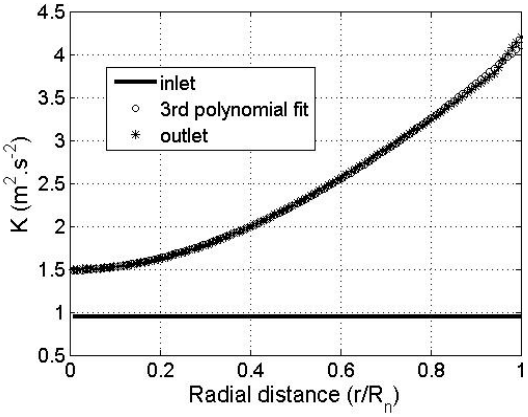

Figure 99: Energie cinétique turbulente à l'entrée et à la sortie de la lance.

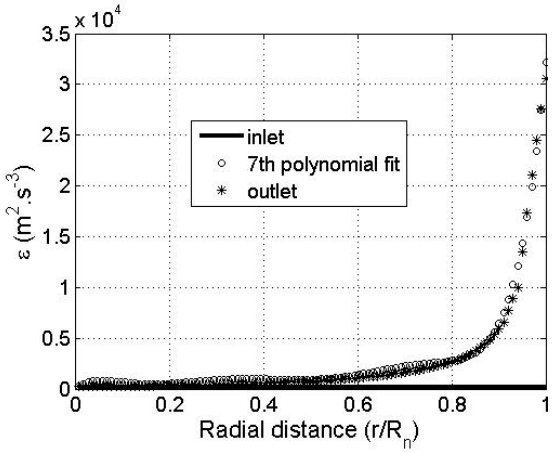

Figure 100: Dissipation de l'énergie cinétique turbulente à l'entré et à la sortie de la lance.

La déformation de la surface libre du bain sous l'impact du jet, prédite en utilisant des profils uniformes et non-uniformes des paramètres à la sortie du jet, est représentée sur la Figure 10. Le schéma donor-acceptor a été utilisé pour le modèle VOF. Comme on peut le constater, la largeur de la cavité est presque identique dans les deux cas. En revanche, la cavité est plus profonde quand elle est calculée avec des profils non-uniformes. En effet, la vitesse axiale du jet à la surface du bain est plus élevée pour le cas des profils non-uniformes comme le montre la Figure 11. Une plus grande vitesse signifie naturellement une plus grande force d'impact du jet et par conséquent une cavité plus profonde.

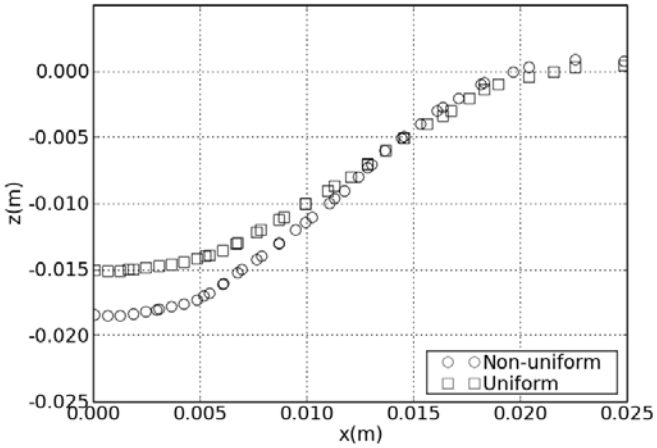

Figure 101: Interface moyennée dans le temps pour différents profils de u, k et ε.

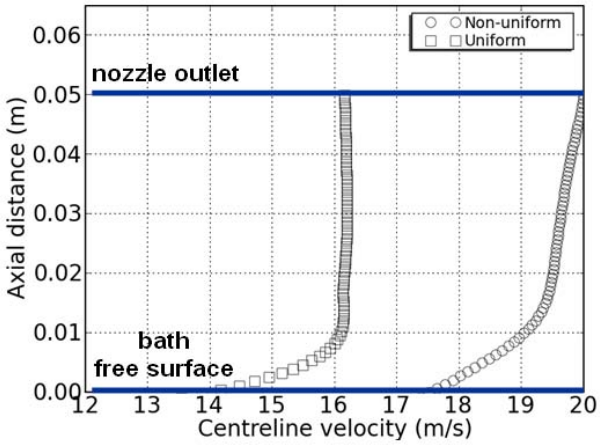

Figure 102: Vitesse à l'axe de symmétrie moyennée dans le temps pour différents profils de u, k et ε.

III.1.1.4 Influence du schéma VOF

Dans cette section, deux schémas VOF différents (donor-acceptor et counter diffusion method) sont comparés pour le calcul de la déformation de la surface libre du bain. La Figure 12 montre la cavité moyennée dans le temps donnée par les deux méthodes. Puisque le CDM repose sur un coefficient C ajustable, nous avons testé une gamme de valeurs de ce co efficient. Les dimensions de la cavité prédites se sont révélées ne pas être très sensibles à l a valeur du coefficient dans l'intervalle 1 <C <2,5. Lorsque nous comparons les deux schémas CDM et DA, il peut être vu que les résultats moyennés dans le temps sont assez semblables. Toutefois, il a été constaté que le comportement dynamique de l'interface est sensiblement différent (cf. Figure 13) avec une grande fragmentation d'interface lorsque nous utilisons le schéma DA. Le volume perdu dans la fragmentation peut expliquer les différences de dimensions de la cavité calculée.

Enfin, il convient de mentionner que les résultats obtenues avec le schéma CDM, présentés ici, ont été obtenus avec un pas de temps beaucoup plus petit (environ dix fois moins) que celui requis par le calcul effectué avec le schéma DA, ce qui signifie que le temps total de simulation est considérablement réduit. Cela rend l'utilisation du CDM très attractive.

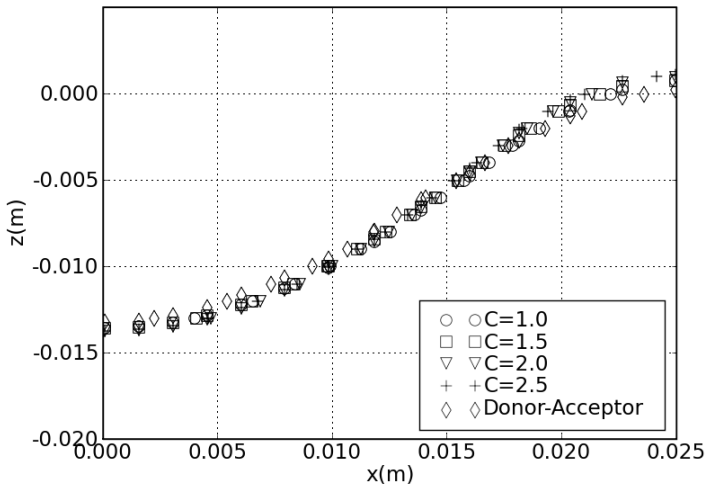

Figure 103: Interface moyennée dans le temps pour les schémas Donor-Acceptor et Counter Diffusion Method (plusieurs valeurs du coefficient C sont testées).

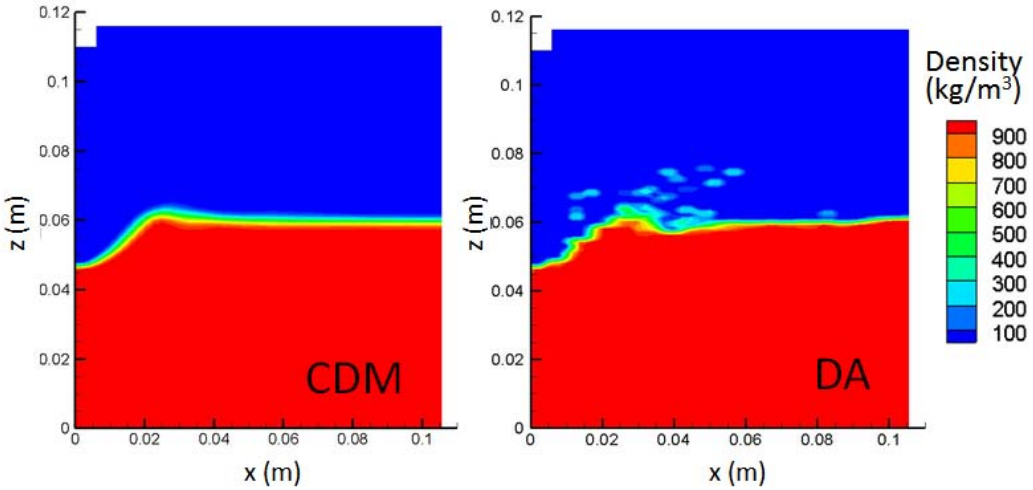

Figure 104: Interface instatanée pour les schemas CDM (gauche) et DA (droite).

III.1.1.5 Influence du modèle de turbulence

Les prédictions obtenues à partir des modèles de turbulence k-ε standard et filtré ont été comparées. Comme décrit précédemment, le modèle k-ε filtré fait intervenir une taille de filtre réglable. Différentes valeurs de la taille du filtre ont été testées pour vérifier leur influence sur la prédiction des dimensions de la cavité. Il faut noter que la taille du filtre ne dépend pas de la taille des cellules et est uniforme sur tout le domaine de calcul. Ces simulations ont été réalisées

avec le schéma CDM. Une comparaison des profils de cavités moyennés dans le temps pour les divers cas considérés, est présentée sur la Figure 14.

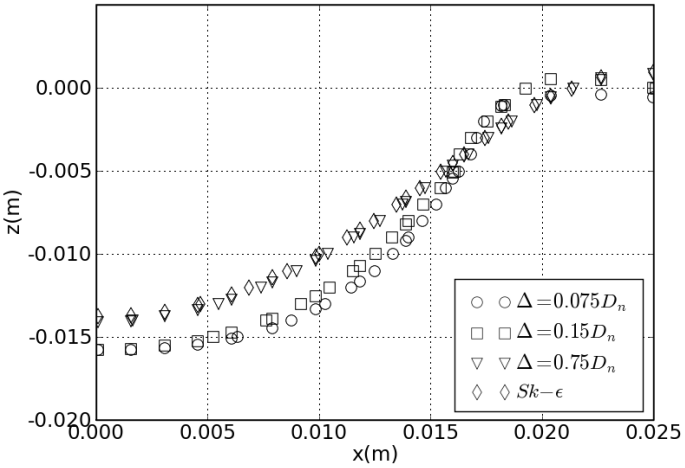

Figure 105: Interface moyennée dans le temps pour le k-ε standard et le k-ε filtré.

Les profils de cavités calculées ne sont que peu affectés par le modèle de turbulence employé. Dans l'ensemble, les résultats obtenus avec les deux modèles de turbulence en termes de forme et de dimensions de la cavité sont relativement similaires avec des écarts d'environ ± 15%. Il est observé que la pénétration du jet augmente lorsque la taille du filtre diminue. En effet, une diminution de la taille du filtre réduit la viscosité turbulente et entraine une augmentation de la vitesse axiale du jet et par conséquent augmente la profondeur de la cavité. Notons que la cavité calculée avec la plus grande taille de filtre (0,75 D_n) est presque identique à celle obtenue avec le modèle k-ε standard. Ceci est dû à la construction du modèle filtré, qui est fait de telle manière que le modèle repasse au modèle k-ε standard si nous utilisons une grande taille de filtre (opérateur "min" dans Eq. 7).

III.1.1.6 Comparaison aux données de Qian

La Figure 15 montre une comparaison entre les prédictions de notre modèle et les mesures de Qian et al. [24]. Pour cette comparaison, différentes simulations ont été réalisées en utilisant diverses combinaisons de paramètres (conditions aux limites d'entrée) et divers modèles (VOF et modèle de turbulence). Les résultats numériques présentés sur la Figure 15 sont ceux présentant le meilleur accord avec les données expérimentales. Ils ont été obtenus en utilisant le schéma CDM et le modèle k-ε standard et en supposant des distributions uniformes des paramètres du jet à la sortie de la buse. Il convient de souligner que toutes les combinaisons possibles de paramètres et de modèles n'ont pas été testées. Par conséquent, il n'est pas possible de prétendre que chacun des paramètres/modèles retenus est individuellement le meilleur. Il est

probable que le jeu "optimal" de paramètres déterminé ici donne lieu à certaines compensations d'erreurs. Notons que toutes les simulations présentées dans le reste de document seront effectuées en utilisant cet ensemble de paramètres.

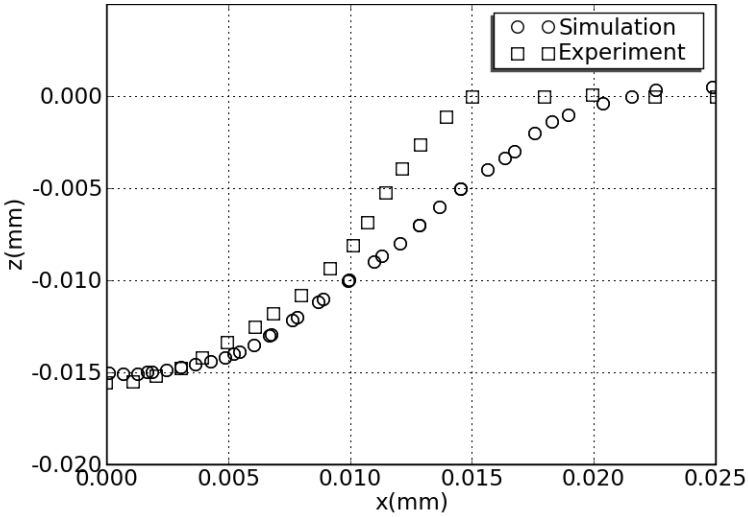

Figure 106: Comparaison des interfaces moyennées dans le temps calculée et obtenue expérimentalement par Qian et al. [23].

L'accord entre le modèle et les mesures est assez satisfaisant. Comme on peut le voir sur la Figure 15, la profondeur de la cavité est très bien prédite par le modèle, mais sa largeur est surestimée (d'environ 24%). Notons que, en terme de volume de la cavité, la différence est plus prononcée avec un écart d'environ 60%. Il semble certain que la surestimation de la largeur de la cavité prédite par le modèle est liée à une faiblesse bien connue du modèle k-ε standard. En effet, ce modèle est connu pour surestimer l'élargissement des jets axisymétriques ce qui contribue à élargir la cavité à la surface du bain. Plusieurs corrections apportées au modèle k-ε standard (cf. e.g. Launder [26]) ont été proposées dans la littérature afin d'améliorer la prédiction de jets ronds. Ces corrections n'ont pas été testées dans cette étude et ce point devrait être abordé dans un travail futur.

III.1.2 Système à trois phases

Qian et al. [24] ont effectué des expériences avec un bain à deux couches pour simuler la présence du laitier recouvrant le bain d'acier dans un convertisseur réel. Dans ces expériences, le laitier a été représenté à l'aide de kérosène ou d'huile de maïs. Les propriétés physiques des trois liquides utilisés dans ces expériences sont résumées dans le Tableau 2. Notons que le kérosène et l'huile de maïs ont des valeurs de viscosité très différentes (1,2 et 40 fois la viscosité de l'eau). L'épaisseur de la couche de kérosène ou d'huile de maïs est fixée à 0,8 cm. La distance entre la

sortie de buse (de 1,2 cm de diamètre) et la surface libre du fluide de couverture est de 3 cm. Le maillage utilisé pour simuler ces expériences contient 3195 cellules.

Les déformations des trois interfaces du système ont été calculées par la méthode VOF à l'aide de deux marqueurs (α et β). En utilisant ces deux paramètres, les propriétés du fluide (densité, viscosité) dans chaque cellule du maillage ont été déterminées par une moyenne volumique des propriétés des différentes phases présentes dans cette cellule de la manière suivante :

$$\phi = \alpha\,\phi_{water} + (1-\alpha)\beta\,\phi_{\ker osene/oil} + (1-\alpha)(1-\beta)\,\phi_{air} \qquad \textbf{Eq. 26}$$

Le marqueur β a été calculé en utilisant le schéma Counter Diffusion Method alors que le marqueur α a été calculé avec le schéma Donor-Acceptor. Dû aux limites du code que nous utilisons, seule la tension superficielle entre l'air et le second liquide recouvrant l'eau a été prise en compte.

<u>Kérosène comme second liquide</u>

Les Figure 16 et Figure 17 montrent une comparaison des profils moyennés dans le temps, calculés et mesurés dans le cas du kérosène utilisé comme second liquide, pour des vitesses de sortie du gaz de 6,4 et 7,6 m/s. Les régions non hachurées sur la Figure 17 correspondent à des régions où les trois phases sont présentes.

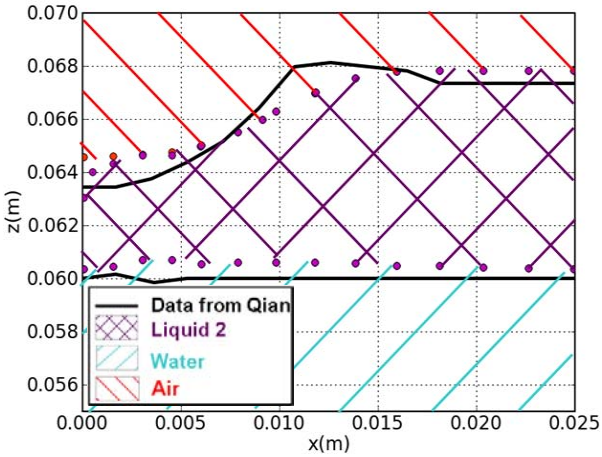

Figure 107: Interfaces moyennées dans le temps pour le système air-kérozène-eau (avec une vitesse du jet de 6.4 m/s).

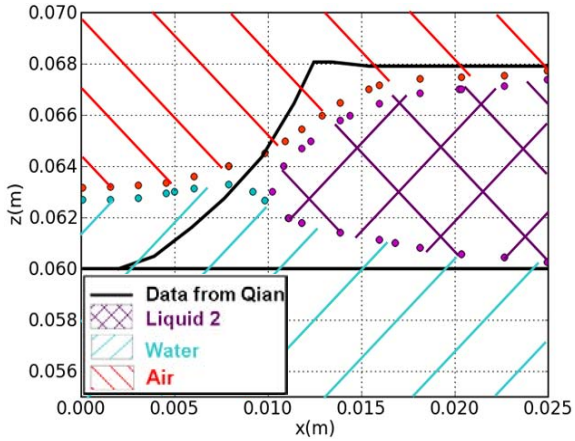

Figure 108: Interfaces moyennées dans le temps pour le système air-kérozène-eau (avec une vitesse du jet de 7.6 m/s).

Evidemment, plus la vitesse du gaz est grande, plus la pénétration du jet dans le bain est importante. Nous pouvons voir sur la Figure 16 que les résultats expérimentaux et ceux de la simulation sont très proches. L'interface eau-kérosène, peu perturbée, est parfaitement prédite par le modèle, tandis que l'interface air-kérosène est prédite avec une précision inférieure à 2 mm. Pour la plus grande vitesse de gaz (7,6 m/s), les résultats numériques sont moins précis. La pénétration du jet dans l'expérience est supérieure à celle calculée. De plus, dans les résultats expérimentaux, l'eau est directement en contact avec le jet d'air dans une région étroite près de l'axe de symétrie. Sur les résultats de la simulation, on peut remarquer que le niveau de l'eau est plus élevé près de l'axe de symétrie. Ce phénomène peut être attribué à l'écoulement dans la couche de kérosène induit par l'action du jet, qui entraine à son tour un mouvement de l'eau. Ce phénomène de surélévation n'est pas observé dans l'expérience, ce qui peut être en partie lié au fait que notre simulation ne tient pas compte de la tension superficielle entre l'eau et le kérosène.

<u>Huile de maïs comme second liquide</u>

Une comparaison des interfaces moyennées dans le temps, obtenues numériquement et expérimentalement, dans le cas de l'huile de maïs comme second liquide, pour des vitesses du gaz de 4,4 et 7,1 m/s est représentée sur les Figure 18 et Figure 19. Dans l'ensemble, les résultats du modèle montrent un accord satisfaisant (précision inférieure à 2 mm) par rapport aux données expérimentales. Cet accord est un peu mieux pour le cas avec la plus faible vitesse.

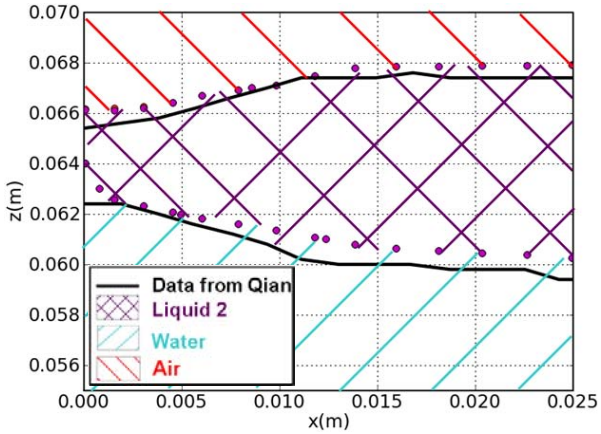

Figure 109: Interfaces moyennées dans le temps pour le système air-huile de maïs-eau (avec une vitesse du jet de 4.4 m/s).

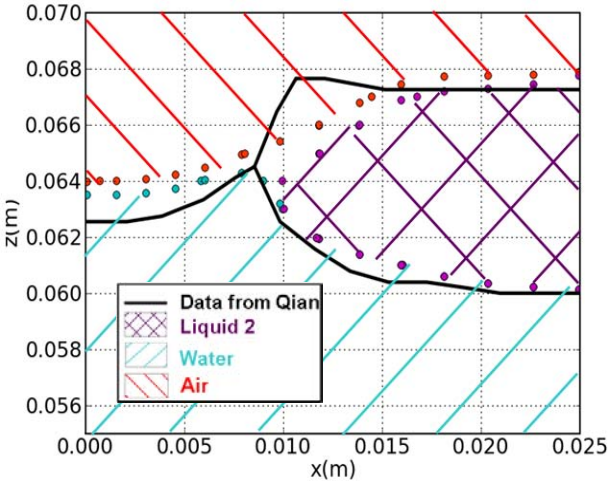

Figure 110: Interfaces moyennées dans le temps pour le système air-huile de maïs-eau (avec une vitesse du jet de 4.4 m/s).

Sur la Figure 18, le niveau de l'eau près de l'axe de symétrie est supérieur d'environ 2 mm au niveau initial. Il est intéressant de noter que l'eau est plus surélevée que précédemment avec le kérosène comme second liquide. Ceci est dû à la viscosité plus élevée de l'huile de maïs. En effet, la viscosité élevée de l'huile de maïs augmente la transmission de la force de cisaillement à l'interface entre l'huile et eau, qui est responsable de cette surélévation de l'eau. Lors de l'augmentation de la vitesse du gaz de 4,4 à 7,1 m/s, la surélévation de l'eau est encore plus importante et l'eau est maintenant en contact direct avec l'air, à partir de l'axe de symétrie jusqu'à un rayon d'environ 8 mm (Figure 19). L'huile est poussée latéralement en dehors de la région d'impact du jet. En effet, plus la vitesse du gaz est grande, plus la cavité est profonde et plus la force de cisaillement transmise à l'interface huile/eau est grande.

III.2 Jet compressible à forte vitesse

Le modèle estutilisé dans cette section pour simuler la déformation d'un bain d'acier liquide sous l'effet d'un jet supersonique d'oxygène dans le convertisseur pilote décrit dans la section II.3. La lance est située à 1 m au-dessus du bain d'acier liquide qui a une profondeur de 0,5 m. La buse est adaptée pour que la pression du jet à la sortie soit égale à la pression ambiante. La température de l'oxygène en sortie de buse est fixée à 203 K. Des simulations sont effectuées sur un maillage de 5457 cellules pour trois valeurs différentes de la vitesse du jet à la sortie de buse. Ces vitesses sont de 378, 500 et 750 m/s (correspondant respectivement à un nombre de Mach de 1,5, 1,9 et 2,9). Les propriétés physiques de l'oxygène et de l'acier liquide sont énumérées dans le Tableau 2.

La déformation de la surface libre du bain peut être vue sur les distributions moyennées dans le temps de la densité, qui sont tracées en plus des lignes de courant dans la phase gazeuse pour les différents cas simulés, sur la Figure 20. Les lignes en trait épais sur la Figure 20 représentent la frontière qui sépare la région intérieure du jet où les effets compressibles sont pris en compte (Ma > 0,3) de la région extérieure où les fluides peuvent être traités comme incompressible (Ma < 0,3). Cette limite est calculée par le modèle et est la base de l'approche zonale employée dans nos calculs. Notons que, pour toutes les conditions de ces simulations, le gaz peut être considéré comme incompressible près de la surface du bain. Une comparaison des profils moyennés dans le temps calculés pour les différentes vitesses de jet est présentée sur la Figure 21, où nous pouvons voir, comme prévu, que la taille de la cavité (en particulier sa profondeur) augmente avec la vitesse du jet. L'augmentation de la vitesse d'un facteur d'environ 2 conduit à une augmentation de la profondeur de la cavité d'un facteur d'environ 3. En sus, la forme de la cavité varie d'une cavité peu profonde pour une faible vitesse (378 m/s) à une cavité profonde à grande vitesse (750 m/s). Plus précisément, le rapport d'aspect de la cavité, défini comme le rapport de la demi-largeur sur la profondeur de la cavité, est réduit de près d'un facteur 2 lorsque la vitesse varie de 378 à 750 m/s.

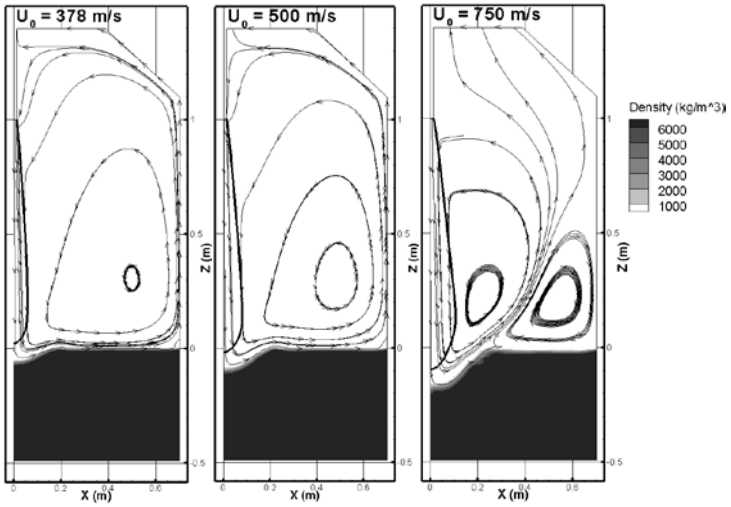

Figure 111: Distributions instatanées (après 2.5 s d'écoulement) des lignes de courant dans la phase gazeuse et de la densité calculée pour différentes vitesses d'entrée du jet. La ligne noire en trait plein représente l'isoligne où le nombre de Mach vaut 0.3.

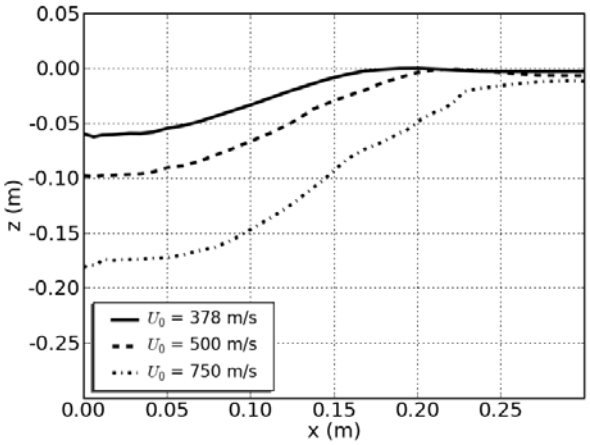

Figure 112: Comparaison des interfaces moyennées dans le temps entre les différentes vitesses d'entrée du jet.

Le Tableau 3 montre une comparaison entre les profondeurs de la cavité calculées avec notre modèle et celles obtenues en utilisant la corrélation de Koria et Lange [27]. Cette corrélation, donnée ci-dessous, a été élaborée à partir d'une étude expérimentale d'une cavité résultante de l'impact d'un jet sur un bain d'acier liquide.

$$\frac{h_c}{h_n} = 4.469\left[\frac{0.7904.10^5}{\rho_\ell g}\frac{D_n^2}{h_n^3}P_{amb}\left(1.27\frac{P_0}{P_{amb}}-1\right)\cos\alpha\right]^{0.66} \qquad \textbf{Eq. 27}$$

Dans cette relation, h_c est la profondeur de la cavité, h_n la distance entre la lance et le bain, ρ_l la densité de l'acier, D_n le diamètre de la buse de la lance, P_{amb} la pression ambiante, P_0 la pression d'alimentation en oxygène et α l'angle d'inclinaison de la buse. Notons que la corrélation de Koria et Lange fournit la valeur maximale de la profondeur tandis que les résultats de notre

modèle indiqués dans le Tableau 3 donnent une profondeur moyennée dans le temps. Dans l'ensemble, les résultats de la présente étude sont en accord avec les valeurs calculées par la corrélation de Koria et Lange. Il faut cependant noter que la différence entre les deux ensembles de données augmente avec la vitesse du jet. Une telle tendance peut s'expliquer par le fait que l'amplitude des oscillations de la profondeur, et donc la divergence entre les valeurs moyennées dans le temps et le maximum de la profondeur, augmentent avec la vitesse du jet.

U_0 (m/s)	Profondeur moyennée prédite par notre modèle	Profondeur maximale calculée avec la corrélation de Koria and Lange [27]
378	6.2 cm	6.6 cm
500	9.8 cm	11.3 cm
750	18 cm	21.6 cm

Tableau 3: Comparaison entre les profondeurs moyennées prédites par notre modèle et les profondeurs maxiamles obtenues avec la corrélation de Korai et Lange [27] pour différentes entrées du jet.

Dans la phase gazeuse, une seule boucle de recirculation est observée pour des vitesses de 378 et 500 m/s alors que dans le cas de la plus grande vitesse (750 m/s), la Figure 20 nous montre la présence de deux boucles de recirculation. La première boucle, qui occupe la majeure partie de la phase gazeuse, est induite par l'écoulement du jet d'oxygène.La seconde, située au-dessus du bain à proximité de la paroi latérale, est de plus petite taille et est le résultat de la déviation de l'écoulement du j et d'oxygène issu de la cavité en raison de la profondeur importante de la cavité.

Chapter IV Résultats de la modélisation des transferts couplés dans la phase gazeuse

IV.1 Simulation de l'expérience de Kaizawa

Les conditions expérimentales simulées avec notre modèle sont les suivantes: vitesse d'entrée de O_2 29,2 m/s, vitesse d'entrée de CO 14 m/s, températures des jets de O_2 et de CO 300 K. Les parois latérales du tube de réaction sont considérées adiabatiques. Dans la simulation, le gaz a été considéré comme incompressible du fait des faibles vitesses. Le maillage du tube de réaction, contenant 20 cellules dans la direction radiale et 104 dans la direction axiale, a été raffiné à proximité de l'axe de symétrie et des frontières d'entrée et de sortie.

Les distributions de vitesse et de température calculées dans le tube de réaction sont représentées sur la Figure 22. Nous pouvons voir sur la distribution de vitesse que la majeure partie du domaine est assez stagnante avec une vitesse inférieure à 2 m/s. Les deux jets se croisent à mi-chemin dans le tube et il n'y a que très peu d'interpénétration. Les températures sont du même ordre de grandeur à l'intérieur du tube sauf à l'entrée des jets où elles restent faibles (~300 K) et autour du jet d'oxygène où la majeure partie de la réaction a lieu. En effet, il découle des résultats présentés ci-dessous que CO réagit avec l'oxygène principalement au niveau des frontières du jet d'oxygène. Nous pouvons, par conséquent, remarquer une augmentation de la température dans cette région due à la formation de CO_2. Il faut également noter que la valeur maximale de la température se situe approximativement à mi-hauteur du tube, à proximité de l'axe de symétrie.

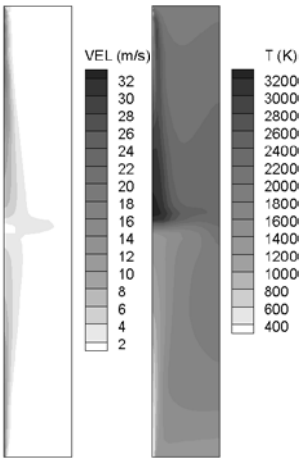

Figure 113: Distributions de la vitesse et de la temperature dans un tube de reaction.

Les distributions des fractions molaires de O_2, CO et CO_2 calculées à l'intérieur du tube de réaction sont présentées sur la Figure 23. Comme attendu, les fractions de O_2 et CO diminuent en s'éloignant de leurs points d'injection respectifs. La réaction de combustion se produit principalement le long de la frontière du jet de O_2 avec une fraction de CO_2 maximum dans cette région. Il convient de noter que O_2 est entièrement consommé par la réaction de combustion et sa concentration est de 0 à l'extérieur du jet d'oxygène.

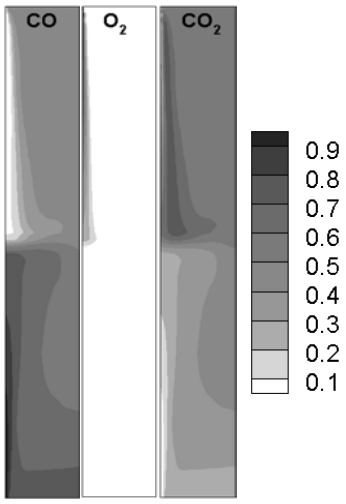

Figure 114: Distributions de la fraction molaire de CO, O2 et CO2 dans le tube de reaction.

Les distributions des fractions molaires de O_2, CO et CO_2 calculées dans deux sections transversales du tube situées à 31,4 et 54,4 cm de la buse d'oxygène sont comparées aux données expérimentales obtenues par Kaizawa et al. [25] sur les Figure 24 et Figure 25. Les données expérimentales sont représentées en ligne continue sur ces figures. Dans la section située dans le jet d'oxygène (31,4 cm de la buse d'oxygène), les distributions suivent la même tendance globale. D'un point de vue quantitatif, les résultats de la simulation diffèrent sensiblement des mesures expérimentales dans le voisinage de l'axe du jet ($r < 2$ cm). A l'intérieur de cette région, notre simulation prédit plus d'oxygène et de carburant et moins de produit que ce qui a été observé expérimentalement. Une raison possible de cet écart entre les fractions molaires calculées et mesurées est le fait que les effets de compressibilité associés au gradient important de la température du gaz n'ont pas été pris en compte dans la version du modèle utilisé pour cette simulation. En s'éloignant de la région axiale du jet, nous avons un meilleur accord avec les mesures. Dans la section transversale située à mi-chemin entre les entrées de O_2 et de CO (54,4 cm de la buse d'oxygène), les concentrations calculées sont en bon accord avec les données expérimentales (précision inférieure à 0,1). Notons que le croisement des profils de CO et de CO_2 observé dans l'expérience près de la paroi latérale n'est pas prédit par le modèle.

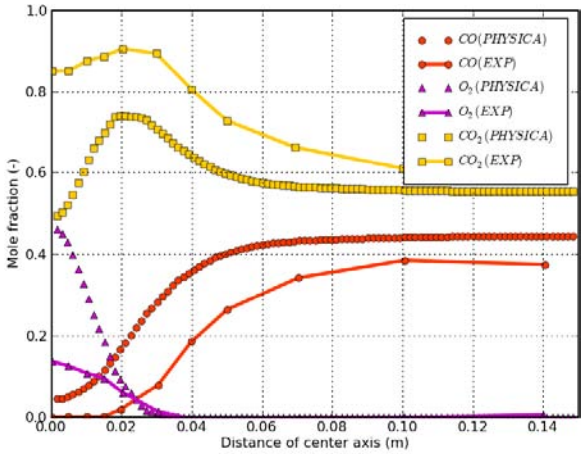

Figure 115: Profils radiaux des fractions molaires calculées et mésurées du CO, CO_2 et O_2 à 31.4 cm de la lance.

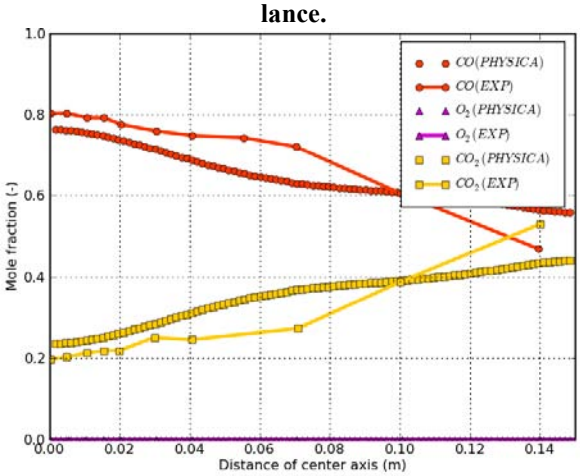

Figure 116: Profils radiaux des fractions molaires calculées et mésurées du CO, CO_2 et O_2 à 54.4 cm de la lance.

IV.2 Simulation du convertisseur pilote d'ArcelorMittal

Dans cette section, le modèle est utilisé pour simuler le comportement de la phase gazeuse dans le convertisseur pilote d'ArcelorMittal. Puisque le modèle des transferts couplés dans la phase gazeuse et celui de l'impact d'un jet sur une surface déformable n'ont pas été couplés à l'heure actuelle, la simulation présentée ici a été effectuée en imposant la forme de la surface libre du bain, à partir du résultat d'un calcul préliminaire réalisé à l'aide du modèle de déformation de surface. Dans la simulation des transferts couplés dans la phase gazeuse, la surface libre du bain déformée reste fixe et est divisée en deux régions. La première région correspond à la cavité ($r \leq 0{,}2$ m) et est le lieu où O_2 peut pénétrer dans le bain, tandis que la deuxième région (de $r = 0{,}2$ m à $r = 0{,}7$ m) est la zone où CO peut entrer dans la phase gazeuse. Cette division est à l'heure actuelle arbitraire. La transition réelle entre un puits d'oxygène et une source de CO à l'interface

ne peut être prédite qu'avec un modèle entièrement couplé entre les deux phases (gazeuse et liquide).

La lance, située à 1 m au-dessus de la surface liquide, pourvoit, à 386 m/s, un jet de O_2 à une température de 218 K. Le débit massique de O_2 entrant dans le bain est égal à 0,157 kg/s et celui du CO sortant du bain est fixé à 0,275 kg/s. La température du CO entrant est prise égale à celle du bain d'acier liquide (i.e. 1573 K). Comme déjà mentionné, le maillage de 5457 cellules, utilisé pour cette simulation, a été déformé pour s'adapter à la forme de la cavité moyennée dans le temps déterminée à partir d'un calcul préliminaire en utilisant le modèle de déformation de surface.

Les distributions de la vitesse et de la température calculées dans la phase gazeuse sont représentées sur la Figure 26. Nous pouvons voir que la vitesse du jet d'oxygène décroit rapidement en s'éloignant de la sortie de lance. Le jet impacte le bain, puis balaie la surface libre du bain et la paroi du convertisseur. L'écoulement comprend une boucle de recirculation unique, avec un fort entraînement dans le jet gazeux du gaz ambiant. Les températures prédites sont dans une marge réaliste et varient entre 1600 K et 2900 K en dehors du cœur potentiel du jet. Les valeurs les plus élevées de température sont situés près de la surface du bain et le long de la frontière du jet d'oxygène, qui correspondent à des régions où la réaction de postcombustion a principalement lieu.

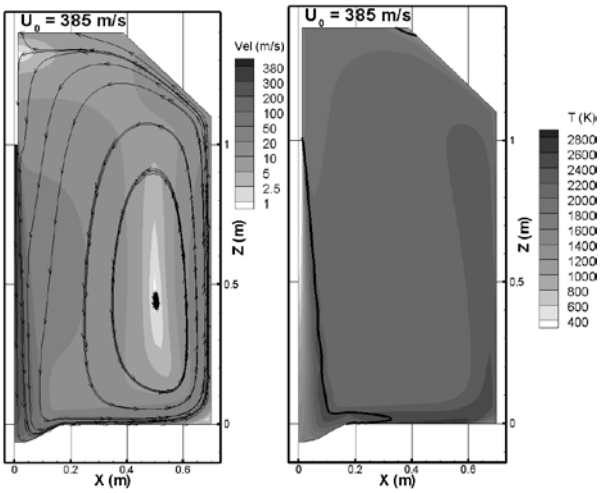

Figure 117: Distribution des lignes de courant, de la vitesse et de la température dans la phase gazeuse du convertisseur pilote (cavité prescrite à la surface du bain).

La Figure 27 représente les distributions de la fraction massique de chaque espèce. On observe que O_2 est entièrement consommé et que la fraction massique de CO est (sauf dans une petite région riche dans le coin en bas à droite) inférieure à 0,2 dans la majeure partie de la phase gazeuse, ce qui signifie que la quasi-totalité de celui-ci est brûlée par l'oxygène, d'où une fraction massique de CO_2 élevée. Le front de flamme, défini comme la courbe où la fraction de mélange est égale à sa valeur stœchiométrique, et qui représente la région principale où la réaction de postcombustion se produit, suit à peu près la frontière du jet d'oxygène et une partie de la surface du bain. Ce résultat est cohérent avec le modèle proposé par Hirai et al. [28]. Le taux de postcombustion à la sortie du convertisseur est égal à 85%.

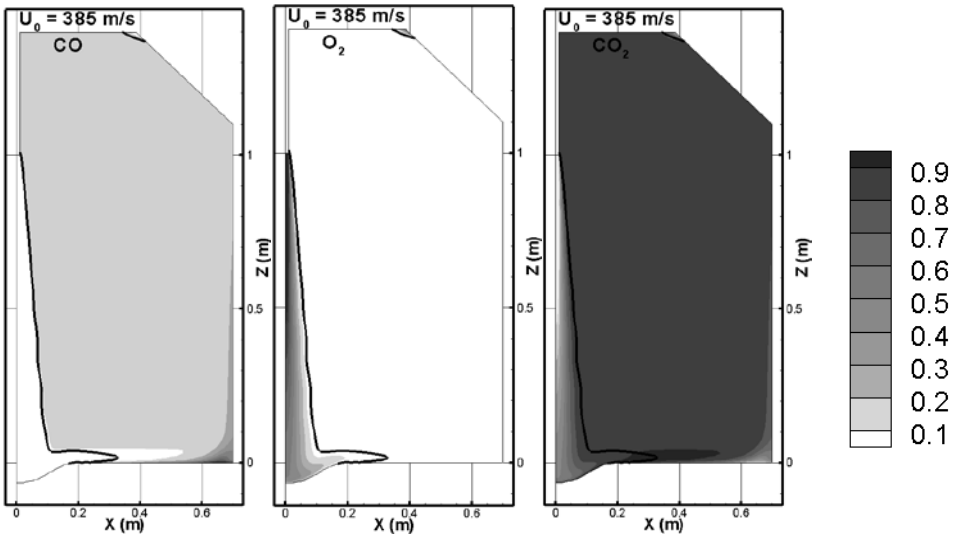

Figure 118: Distributions de la fraction massique du CO, CO_2 et O_2 dans la phase gazeuse du convertisseur pilote (cavité prescrite à la surface du bain). La ligne noire représente le front de flamme.

Conclusions

Deux modèles distincts ont été développés pour étudier différents phénomènes dans un convertisseur d'aciérie.

Le premier modèle décrit la déformation de la surface libre du bain de métal sous l'impact du jet de gaz. Il prend en compte les effets de compressibilité dans le cas de jets à forte vitesse. Néanmoins, dans la version actuelle du modèle, le gaz est considéré incompressible près de la surface libre (ce qui est une approximation raisonnable pour les applications envisagées dans cette étude). L'advection de la surface libre par la méthode VOF a été traitée en utilisant un nouveau schéma, appelé Counter Diffusion Method, ce qui permet d'avoir des temps de simulation beaucoup plus petits. Ce modèle de jet impactant a été confronté à des données expérimentales de la littérature, obtenues dans des maquettes froides pour des systèmes à deux et trois phases. La profondeur de pénétration du jet est bien reproduite par le modèle alors que concernant la largeur de la cavité la confrontation du modèle avec l'expérience est moins bonne. Ceci peut s'expliquer par la surestimation de l'élargissement du jet résultant de l'utilisation du modèle de turbulence k-ε standard. Dans ces simulations, les effets de différents paramètres ont été analysés. Lorsque l'on compare deux schémas VOF différents (donor-acceptor et counter diffusion method), il a été constaté que les dimensions de la cavité restent du même ordre de grandeur. À la sortie de lance, la spécification de profils non-uniformes des paramètres du jet conduit à une cavité plus profonde que lorsque nous utilisons des profils uniformes. Le modèle k-ε filtré produit une cavité légèrement plus profonde que le modèle k-ε standard. Enfin, le modèle de déformation de la surface du bain a été utilisé pour calculer la cavité créée par un jet d'oxygène à forte vitesse dans un convertisseur pilote dans lequel les effets de compressibilité sont importants.

Le second modèle rend compte des écoulements, des transport de masse et de chaleur et de la réaction de postcombustion dans la phase gazeuse du convertisseur. Il utilise l'algorithme SCRS pour décrire le transport des espèces chimiques, et prend en compte l'absorption de l'oxygène par le bain et les transferts thermiques radiatifs. Des simulations ont été présentées pour des expériences réalisées à l'échelle du laboratoire et à l'échelle pilote. Le modèle donne des résultats cohérents, en montrant de bonnes tendances. Il a été observé que pour les conditions particulières considérées ici la réaction de postcombustion, qui se produit principalement le long de la frontière du jet et à proximité de la surface du bain, est très efficace et que des valeurs très

élevées du taux de postcombustion à la sortie du convertisseur peuvent être atteintes pour dans un convertisseur de taille pilote.

Les deux modèles développés dans cette étude sont indépendants à l'heure actuelle. Dans la section précédente, nous avons présenté une méthode de couplage faible qui a pu permettre une simulation de la phase gazeuse en utilisant les résultats du modèle d'impact du jet. Dans un travail futur, il serait souhaitable de coupler les deux modèles, ce qui permettra une meilleure compréhension des interactions entre les réactions de décarburation et de postcombustion ainsi que les mécanismes de pénétration de l'oxygène dans le bain de métal.

Références

1. R.B. Banks and D.V. Chandrasekhara: J. Fluid Mech., 1963, vol. 15, pp. 13-35.
2. A. Nordquist, N. Kumbhat, L. Jonsson and P. Jonsson: Steel Res. Int., 2006, vol. 77, pp. 82-90.
3. O. Olivares, A. Elias, R. Sanchez, M. Diaz-Cruz and R. Morales: Steel Res., 2002, vol. 73, pp. 44-51.
4. A.V. Nguyen and G.M. Evans: Applied Mathematical Modelling, 2006, vol. 30, pp. 1472-1484.
5. H. Odenthal, J. Kempken, J. Schluter and W. Emling: Iron Steel Technol., 2007, vol. 4, pp. 71-89.
6. M. Ersson, L. Hoglund, A. Tilliander, L. Jonsson and P. Jonsson: ISIJ Int., 2008, vol. 48, pp. 147-153.
7. L. Zhang and F. Oeters: Steel Res., 1991, vol. 62, pp. 95-106.
8. L. Zhang and F. Oeters: Steel Res., 1991, vol. 62, pp. 107-116.
9. H. Gou, G. Irons and W. Lu: Metall. Trans. B, 1993, vol. 24, pp. 179-188.
10. J. Huber, J. Lehmann and R. Cadet: Rev. Metall. (Paris), 2008, vol. 105, pp. 121-126.
11. N. Croft, K. Pericleous, and M. Cross: Numerical Methods in Laminar and Turbulent Flow, vol. 9, Part 2, edited by C. Taylor et al., Pineridge Press, Swansea, U.K., 1995, pp. 1269-1280.
12. B.E. Launder and D.B. Spalding: Lectures in Mathematical Models of Turbulence, Academic Press, London, England, 1972.
13. K.S. Abdol-Hamid, S.P. Pao, S.J. Massey and A. Elmiligui: Trans. ASME, 2004, vol. 126, pp. 844-850.
14. M. Alam, J. Naser and G. Brooks: Metall. Trans. B, 2010, vol. 41B, pp. 636-645.
15. B. Lebon, Unstructured finite volume algorithms for compressible multiphase flow, PhD thesis, University of Greenwich, London, 2011.
16. I. Sumi, Y. Kishimoto, Y. Kikuchi and H. Igarashi: ISIJ Int., 2006, vol. 46, pp. 1312-1317.
17. S.T. Johansen, J. Wu and W. Shyy: Int. J. Heat Fluid Flow, 2004, vol. 25, pp. 10-21.
18. C.W. Hirt and B.D. Nichols: J. Comput. Phys., 1981, vol. 39, pp. 201-225.
19. K. Pericleous, G. Djambazov, B. Lebon, T.N. Croft, J.F. Domgin and P. Gardin: Rev. Metall. (Paris), 2008, vol. 105, pp. 207-217.
20. D. Wheeler, Computational modelling of surface tension phenomena in metals processing, PhD thesis, University of Greenwich, London, 2000.
21. B.E. Launder, W.C. Reynolds, W. Rodi, J. Mathieu and D. Jeandel: Turbulence models and their applications, Paris 5ème: Eyrolles, 1984.
22. D.B. Spalding: Combustion and mass transfer, Pergamon Press, 1979.
23. L. Hjertager, B. Hjertager and T. Solberg: Comput. Chem. Eng., 2002, vol. 26, pp. 507-515.
24. F. Qian, R. Mutharasan and B. Farouk: Metall. Trans. B, 1996, vol. 27B, pp. 911-920.
25. A. Kaizawa, N. Sasaki, T. Inomoto, Y. Ogawa: Proceeding of the 8th International Conference on CFD in Oil & Gas, Metallurgical and Process Industries, SINTEF/NTNU, Trondheim, Norway, 2011, Paper CFD11-88.
26. B.E. Launder: Int. J. Heat Fluid Flow, 1989, vol. 10, pp. 282-300.
27. S.C. Koria and K.W. Lange: Steel Res., 1987, vol. 58, pp. 421-426.

28. M. Hirai, R. Tsujino, T. Mukai, T. Harada and M. Omori: Trans. Iron Steel Inst. Jpn, 1987, vol. 27, pp. 805-813.

UNIVERSITÉ DE LORRAINE

AUTORISATION DE SOUTENANCE
DU DOCTORAT DE L'UNIVERSITE DE LORRAINE

o0o

VU LES RAPPORTS ETABLIS PAR :
Monsieur Eric CLIMENT, Professeur, Institut de Mécanique des Fluides de Toulouse,
Monsieur Mark JOLLY, Senior lecturer, University of Birmingham (UK)

L'Administrateur Provisoire de l'Université de Lorraine, autorise :

Monsieur Yannick Nikienta DOH

à soutenir devant un jury de l'UNIVERSITE DE LORRAINE, une thèse intitulée :

"Modélisation multiphysique du convertisseur d'aciérie"

en vue de l'obtention du titre de :

DOCTEUR DE l'UNIVERSITE DE LORRAINE

Intitulé du doctorat : **"Sciences des Matériaux"**

Fait à Vandoeuvre, le 11 janvier 2012
Pour l'Administrateur Provisoire par délégation,
Le Chargé de Mission,
François LAURENT

UNIVERSITÉ DE LORRAINE
34 COURS LEOPOLD - CS 25233
54052 NANCY CEDEX
TEL : 03 54 50 54 00
CONTACT@UNIV-LORRAINE.FR
WWW.UNIV-LORRAINE.FR

Multiphysics modelling of the steelmaking converter

Abstract

The present thesis treats different phenomena taking place in a steelmaking converter through the development of two separate models. The first model describes the cavity produced at the free surface of the metal bath by the high speed impinging oxygen jet. The model is based on a zonal approach, where gas compressibility effects are taken into account only in the high velocity jet region while elsewhere the gas is treated as incompressible. The Volume Of Fluid (VOF) method is employed to follow the deformation of the bath free surface. Calculations are presented for two- and three-phase systems and compared against experimental data obtained in various cold model experiments. The influence on the size and shape of the cavity of various parameters and models (including the jet inlet boundary conditions, the VOF advection scheme and the turbulence model) is studied. Next, the model is used to simulate the interaction of a supersonic oxygen jet with the surface of a liquid steel bath in a pilot-scale converter. The second model concentrates on fluid flow, heat transfer and the post-combustion reaction in the gas phase above the metal bath. The model uses the Simple Chemical Reaction Scheme approach to describe the transport of the chemical species and takes into account the consumption of oxygen by the bath and thermal radiative transfer. The model predictions are in reasonable agreement with measurements collected in a laboratory experiment and in a pilot-scale furnace.

Key Words: Basic Oxygen furnace (BOF), mathematical modelling, impinging gas jet, compressible flow regime, free surface, post-combustion reaction.

Modélisation multiphysique du convertisseur d'aciérie

Résumé

Le présent manuscrit de thèse traite de différents phénomènes dans un convertisseur d'acier à travers le développement de deux modèles distincts. Le premier modèle décrit la cavité produite à la surface libre du bain de métal par l'impact du jet d'oxygène supersonique. Le modèle est basé sur un découpage du domaine de calcul en deux régions. Les effets de compressibilité du gaz sont pris en compte uniquement dans la région du jet où la vitesse est élevée, alors que partout ailleurs, le gaz est considéré comme incompressible. La méthode Volume Of Fluid (VOF) est utilisée pour suivre la déformation de la surface libre du bain. Des calculs sont présentés pour des systèmes bi- et triphasés et comparés à des données expérimentales obtenues dans des maquettes froides. L'influence sur la taille et la forme de la cavité de différents paramètres et modèles parmi lesquels les conditions d'injection du jet, le schéma d'advection de la méthode VOF et le modèle de turbulence) est étudiée. Ensuite, le modèle est utilisé pour simuler l'interaction entre un jet supersonique d'oxygène et la surface libre d'un bain d'acier liquide dans un convertisseur de taille pilote. Le second modèle se focalise sur l'écoulement du gaz, le transfert de chaleur et la réaction de postcombustion dans la phase gazeuse au-dessus du bain de métal. Le modèle utilise l'algorithme Simple Chemical Reaction Scheme pour décrire le transport des espèces chimiques, et prend en compte l'absorption d'oxygène par le bain et les transferts thermiques radiatifs. Les prédictions du modèle sont en accord raisonnable avec les mesures recueillies dans une expérience de laboratoire et dans un four à l'échelle pilote.

Mots clés: convertisseur d'aciérie, modélisation mathématique, jet gazeux impactant, régime d'écoulement compressible, surface libre, réaction de postcombustion.